



Universidade do Porto

Faculdade de Engenharia

FEUP

FACULDADE DE ENGENHARIA DA UNIVERSIDADE DO PORTO

MASTER THESIS

**DEVELOPMENT OF A LOW FIDELITY PROCESS
MODEL FOR ADDITIVE MANUFACTURING.**

Computational Mechanics master

Author: MANUEL JIMÉNEZ ABARCA

Supervisors: OLE SIGMUND, ANDERS CLAUSEN, CESAR DE SÁ

Copenhagen, September of 2020

Acknowledgment.

This Master Thesis was carried out at the Institute of Science and Innovation in Mechanical and Industrial Engineering (INEGI¹) in Porto and at Technical University of Denmark (DTU) in Lyngby between January and September 2020 as a part of the Computational Mechanics program from the Faculty of Engineering at University of Porto (FEUP).

I would like to thank my supervisor at DTU Dr. Ole Sigmund for guiding the decisions made and his support during the complete work here presented. I would also like to thank the members from the Oqton company Anders Clausen and Erik Andreassen for providing the data related to the experimental print and their advice about the printing outcomes. Also, a kindly thanks to my supervisor at FEUP Dr. José Cesar de Sá for tracking my progress and giving me the opportunity to start researching at INEGI in the additive manufacturing field. A friendly thanks to my colleague at INEGI Roya Darabi for the positive co-working experience. Finally, a warm thanks to my parents Manuel Jimenez and Maria Angeles Abarca for supporting me from the beginning of my studies.

Sincerely,

Manuel Jimenez Abarca

¹ through funding of Project ADDing (POCI-01-0145-FEDER-030490), co-financed by Fundo Europeu de Desenvolvimento Regional (FEDER) through Programa Operacional Competitividade e Internacionalização (COMPETE 2020) and Fundação para a Ciência e a Tecnologia (FCT), Portugal.

Abstract.

Additive manufacturing of metal components is a complex process that involves an exhaustive experimental work to achieve the demands of the customers. The computer simulation is a powerful tool to support the experimental work and reduce the lead time and cost required. However, the simulation process has its own challenges.

The finite element-based software Abaqus is selected to run two different methods of printing simulation: thermo-mechanical and Inherent strains-based. The presented models are classified according to the level of fidelity of the solution. Two studies are carried out: comparison of the thermo-mechanical models in a scaled part and validation of the simulation methods in an industrial-size part. Data from experimental prints is used to validate the results of the simulations. The trade-off between accuracy and computational cost is examined. In addition, the capabilities of the software to implement the complete manufacturing process are evaluated.

A deep knowledge of the manufacturing process and the finite element software is required to successfully simulate the final state of a printed component. The Inherent strains-based method is a better choice in terms of efficiency and accuracy than the thermo-mechanical method to model parts typically printed in the additive manufacturing industry. The software allows to simulate the whole metal printing process but presents some limitations in the implementation.

Keywords: Additive manufacturing, selective laser melting, finite elements method, Inherent strains, residual stresses, Abaqus.

Index

1.	Introduction.....	12
1.1.	Motivation.....	12
1.2.	Additive Manufacturing.....	12
2.	Finite Elements Analysis.....	16
2.1.	Thermo-mechanical simulation.....	16
2.1.1.	Progressive element activation.....	17
2.1.2.	Moving heat source.....	18
2.1.3.	Thermal losses.....	21
2.2.	Inherent strains-based simulation.....	21
2.2.1.	Progressive element activation.....	22
2.2.2.	Pattern-mesh intersection.....	23
3.	Basis formulation and governing equations.....	26
3.1.	A non-linear finite element approach.....	26
3.2.	Thermal model.....	26
3.2.1.	Thermal equilibrium.....	27
3.2.2.	Boundary conditions.....	27
3.3.	Continuums mechanics.....	28
3.3.1.	Elasticity.....	28
3.3.2.	Boundary conditions.....	29
3.3.3.	Plasticity.....	29
3.3.4.	Inherent strains.....	31
4.	Material modelling.....	32
4.1.	Material selection.....	32
4.2.	Latent heat effect.....	34
4.3.	Plasticity model.....	35
5.	Geometry selection.....	37
6.	Scaled model.....	39
6.1.	Part-fixing.....	39
6.2.	Tool path and scanning strategy.....	40
6.3.	Level of fidelity.....	41
6.4.	Boundary conditions.....	42
6.5.	Interactions.....	43
6.6.	Printing parameters.....	44
6.7.	Cooling.....	45
6.8.	Mesh.....	45
6.9.	Time-stepping.....	46
6.10.	Results.....	47
6.10.1.	Thermal results.....	47
6.10.1.1.	High Fidelity model.....	47

6.10.1.2.	Medium Fidelity model.....	50
6.10.2.	Mechanical results.....	51
6.10.2.1.	High Fidelity model.....	51
6.10.2.2.	Medium Fidelity model.....	53
6.10.3.	Models comparison.....	54
6.10.4.	Computational cost.....	56
7.	Real model.....	57
7.1.	Part-fixing.....	57
7.2.	Inherent strains application.....	59
7.3.	Boundary conditions.....	61
7.4.	Interactions.....	61
7.5.	Printing parameters.....	62
7.6.	Mesh.....	63
7.7.	Time-stepping.....	64
7.8.	Results.....	65
7.8.1.	After printing.....	65
7.8.2.	Supports removal.....	68
7.8.3.	Heat treatment.....	70
7.9.	Experimental data.....	74
7.9.1.	Available data.....	74
7.9.2.	Measurement methodology.....	74
7.9.3.	Results.....	76
7.10.	Results comparison.....	77
7.10.1.	Non-heat treated part.....	77
7.10.1.1.	Low Fidelity model.....	78
7.10.1.2.	Medium Fidelity model.....	80
7.10.2.	Heat treated part.....	82
7.11.	Computational cost.....	83
8.	Conclusions.....	84
9.	Assessment of the work done.....	86
9.1.	Objectives achieved.....	86
9.2.	Limitations and Future work.....	86
A.	Appendix.....	89
A.1.	Collaborating organizations.....	89
A.2.	Convergence studies.....	89
A.2.1.	Mesh convergence.....	89
A.2.2.	Time increment convergence.....	95
A.3.	Experimental measurements.....	107

List of Figures

1	<i>SLM manufacturing process</i>	14
2	<i>Removable Partial Denture (RPD) stent fabricated using SLM technology.</i>	14
3	<i>Cranial prosthesis made by an AM metal process.</i>	14
4	<i>Point, infinite line and box toolpaths.</i>	18
5	<i>Infinite line toolpath-mesh intersection.</i>	18
6	<i>Point toolpath-mesh intersection.</i>	20
7	<i>Box toolpath-mesh intersection</i>	20
8	<i>Goldak volume-based energy distribution.</i>	20
9	<i>Simulation steps required in the IS method.</i>	23
10	<i>Example of Island pattern strategy for IS method.</i>	24
11	<i>Scan pattern – element intersection [11].</i>	24
12	<i>Visualization of the first component of the inherent strains in a simple cube.</i> . .	25
13	<i>Stresses and strains in the HAZ during SLM process.</i>	30
14	<i>Ti6AlV4 thermal properties evolution.</i>	33
15	<i>Ti6AlV4 mechanical properties evolution.</i>	33
16	<i>Ti6AlV4 thermal expansion coefficient.</i>	34
17	<i>Latent heat effect in a metal material.</i>	35
18	<i>Hardening model with annealing temperature effect.</i>	36
19	<i>Front and top views (left) and isometric view (right) of the Real part.</i>	37
20	<i>Front and top views (left) and isometric view (right) of the Scaled part.</i>	38
21	<i>Build plate top and front view.</i>	39
22	<i>Scanning strategy of the Scaled model.</i>	41
23	<i>Contact surface between build plate and part.</i>	43
24	<i>8 nodes linear brick element.</i>	46
25	<i>Mesh distribution for the part (left) and the build plate (right).</i>	46
26	<i>Isosurface of the melting pool gradient for the High-fidelity model.</i>	48
27	<i>Cross section and depth views of the molten pool for the High-fidelity model.</i> . .	49
28	<i>Thermal history of the node 971 for the High-fidelity model.</i>	49
29	<i>Thermal history of the node 4759 for the MF scaled model.</i>	50
30	<i>Node evaluated (red point) for the MF scaled thermal history.</i>	51
31	<i>Distortions in X-direction U1 (left), Y-direction U2 (centre) and Z-direction U3 (right) for the HF model. Units in mm.</i>	52
32	<i>Temperature field comparison between left side (top) and right side (bottom) of the HF model. Toolpath depicted in red on the right.</i>	52
33	<i>Von Mises stress σ_{VM} (MPa) for the HF model.</i>	53
34	<i>Displacement magnitude U in mm for the MF model.</i>	54
35	<i>Von Mises stress σ_{VM} distribution (left) and stress singularity (right) for the MF model.</i>	54
36	<i>Locations evaluated for the models' comparison of U_x (blue) and U_y (red).</i>	55
37	<i>Cross-sections at $z = 4$ mm of the MF model (red) and HF model (blue) after print. Measurements in mm.</i>	56
38	<i>Support's geometry (left) and distribution along the part (right). Dimensions in mm.</i>	58
39	<i>Build plate top and front view. Dimension in mm.</i>	59
40	<i>ε_{11}^* state before the addition of a new element layer (left) and after the addition of a new element layer (right).</i>	60
41	<i>Part contact surface (left) and build plate contact surface (right).</i>	61

42	<i>Scanning strategy of the Real model</i>	63
43	<i>Mesh distribution for the supports and part (left) and the build plate (right).</i>	64
44	<i>Distortions in X-direction U1 (left), Y-direction U2 (centre) and Z-direction U3 (right) for the LF model. Units in mm.</i>	66
45	<i>Distortions in X-direction U1 (left), Y-direction U2 (centre) and Z-direction U3 (right) for the MF real model. Units in mm.</i>	66
46	<i>Detail of the distortions in Z-direction U3 for the MF model.</i>	67
47	<i>Cross-sections at z=20 mm of the LF model (red) and MF model (blue) after print. Measurements in mm.</i>	67
48	<i>Stress distribution in MPa in the outer face (left) and a detail in the support's area (right) for the LF model.</i>	68
49	<i>Stress distribution in MPa in the outer face (left) and a detail in the support's area (right) for the MF real model.</i>	68
50	<i>Section of the supports cut from the LF model.</i>	69
51	<i>Locations constrained in X-direction (top), Y-direction (bottom left) and Z-direction (bottom right) for the cutting procedure.</i>	69
52	<i>Stress distribution before cut (left) and after cut (right).</i>	70
53	<i>Comparison of cross-sections of the part before cutting (dark blue) and after cutting (light blue).</i>	70
54	<i>Annealing heat cycle</i>	72
55	<i>Stress-temperature annealing cycle on LF model. Stress (blue), temperature (red).</i>	72
56	<i>Point evaluated during the Annealing treatment (highlighted in red).</i>	73
57	<i>Stress – creep strain relationship during the annealing treatment. Stress (blue), strain (orange).</i>	73
58	<i>Bottom cross-sections of the LF model with annealing treatment (red) and without annealing treatment (blue).</i>	74
59	<i>Inspection machine developed by Oqton® to scan the experimental parts.</i>	75
60	<i>Scanned part before removal of the clamp (left) and after removal of the clamp (right).</i>	75
61	<i>Measurements in the experimental parts.</i>	76
62	<i>Contour shape comparison between the original part (blue) and experimental Part1 (red) for the Non-HT case.</i>	77
63	<i>Error in the application of the Inherent strains on the last element layer</i>	78
64	<i>Deformed shape of the Part1 (red) and the LF part (blue) for the non-heated treatment case.</i>	79
65	<i>Cross-section's contour at z=12 mm of the experimental part (red) and LF model (blue). Measurements in mm</i>	79
66	<i>Residual stress presented in MF model after printing. Von Mises stress in MPa.</i>	80
67	<i>Closing effect. Deformed shape after printing (blue) and after stresses release (red) for the MF model.</i>	81
68	<i>Support's top surface deformation after printing for the MF model. Displacements in mm.</i>	81

List of Tables.

1	<i>Material basic properties.</i>	33
2	<i>Laser scanning parameters of the Scaled model.</i>	40
3	<i>Laser energy distribution parameters.</i>	44
4	<i>Laser scanning parameters of the Real model.</i>	63
5	<i>Creep law parameters.</i>	72
6	<i>Measurements of the experimental parts after cut for the HT and Non-HT parts .</i>	76
7	<i>Experimental - simulated model comparison for the Non-HT case.</i>	77
8	<i>Experimental - LF model comparison for the HT case.</i>	82

Notation.

Symbol	Unit	Description
q	mW/mm^2	Heat flux density
x, y, z	mm	Cartesian coordinates
Q	mW	Input energy
η	-	Absorption coefficient
P	mW	Laser power
r	mm	Laser spot radius
e	-	Laser spot eccentricity
d	mm	Laser spot depth
φ	-	Patch local angle
θ	-	Interlayer rotation angle
U	-	Solution vector
R	-	Residual vector
Δt	s	Time step
C_p	$mJ/(t \cdot K)$	Specific heat capacity
θ	K	Temperature
t	s	Time
\vec{r}	mm	Relative spatial coordinate
k	$mW/(mm \cdot K)$	Thermal conductivity
q_k	mW/mm	Heat flux conduction
h	$mW/(mm^2 \cdot K)$	Film coefficient
σ	$mW/(mm^2 \cdot K^4)$	Stefan-Boltzmann constant
ϵ	-	Emissivity
$\vec{\sigma}$	MPa	Tension vector
$\vec{\epsilon}$	-	Deformation vector
E	MPa	Young modulus
ν	-	Poisson's coefficient
σ_y	MPa	Yielding stress
u	mm	Displacement
α	$1/K$	Expansion coefficient
$\dot{\epsilon}$	-	Strain rate
σ_{VM}	MPa	Von Mises stress
ϵ^*	-	Inherent strain

Acronyms.

Abbreviation	Meaning
AM	Additive Manufacturing
CAD	Computer Aided Design
DED	Direct Energy Deposition
PBF	Powder Bed Fusion
EBM	Electron Beam Melting
SLM	Selective Laser Melting
CNC	Computer Numerical Control
FEM	Finite Element Method
CAE	Computer Aided Engineering
HAZ	Heat Affected Zone
TGE	Temperature Gradient Effect
STL	STereoLithography
BC	Boundary Conditions
NIST	National Institute of Standards and Technology
HF	High Fidelity
MF	Medium Fidelity
LF	Low Fidelity
HT	Heat Treated

1. Introduction.

1.1. Motivation.

The simulation of additive manufacturing (AM) processes has traditionally demanded a high computational cost translated into powerful computers and large running times. It derives from the refined solution needed to capture the large temperature gradients in very short times presented in the building process. These simulations generate very accurate results and the models are called “High fidelity” models. However, an approximate model can often be sufficient to guide manufacturing choices.

The objective of this work is to create a “Low fidelity” model which approximates the final state of the printed part at a substantially lower computational cost. For that purpose, an inherent strain-based calculation method is used together with other simplifications. The trade-off between accuracy and computational cost is examined and the results compared with higher fidelity and experimental ones.

As a result, the approximate model is validated, and the modelling choices made in this work can be useful to guide future AM modelling under similar conditions.

1.2. Additive Manufacturing.

AM or, commonly referred as 3D printing, describes the modern technology which automatically builds up parts layer by layer using a Computer Aided Design (CAD) file. Parts can be produced in complex forms that are not possible to be produced using traditional manufacturing methods. In addition, it does not rely on expensive tooling having essentially no start-up costs. That also leads to rapid verification and development of prototypes and low-volume production parts. However, this technology presents some limitations. The main one is the inability to produce parts with material properties equivalent to those made via subtractive or formative procedures [1]. Basically, the parts produced are inherently anisotropic and not fully dense. AM also has limitations in repeatability due to variations during cooling.

The different AM technologies can be classified according to the material used: polymer or metal. Metal 3D printing allows to produce high-quality, functional and load bearing parts. They can also be divided by the way the material is placed on the build plate in depositing or powder bed processes [1]. The deposition process is made by the printing nozzle at the same

time as the material is heated. An example is the Direct Energy Deposition (DED) process, typically used to repair or add additional material to existing components. On the other hand, in the powder bed fusion (PBF) processes the material is spread over the building plate and, subsequently, melted by the energy source. Lastly, PBF processes can be differentiated according to the energy heat source in Electron Beam Melting (EBM) and Selective Laser Melting (SLM).

The PBF process has 4 steps depicted in figure 1:

- 1. A thin layer of the powder material is spread along the build plate surface.
- 2. The high-powered laser scans a single cross section of the part and fuse it with the material underneath.
- 3. An elevator lowers the build plate by the thickness of the powder layer.
- 4. A roller pushes a new layer of powder over the built component. The steps 2, 3 and 4 are repeated until the part is completed.

The main limitations of SLM are cost and build size. Thus, only the critical and complex parts of a design should be printed. The simpler sections should be machined by Computer Numerical Control (CNC) and then assembled.

SLM suits better in dental, medical, aerospace and automotive applications where the fundamental benefits of AM are required [1]. SLM has become popular in the dental industry to produce crowns, bridges and stents like the ones shown in figure 2. The possibility of producing a large number of customised parts in a single print has significantly accelerated the manufacturing process. The medical industry has also embraced AM. The high level of freedom in the design enables an exact fit in the patient's anatomy and can include unique surface characteristics (like porosity) to imitate biological textures. Figure 3 shows an example of a customized cranial prosthesis. Related to the aerospace and automotive industries the SLM process plays an important role in parts where weight reduction is a critical design parameter. SLM also ensures the production of complex parts with a high strength and made of high-performance metals.

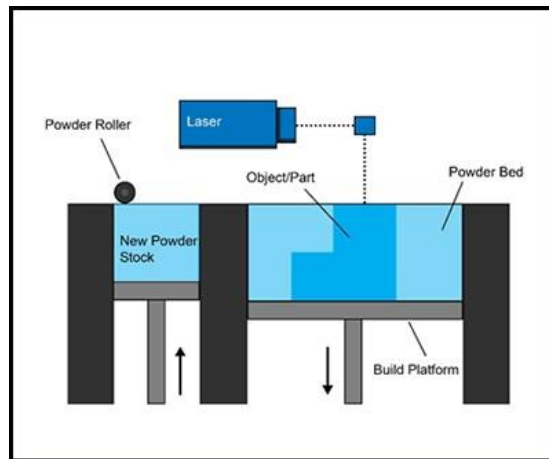


Figure 1: SLM manufacturing process [2].



Figure 2: Removable Partial Denture (RPD) stent manufactured using SLM technology.



Figure 3: Cranial prosthesis made by an AM metal process [3].

The aforementioned benefits of AM and specially of the SLM process have created an excitement atmosphere about this technology. However, the process is not as simple and accurate as promised. The involving change of phase (melting and solidification) of a material region over a much cooler body produces expansion and contraction in the part which leads to permanent warping as well as to high residual stresses [4]. Residual stresses can cause failure during printing or during the in-service life of a part. The distortion imperils the economic feasibility of producing parts using the AM technology as, usually, iterative builds are required to minimize the warping. Each experimental test can take hours to days to complete with the consequent cost. Thus, modelling of the thermo-mechanical behaviour becomes a complement or even an alternative to repetitive experimental tests. The objectives of the AM simulation are to [5]:

- Predict the residual stresses in a part.
- Minimise the gap between the designed and manufactured part through process optimization.
- Evaluate how a manufactured part performs under realistic loading conditions in an assembly with other components.

Modelling an AM process has its own challenges. First, implementing the progressive material addition and then to deal with the non-linearities introduced by the thermal dependence of the material properties as well as the material state change. Related to the mechanical behaviour, a proper plasticity model must be implemented. In addition, due to the transient characteristic of the process, the discretization both in space and time may require expensive computational resources and a deeper understanding of computational methods to achieve accurate results in a feasible time.

2. Finite Elements Analysis.

The Finite Element Method (FEM) has been consolidated over the last decades as the main solution for Computer Aided Engineering (CAE) problems. The novel AM technology is not an exception and numerous FEM commercial software packages have implemented the mechanisms needed to accurately simulate the process. The modelling of the SLM process must overcome the following challenges:

- Progressive Material addition.
- Moving heat source input.
- Thermal losses during building.
- Thermo-mechanical coupling.
- Material properties dependence on temperature.

From the different software available Abaqus/Standard from Dassault Systèmes® is selected due to its special AM plug-in. The plug-in consists of pre-defined tables and modules that allows to model in a detailed and efficient way. Abaqus does not only implement a solution for the aforementioned challenges, but it is developed in a user subroutine structure and keywords interface that provides a high degree of control and customization. Abaqus/Standard uses thermo-mechanical and eigenstrain analyses for the simulation of AM processes.

2.1. Thermo-mechanical simulation.

A thermal-stress analysis allows exact specification in time and space of processing conditions and control over the fidelity of the solution. It is usually more accurate but more computationally expensive than the pure mechanical eigenstrain analysis.

The thermal-stress analysis is decoupled or weakly coupled, assuming that the thermal behaviour affects the mechanical one, but the mechanical response does not affect the thermal history. This is due to the fact that the energy from the heat source is very large compared to the strain energy stored in the workpiece [6]. The process turns into a sequential simulation where the heat transfer problem is solved first and then the mechanical response. Basically, the thermal loads introduced by the printing process results in a temperature field which drives the static structural analysis.

2.1.1. Progressive element activation.

The layer by layer deposition of raw material from a roller and the melting process are modelled using progressive element activation. The elements with the activation feature on can be activated by assigning a volume fraction of material at the beginning of the increment. Both full and partial activation are implemented. The addition of material into a numerical model means the addition of new equations. To account for this, the “Dead-alive” method is used which adds the new equations into the matrices over the history of the model [7].

The elements get activated when they are intersected by a tool path. Abaqus presents the Toolpath-mesh intersection module to compute the geometric intersection between several toolpaths and the finite element mesh of the part to be manufactured. A toolpath is defined by a geometric shape attached to a reference point that moves along a path. The path is defined by connecting a collection of points in space and time. An event series defines the collection of points [8]. The three shapes considered for toolpath-mesh intersection are illustrated at the figure 4.

For example, the infinite line representation is useful to describe the process of layer-by-layer material deposition, such as the activation of the roller in PBF [9]. Figure 5 depicts the intersections of an infinite line toolpath with a finite element, E . The toolpath is defined by an infinite line attached to a reference point that is moving along the path connecting points $(X_1, X_1, X_1, \dots, X_N)$ such that the reference point is at X_i at time t_i . For a given element, the toolpath-mesh intersection module computes the number of intersections, m , and the volume fraction, v_f , for each intersection. The volume fraction is equal to the ratio of the partial volume of the element below the z-plane defined by the motion of the infinite line following the path to the total volume of the element. The module also computes the area A ; the coordinate X^a with respect the element reference coordinate system of the centre of the intersection of the z-plane and the element; as well as the area fractions, α_i^f , below the z-plane for all sides for each intersection [8].


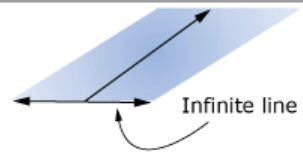
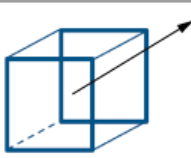
Shape	Point	Infinite Line	Box
Schematic			
Machine tool examples	Point lasers for coarse meshes	Recoater in powder-bed fabrication	Material deposition nozzle in polymer extrusion, wire-feed, laser blob for fine meshes, etc.

Figure 4: Point, infinite line and box tool shapes [8].

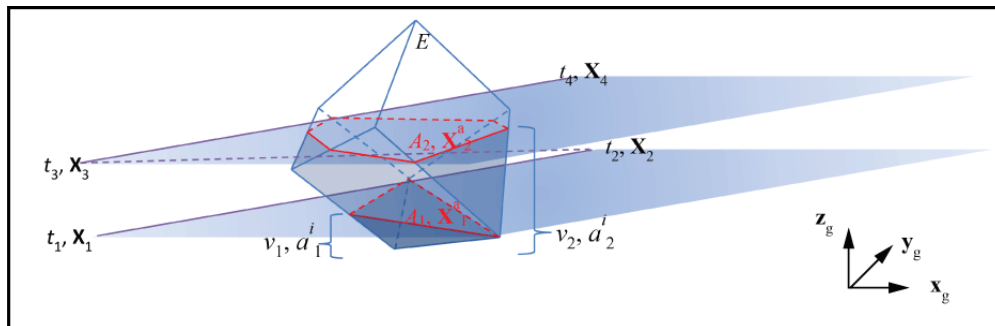


Figure 5: Infinite line toolpath-mesh intersection [8].

2.1.2. Moving heat source.

The recently deposited layer of material gets heated up to the melting point, causing the material to fuse to the solid material underneath. For that purpose, the modelling of the heat source is required. The challenges are to accurately capture the size and shape of the energy distribution and to estimate the amount of heat actually absorbed by the printed part.

The laser energy distribution can be modelled as a concentrated spot or a Goldak volume. When the size of the elements used is significantly larger than the laser spot, the concentrated moving heat flux is a valid approximation. Then, the point formulation shown in figure 6 is used for the toolpath – mesh intersection. For a given element, it computes the number of intersections of the toolpath, the coordinates of the start and end points ξ_s and ξ_e related to the element reference coordinate system and the start and end times t_s and t_e , for each intersection.

On the other hand, if the size of the elements is comparable or smaller to the laser spot, the laser energy must be distributed over a volume. Then, the Box formulation illustrated at the

figure 7 is used for the toolpath – mesh intersection [8]. The box lengths L_1, L_2, L_3 are oriented along the directions of the local coordinate system. For a given element, it computes the number of intersections of the toolpath, the coordinates of the start and end points ξ_s and ξ_e related to the element reference coordinate system and the start and end times t_s and t_e , for each intersection.

The suggested distribution is based on the Goldak energy distribution [5]. The energy distribution q moves along the x-direction:

$$\begin{aligned} q &= q_f \text{ when } x \geq 0 \\ &= q_r \text{ when } x < 0 \end{aligned} \quad (2.1)$$

$$q_{f/r} = \frac{6\sqrt{3} f_{f/r} Q}{a b c \pi \sqrt{\pi}} \cdot e^{\left(-\frac{3x^2}{c_{f/r}^2}\right)} \cdot e^{\left(-\frac{3y^2}{a^2}\right)} \cdot e^{\left(-\frac{3z^2}{b^2}\right)} \quad (2.2)$$

Figure 8 depicts the Goldak spatial coordinates. q_f and q_r are the front and rear sides of the energy distribution, respectively. f_f and f_r are dimensionless factors related to the lengths of the ellipsoid:

$$f_f = \frac{2}{1+a_r/a_f} \quad (2.3)$$

$$f_r = \frac{2}{1+a_f/a_r} \quad (2.4)$$

The ellipsoid coordinates a, b and c can be approximated by the laser parameters like radius r , eccentricity e or depth d :

$$c = e \cdot r, \quad a = \frac{r}{e}, \quad b = d \quad (2.5)$$

The effective input energy Q represents the product of the laser power P and the material absorption coefficient η .

The scanning path of the moving heat source is defined in an event series in a time, spatial coordinates and power magnitude format.

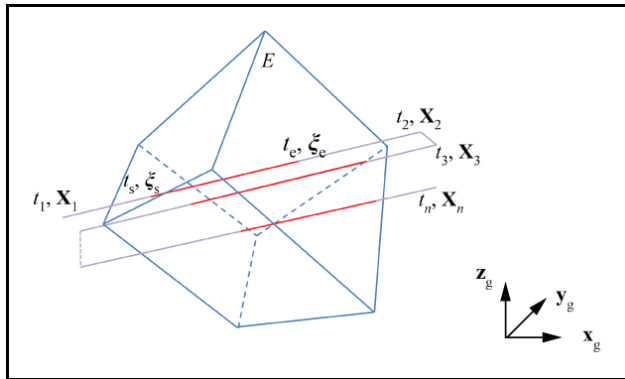


Figure 6: Point-tool path intersection [8].

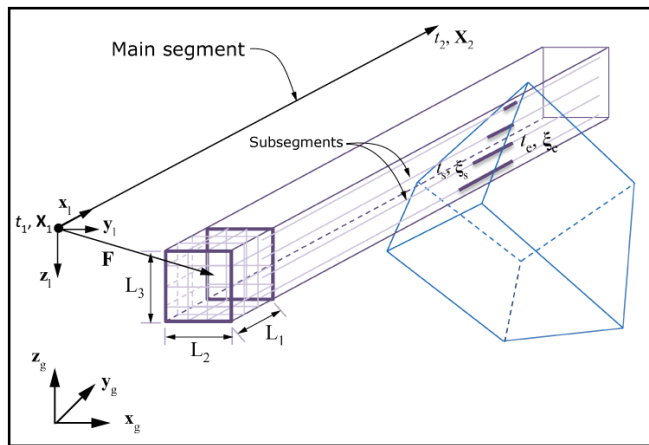


Figure 7: Box-toolpath mesh intersection [8].

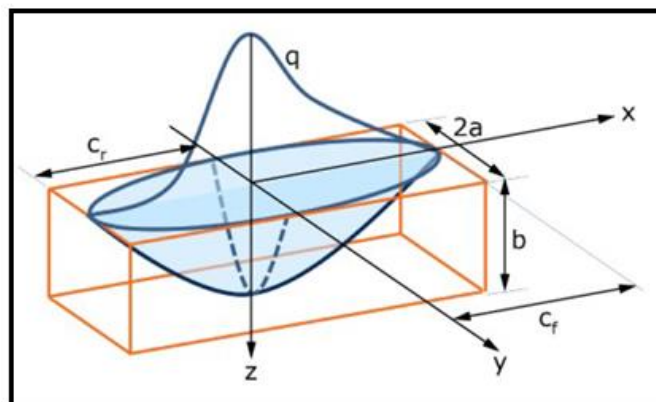


Figure 8: Goldak volume-based energy distribution [5].

2.1.3. Thermal losses.

The thermal losses balance the heat input. Thus, it is important to accurately model the thermal conduction, the free convection and the thermal radiation to ensure that the temperature gradients are properly calculated.

With the deposition of new material, previously exposed material surfaces are covered, and new free surfaces are created with time. Surface convection and radiation can be defined on evolving free surfaces. Abaqus/Standard continuously tracks the evolving free surfaces that reflect the current shape of a printing part and applies convection and radiation loadings only to those surfaces [9]. A sink or room temperature must be introduced in both convection and radiation mechanisms. The film coefficient and the material surface emissivity are commonly extracted from experimental analysis.

2.2. Inherent strains-based simulation.

The Inherent Strains (IS) method is a purely mechanical method which was introduced to reduce the high computational time that the thermo-mechanical approach required to simulate the AM process in industrial parts.

The Inherent strains also referred as Eigenstrains or stress-free strains are an engineering concept used to account for all sources of inelastic deformation that lead to residual stresses and distortions in manufactured components.

The eigenstrains are calculated at the end of the printing process when the residual stresses get relaxed and the component deforms to its ultimate state. Thus, this method assumes that the inherent strains are the cause of the residual stresses. There are different ways to obtain the inherent strains: experimentally, numerically or even empirically for simple cases.

The concept of Inherent strains is based on the fact that every printed layer experiments the same strain state. This comes from the assumption that the laser seam in an AM process is very small in relation to the size of the build part, so that each laser seam has a similar thermal history. This approach presents some error in locations close to the edges of the part where the temperature is affected by the boundary conditions [10].

The IS model is also implemented in the FEM software Abaqus. It offers a high level of customization: different scanning and element activation strategies, pattern rotation and build parameters that allow to simulate the real laser scanning used in industrial components.

2.2.1. Progressive element activation.

The inherent strains are applied layer by layer and, thus, the elements get activated following the same strategy. Figure 9 shows the activation process during the building time [17]. It can be summarized in three steps:

- Time increment 0 : At the beginning all the elements of the model are deactivated.
- Time increment i : Two actions are carried out for each layer of the model: activation of a new layer and application of the inherent strains ε^* on the layer. Both actions can be done at the same time increment and the sequence is repeated until all the layers N get activated.
- Time increment $N+1$: In this step the part is cut off from the build plate. It is simulated by removing a layer of elements from the supports. Consequently, the residual stresses are released allowing to the part to achieve its ultimate shape. In order to avoid an impulse in the static solution additional constraints must be defined in the model.

The number of time increments involved in the simulation is given by the number of layers defined plus the increment for the cutting:

$$n_{inc} = N + 1 \quad (2.10)$$

The elements get activated by assigning a volume fraction of material at the beginning of the increment.

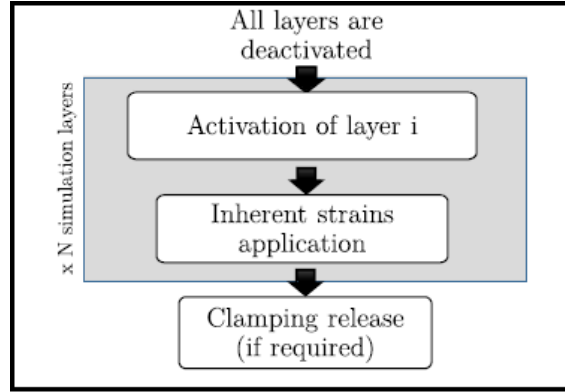


Figure 9: Simulation steps required in the IS method [17].

2.2.2. Pattern-mesh intersection.

A scanning strategy is defined to assign a distribution of the inherent strains to each layer. Some AM processes are characterized by a tool trajectory that follows a repetitive pattern in space. In the SLM technology the laser follows a predefined island strategy. In such cases, instead of describing individual trajectories of the toolpath, it is more effective to define a scan pattern that represents the idealized motion of a tool inside a part [11].

The printed part is divided in slices of uniform thickness h perpendicular to the building direction. The scan pattern consists of a rectangular domain that is partitioned in one or more patches. Each patch can define a local angle φ and a specific value of eigenstrains as a result of a specific trajectory in that area. The eigenstrains pattern in PBF processes is related to the in-plane scanning pattern of the heat source. Figure 10 illustrates an example of a pattern with four patches and an alternative $0-90^\circ$ orientation. The software automatically spreads the pattern until covering the whole cross section of the component.

A layer-to-layer rotation angle θ can also be defined. The scan pattern is rotated:

$$\theta_i = (i - 1) \cdot \theta \quad (2.11)$$

on the i^{th} slice for $i > 1$.

For a given element, the toolpath-mesh intersection module computes the number of slices m in a given increment. It finds which pattern patch contains the centre of each slice in that element and the local orientation of that patch considering the layer-to-layer rotation θ

and the local orientation φ . The module also computes the partial volume v_f of the element below each slice. The tool-element intersection is shown in figure 11.

A scan pattern can be visualized by requesting element solution-dependent field variables as outputs and plotting them as contours over the finite element mesh. It can be helpful to ensure that the introduced inherent strains are the desired ones. Figure 12 shows an example of the inherent strains in the first principal direction ε_{11}^* for two different scanning strategies.

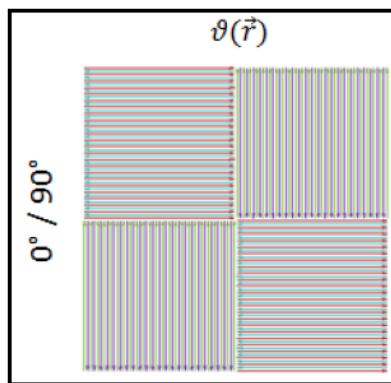


Figure 10: Example of Island pattern strategy for IS method.

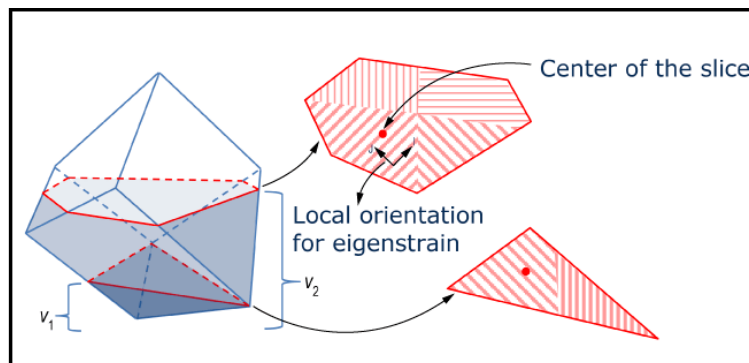


Figure 11: Scan pattern – element intersection [11].

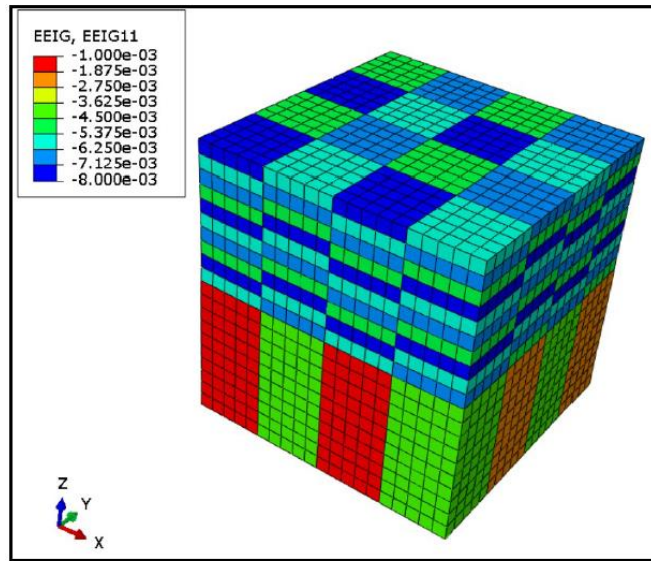


Figure 12: Visualization of the first component of the inherent strains ε_{11}^* in a simple cube.

3. Basis formulation and governing equations.

3.1. A non-linear finite element approach.

The physics behind the AM process implies the use of the non-linear finite element method. Abaqus/Standard uses the Galerkin approach to turn the governing physical equations into a weak formulation. The weak formulation results in a nodal solution vector U of temperatures (heat transfer) or displacements (structural), a residual vector R and a stiffness matrix dR/dU . From an initial estimate of the solution U_0 the Newton-Raphson method is iteratively applied using:

$$U_{i+1} = U_i - \left[\frac{dR_i}{dU_i} \right]^{-1} \cdot R_i \quad (3.1)$$

until an appropriate norm of the residual R is less than a specified tolerance. The subscripts i and $i+1$ indicate the previous and the current iteration, respectively [12]. Each time step takes the solution of the previous step as an initial estimate.

The time step integration is implemented by the backward difference algorithm:

$$\dot{U}_{t+\Delta t} = (U_{t+\Delta t} - U_t) \cdot (\Delta t)^{-1} \quad (3.2)$$

It is a simple method as it does not require any specific starting procedure. In addition, it is an unconditionally stable method which is commonly applied to problems where the solution is sought over very long periods [13].

3.2. Thermal model

In this chapter, the governing thermal equations solved by Abaqus/Standard are described together with the thermal boundary conditions needed to calculate the temperature field over the history of the building process.

3.2.1. Thermal equilibrium.

The governing equation for a body with a constant density ρ and an isotropic temperature-dependent specific heat capacity $C_p(\theta)$ is:

$$\rho \cdot C_p(\theta) \cdot \frac{d\theta}{dt} = -\nabla \cdot q(\vec{r}, t) + Q(\vec{r}, t) \quad (3.3)$$

where θ is the temperature, t the time, $\nabla \cdot$ the divergence, q the heat flux density, \vec{r} the relative spatial coordinate and Q the laser energy distribution of the expression (2.2). The specific heat $C_p(\theta)$ presents an extreme non-linearity given by the addition of the internal energy associated with the phase change (latent heat, λ) for a temperature range between the solidus and liquidus temperatures of the material (See chapter 4.2).

The distribution of heat through the part is driven by Fourier's conduction:

$$q = -k(\theta) \cdot \nabla \theta \quad (3.4)$$

where $k(\theta)$ is the isotropic temperature-dependent conductivity.

The required initial condition is:

$$\theta_0 = \theta_\infty \quad (3.5)$$

where θ_∞ is the room temperature or, eventually, the preheating temperature for the elements belonging to the build plate.

3.2.2. Boundary conditions.

A two-part Neumann boundary condition is implemented consisted of the applied heat source and the heat losses due to convection and radiation. The convection heat flux on a surface is governed by the equation:

$$q = -h \cdot (\theta - \theta^0) \quad (3.6)$$

where h is a reference film coefficient, θ is the temperature at the point of the surface and θ^0 is the reference sink temperature.

In PBF manufacturing processes it is common to have a small flow of shielding gas streaming across the build chamber to avoid burning and oxidation of the part. Commonly, the gases have whether a Nitrogen or an Argon base. The gas is not applied directly to the part,

resulting in a free convection that can be approximated as a single film coefficient value. Calibration studies show that convection coefficient values between $5\text{-}20 \text{ W/m}^2 \text{ K}$ produce accurate models [14].

The radiation heat losses are driven by the Stefan-Boltzmann law:

$$q = \sigma \cdot \epsilon [(\theta - \theta^z)^4 - (\theta^0 - \theta^z)^4] \quad (3.7)$$

where $\sigma = 5.67 \cdot 10^{-8} \text{ W/m}^2 \text{ K}^4$ is the Stefan-Boltzmann's constant, ϵ the constant surface emissivity and θ^z the value of the absolute zero of the temperature's scale. The emissivity ϵ is a material dependent property usually obtained from experimental calibration.

3.3. Continuums mechanics.

3.3.1. Elasticity.

The mechanical behaviour of a macroscopic, metallic solid body can be approximated by an elastic-perfectly plastic material model. The elastic part is described by the Hooke's law:

$$\vec{\sigma} = D(\theta) \cdot \vec{\epsilon} \quad (3.8)$$

which formulates a linear relationship between the tension and the deformation that the body experiments. This relationship in a 3D solid body is given by the so-called material elastic matrix $D(\theta)$ of the expression:

$$D(\theta) = \frac{E(\theta)}{(1-2\nu(\theta))(1+\nu(\theta))} \cdot \begin{pmatrix} 1-\nu(\theta) & \nu & \nu & 0 & 0 & 0 \\ \nu & 1-\nu(\theta) & \nu & 0 & 0 & 0 \\ \nu & \nu & 1-\nu(\theta) & 0 & 0 & 0 \\ 0 & 0 & 0 & \frac{1-2\nu(\theta)}{2} & 0 & 0 \\ 0 & 0 & 0 & 0 & \frac{1-2\nu(\theta)}{2} & 0 \\ 0 & 0 & 0 & 0 & 0 & \frac{1-2\nu(\theta)}{2} \end{pmatrix} \quad (3.9)$$

where $E(\theta)$ refers to the Young modulus and $\nu(\theta)$ the Poisson's coefficient of the material. The stress and strain vectors are given by the expression:

$$\vec{\sigma} = \begin{pmatrix} \sigma_{11} \\ \sigma_{22} \\ \sigma_{33} \\ \sigma_{12} \\ \sigma_{23} \\ \sigma_{31} \end{pmatrix}, \quad \vec{\epsilon} = \begin{pmatrix} \epsilon_{11} \\ \epsilon_{22} \\ \epsilon_{33} \\ \gamma_{12} \\ \gamma_{23} \\ \gamma_{31} \end{pmatrix} \quad (3.10)$$

3.3.2. Boundary conditions.

In order to model the physical attachment of the build plate to the printer structure, the translational degrees of freedom must be constrained at some points:

$$u_x = 0, \quad u_y = 0, \quad u_z = 0 \quad (3.11)$$

located on the bottom surface of the build plate. The mechanical and the thermal simulation are joined by the temperature field result which is introduced as a time-dependent boundary condition for the static solution. A gradient of temperature causes a deformation in the solid which depends on the expansion coefficient of the material $\alpha(\theta)$. The expansion coefficient becomes zero for a temperature over the melting point. Then, the unitary thermal strain caused by one temperature degree change is driven by the expression:

$$d\varepsilon^{th} = \alpha(\theta) \cdot d\theta \quad (3.12)$$

The accumulated deformation caused by a temperature gradient is given by the expression:

$$\vec{\varepsilon}^{th}(\theta) = \left(\int_{\theta_0}^{\theta} \alpha(\theta') d\theta' \right) \cdot \vec{I} \quad (3.13)$$

, with $\vec{I} = (1, 1, 1, 0, 0, 0)^T$ showing an isotropic material behaviour without shear deformation [10]. Then, the thermo-elastic coupling can be described by the equation:

$$\vec{\sigma} = D \cdot (\vec{\varepsilon}^{el} - \vec{\varepsilon}^{th}) \quad (3.14)$$

3.3.3. Plasticity.

Normally the behaviour of a solid body is not purely elastic. If the component is subjected to a severe overload (laser thermal load in AM), it is important to determine how it deforms under that load and if it has sufficient ductility to withstand the overload without catastrophic failure [15]. This might be answered by modelling the material as rate-independent elastic-perfectly plastic.

When the load causes stresses beyond a limit called yielding stress, the deformation become permanent and once the load is removed the body does not recover its original shape. In the plastic models provided in Abaqus, the elastic and plastic responses are distinguished by

dividing the deformation into recoverable (elastic) and non-recoverable (plastic) parts. It assumes that there is an additive relationship between strain rates:

$$\dot{\epsilon} = \dot{\epsilon}^{el} + \dot{\epsilon}^{pl} \quad (3.15)$$

When the elastic strains are small the approximation of the previous expression is consistent. The elastic strains always remain small for metals with a yield stress typically three orders of magnitude smaller than its modulus of elasticity.

There are different criteria to evaluate the overall mechanical response of a point. A reliable one for metal parts is the Von Mises Stress σ_{VM} :

$$\sigma_{VM} = \sqrt{\frac{1}{2}[(\sigma_{11} - \sigma_{22})^2 + (\sigma_{22} - \sigma_{33})^2 + (\sigma_{33} - \sigma_{11})^2 + 6 \cdot (\sigma_{12}^2 + \sigma_{23}^2 + \sigma_{31}^2)]} \quad (3.16)$$

which gives a multiaxial stress state for isotropic materials.

The origin of the plastic deformations derives from the sudden load application in the PBF processes. The large temperature gradient introduced together with the big changes in the material properties with temperature cause inherent stresses and strains in the Heat Affected Zone (HAZ). The figure 9 shows the temperature gradient effect (TGE) during heating and cooling of the HAZ. The thermal strains cause a compression in the HAZ where plastic deformations are consequently originated.

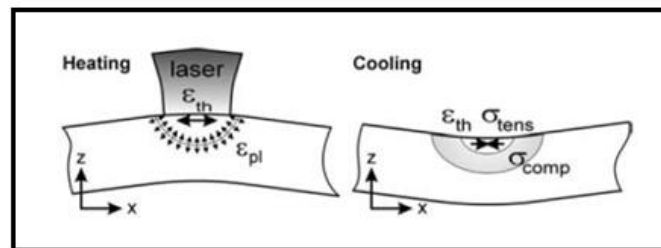


Figure 13: Stresses and strains in the HAZ during SLM process.

3.3.4. Inherent strains.

The total strain consists of the addition of elastic, plastic, thermal and creep strains [10]:

$$\vec{\varepsilon} = \vec{\varepsilon}^{el} + \vec{\varepsilon}^{pl} + \vec{\varepsilon}^{th} + \vec{\varepsilon}^{cr} \quad (2.1)$$

Assuming an elastic-perfectly plastic material model the creep component is neglected so that the equation can be redefine:

$$\vec{\varepsilon}^* = \vec{\varepsilon} - \vec{\varepsilon}^{el} = \vec{\varepsilon}^{pl} + \vec{\varepsilon}^{th} \quad (2.2)$$

where $\vec{\varepsilon}^*$ are the inherent strains composed by the plastic and thermal strains. The inherent strains tensor in three dimensions is represented with six components:

$$\varepsilon^* = \begin{Bmatrix} \varepsilon_{11}^* \\ \varepsilon_{22}^* \\ \varepsilon_{33}^* \\ \varepsilon_{12}^* \\ \varepsilon_{13}^* \\ \varepsilon_{23}^* \end{Bmatrix} \quad (2.3)$$

Once these components are known the residual stresses can be calculated in the following way: first, the eigenstrains are imposed on the non-linear elastic FEM formulation [16]:

$$[K][u] = [f^*], \quad (2.4)$$

$$f^* = \int [B] [D][\varepsilon^*] dV \quad (2.5)$$

where $[K]$ is the stiffness matrix, $[u]$ is the nodal displacement vector and $[f]^*$ is the nodal force vector introduced by the inherent strains. Once the displacement vector $[u]$ is solved using the equation (2.4), the total strain ε and the residual stress σ can be calculated:

$$\varepsilon = [B][u] \quad (2.6)$$

$$\sigma = [D^e](\varepsilon - \varepsilon^*) \quad (2.7)$$

where $[B]$ denotes the nodal deformation matrix and $[D^e]$ the elastic material matrix. The inherent strain tensor can be rotated in order to simulate different scanning strategies:

$$\mathbb{T} = R \varepsilon^* R^T, \quad (2.8)$$

$$R := \begin{pmatrix} \cos\varphi & -\sin\varphi & 0 \\ \sin\varphi & \cos\varphi & 0 \\ 0 & 0 & 1 \end{pmatrix} \quad (2.9)$$

where R denotes the rotation matrix and φ the rotation angle.

4. Material modelling.

The material properties that influence on the temperature history and, consequently, on the mechanical behaviour of the body must be accurately modelled. They frequently show a large temperature dependence which must be considered. However, the need to produce accurate models must be balanced with the computational time. The temperature-dependent properties like conductivity, specific heat capacity, density and emissivity are the source of the non-linear character of the solution. If the thermal dependence can be eliminated or decreased for any of these properties, it would decrease the non-linearity which would speed up the convergence and, ultimately, the simulation time.

An engineering analysis supported in experimental tests and validated models is needed to determine which material properties have a crucial temperature dependency and in which ones can be neglected [7].

4.1. Material selection.

The material used to print the parts is Ti-6Al-4V powder of $60 \mu m$ size. It is the most widely used titanium alloy. It offers the best all-round performance for a variety of weight reduction applications.

The properties have been provided by the Danish Technological Institute (DTI) (see Appendix A.1. for more information about DTI). Both thermal and mechanical essential properties are shown in table 1.

The density is modelled constant (at room temperature) because its change is already considered in the thermal volume change [10]. The density of the material is:

$$\rho = 4480 \text{ Kg/m}^3 \quad (4.1)$$

The temperature dependence properties can be visualized at the figures 14 and 15 for thermal and mechanical properties, respectively.

In order to couple the thermal with the mechanical simulation the temperature field result is introduced as a time-dependent boundary condition for the static solution. A gradient of temperature causes a deformation in the solid which linearly depends on the expansion coefficient of the material $\alpha(\Theta)$ illustrated in figure 16.

ρ	Density
$k(\theta)$	Thermal conductivity
$C_p(\theta)$	Specific heat capacity
λ	Latent heat of fusion
$E(\theta)$	Young modulus
$\nu(\theta)$	Poisson coefficient
$\alpha(\theta)$	Expansion coefficient

Table 1: Material basic properties.

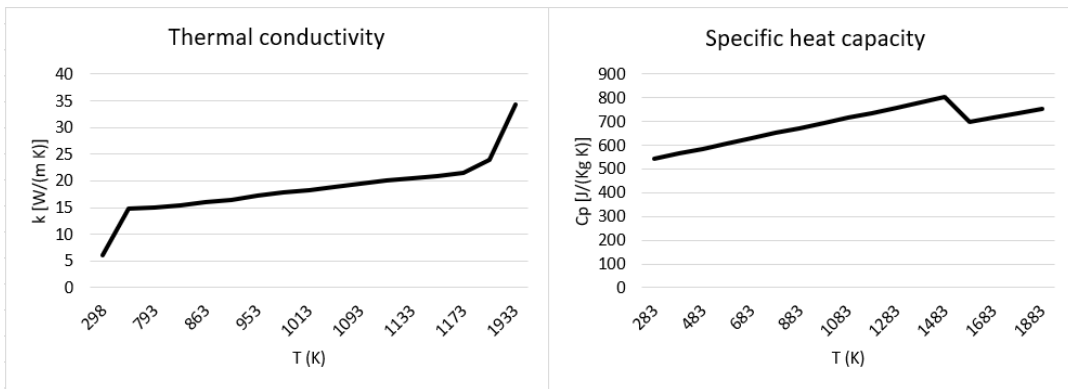


Figure 14: Ti6AlV4 thermal properties evolution.

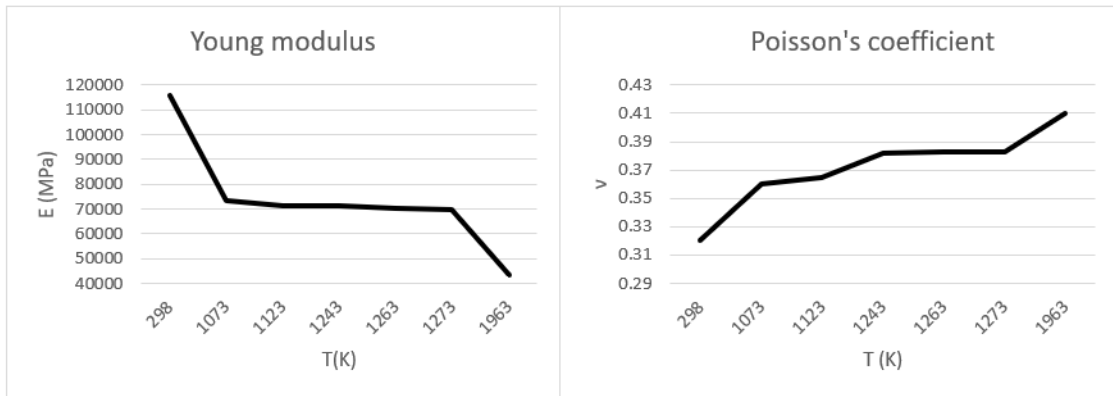


Figure 15: Ti6AlV4 mechanical properties evolution.

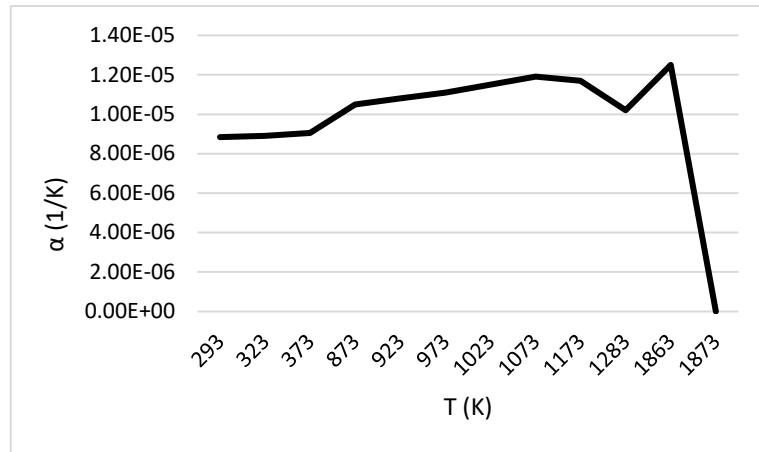


Figure 16: Ti6AlV4 thermal expansion coefficient.

4.2. Latent heat effect

In order to capture the change of phase the temperature limits for the solid and liquid state are required:

$$\theta_{solidus} = 1823 \text{ K}, \quad \theta_{liquidus} = 1873 \text{ K}, \quad \lambda = 419000 \text{ J/Kg} \quad (4.2)$$

They define the range of temperatures where the latent heat λ is applied. The latent heat is the extra energy required to make the phase change in the material in form of thermal energy absorption (melting) or release (solidification). The value of the latent heat for metals is roughly 100-1000 times the specific heat capacity. The latent heat magnitude for the Ti-6Al-4V alloy is given by the expression (4.2). It adds an extreme non-linearity in the thermal solution which may inhibit convergence. The high change in the internal energy of the body caused by the latent heat can be visualized in figure 17. The non-linearity can be smoothed in Abaqus by extending the temperature range of application.

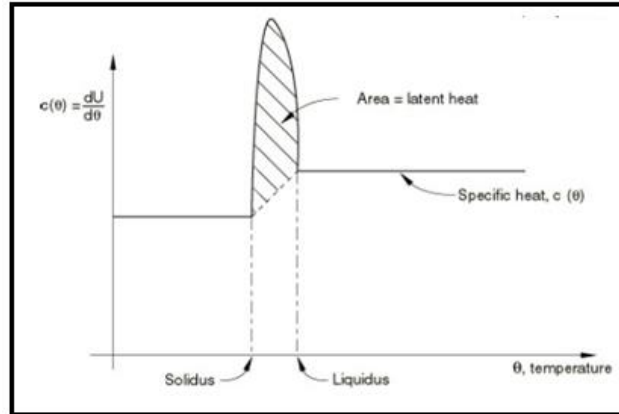


Figure 17: Latent heat effect in a metal [9].

4.3. Plasticity model.

An elastic-perfectly plastic behaviour is defined for the material. The yield stress σ_y as well as the ultimate stress σ_U and elongation ε_U extracted from the manufacturer at ambient temperature are:

$$\sigma_y = 770 \text{ MPa}, \quad \sigma_U = 770 \text{ MPa}, \quad \varepsilon_U = 0.1 \quad (4.3)$$

A strain rate independent plasticity is assumed. When the temperature of a material point exceeds a user-specified value called the annealing temperature, Abaqus assumes that the material point loses its hardening memory. Depending on the temperature history a material point may lose and accumulate memory several times, which in the context of modelling melting would correspond to repeated melting and re-solidification [9]. In order to determinate this temperature it must be considered that metals lose most of its strength as getting closer to the melting temperature. It is a good practice to take a value of $100\text{-}200^\circ\text{C}$ below the solidus temperature and assign to it a low yield stress of a 10% of the room temperature one, assuming perfect plasticity [7]. Thus, the annealing temperature in this model is set to 1673 K .

The complete plastic model can be visualized in figure 18. Commonly in metals, the yield stress at a fixed strain rate decreases with an increasing temperature.

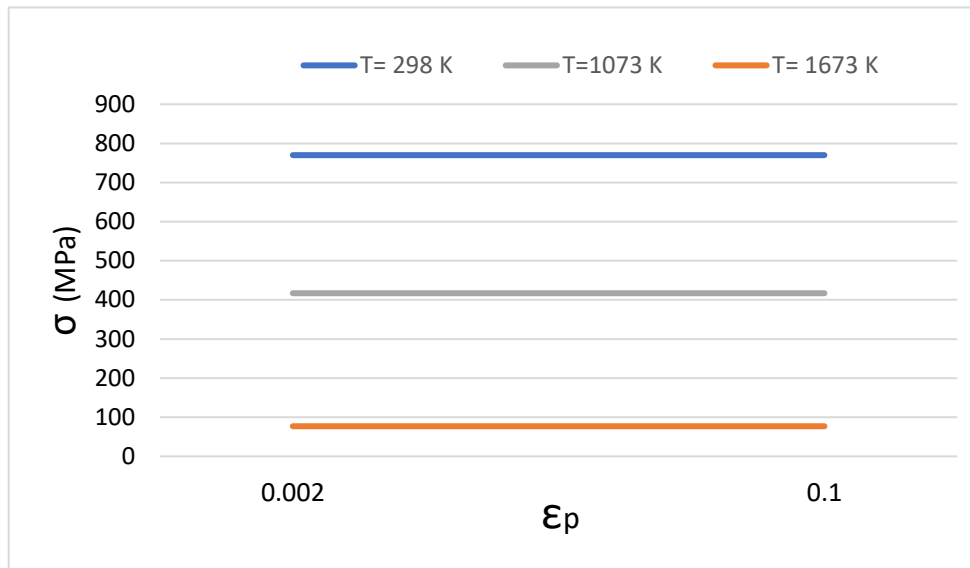
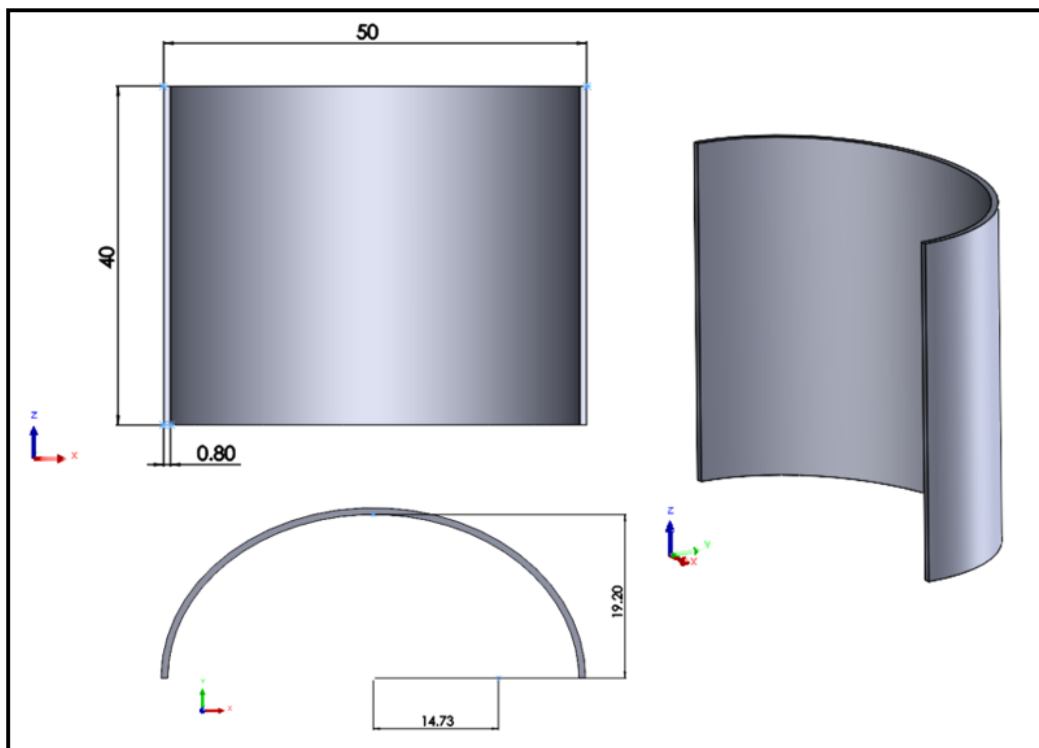


Figure 18: Plasticity model with temperature effect.

5. Geometry selection.

The geometry of the component used in this work is a simplified thin-walled structure which was provided by the Oqton® company (see Appendix A.1. for more information about Oqton). This type of structure can be used to capture the challenges involved in the printing of dental stents. The curved-shape geometry can be visualized in figure 19. The dimensions are expressed in millimetre. The size of the original part led to an unfeasible computational time when running a model that captures the physical melting-solidification effect involved in SLM processes. Thus, all the dimensions of the original part are scaled 1:5 except for the thickness 1:2. The part thickness lays on the minimum value recommended to print accurately of 0.4 mm [1]. The resulting scaled geometry is depicted in figure 20.



*Figure 19: Front and top views (left) and isometric view (right) of the Real part.
Dimensions in mm.*

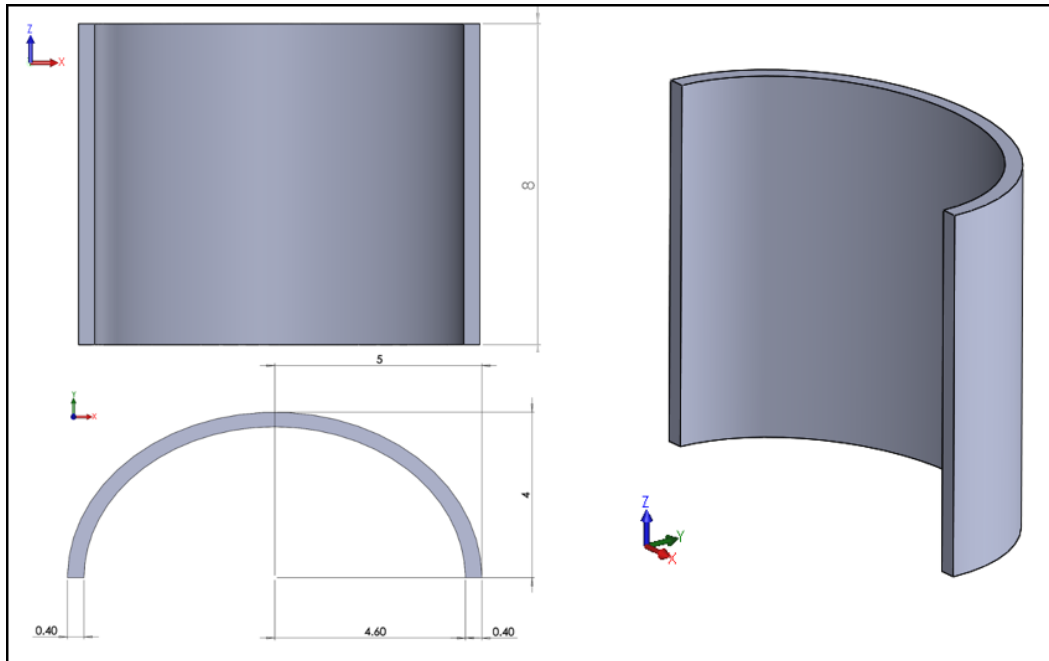


Figure 20: Front and top views (left) and isometric view (right) of the Scaled part. Dimensions in mm.

6. Scaled model.

Two models are presented using the sequential thermo-mechanical method based on the fidelity of the solution: High Fidelity (HF) and Medium Fidelity (MF). The main differences are the spatial and time discretizations. The following sections describe the part fixing, scanning strategy, solution fidelity, boundary conditions, process parameters, discretization and results.

6.1. Part-fixing.

The part is directly attached to a flat build plate which acts like a heat conduction sink. There are not supports that connect the build plate with the part. The build plate dimensions are shown in figure 21. The build plate is from the same material as the part.

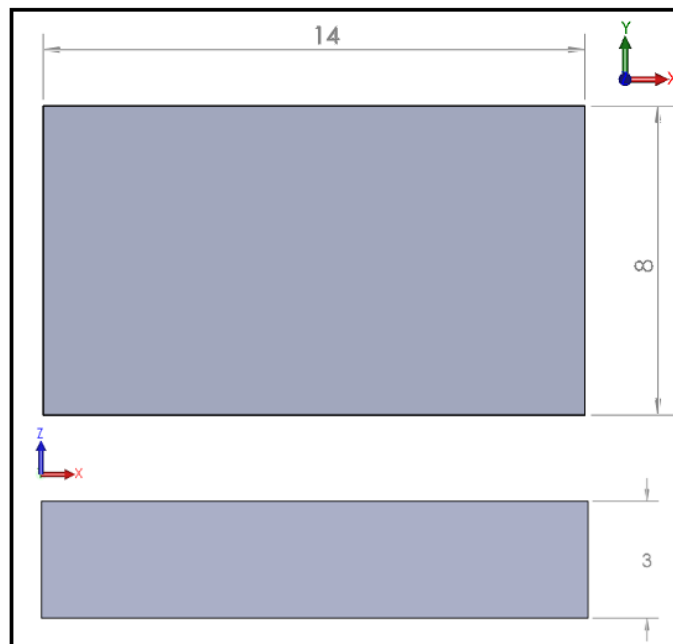


Figure 21: Build plate top and front view. Dimensions in mm.

6.2. Tool path and scanning strategy.

The laser movement along the part as well as the roller deposition are introduced in Abaqus AM plug-in through event series files. In order to create those files first a code with the tool instructions must be obtained. For that purpose, the open-source software ReplicatorG® is used. The part is imported as a stereolithography (STL) file and located on the centre of the build plate. Then, the slicing profile is edited with the parameters of the process summarized in table 2. The infill track speed is higher than the contour one to compensate the heat accumulation inside the part. The generated Gcode is translated into the laser and roller event series by a Python® script provided by Simulia Dassault Systems®. The user introduces the laser power, the roller deposition time and the roller position on the build plate. The values are 250 W, 1 s and 0.5, respectively. The last value means that the roller is located in a centred position related to the part.

The resulting laser scanning movement over one layer of the part is depicted at the figure 22. The orientation of 90° from the x-axis is given to ensure short straight tracks of the laser which has a better effect in the distortion than long tracks [17]. The laser takes 59 ms to complete one layer.

Printing parameter	Value
Object infill (%)	100
Layer height (μm)	80
Laser diameter (μm)	60
Feed rate (mm/s)	1200
Perimeter feed rate multiplier	0.75
Infill rotation (°)	90

Table 2: Laser scanning parameters of the Scaled model.

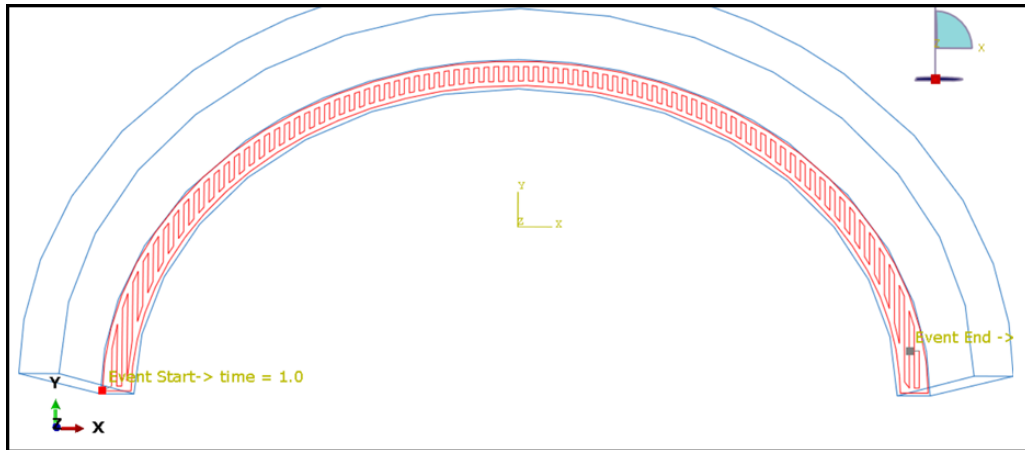


Figure 22: Scanning strategy of the Scaled model.

6.3. Level of fidelity.

AM is a multiscale problem in both time and space. Abaqus allows to control the scale as well as the fidelity of the solution through the mesh size and the time step incrementation. Typically, there are two types of thermo-mechanical simulations at the end of the fidelity spectrum: process-level simulation (High fidelity) and part-level simulation (Low fidelity) [9]. In this work, the thermo-mechanical part-level simulation is named “Medium fidelity” in order to make a difference with the purely mechanical Inherent Strains (Low fidelity) simulation.

A detailed process simulation is performed using:

- A refined mesh size: at least one element per powder layer thickness and a few elements across a section affected by the melting.
- A small-time increment: typically of the order of milliseconds.
- A volumetric input tool geometry together with a detailed laser energy distribution.

This detail level allows to capture the fast and large temperature gradients evolving in the HAZ, providing an accurate outcome of residual stresses and distortions. The thermal energy release and absorption is modelled using the latent heat of fusion in the thermal model. In the mechanical model the annealing temperature applied in the plasticity model of the material (see section 4.3) captures the effect of the melting on the thermal strains. This type of simulation, on the other hand, demands a high computational cost. It can also be affected by convergence issues caused by the non-linear material properties under rapidly changing temperature conditions.

A part-level simulation is performed using:

- A coarse mesh: a few physical layers per element.
- A big-time increment: the time sequence of events is lumped. One or several time increments per element layer.
- A discrete point tool geometry without laser energy distribution.

The heat transfer analysis can usually capture far-field temperatures (away from the HAZ) but may not capture the local rapid temperature evolution because the moving of the heat source is lumped in space and time. Thus, the results do not usually contain an accurate melting and solidification history. To correctly model melting effects in the stress analysis, a temperature must be assigned representing the relaxation temperature of the material above which thermal straining induces negligible thermal stress [9]. Upon element activation, the relaxation temperature is the temperature from which the initial thermal contraction occurs and can be calibrated from experimental tests or detailed-process level simulations. In this case, the relaxation temperature $\Theta_{SR} = 963 \text{ K}$ for Ti-6Al-4V is extracted from the literature [7]. It is implemented in the plasticity model of the material. The part-level simulation is computationally efficient for the prediction of distortions and stresses in printing parts with a reasonable accuracy [9].

The aforementioned suggestions for mesh size and time step increment are approximations and both space and time discretization must be specifically determined for each printing case through the corresponding convergence studies.

6.4. Boundary conditions.

The Boundary Conditions (BC) play an important role in the correcting modelling of the process.

The thermal and mechanical models experience different BCs. In the thermal model a preheating temperature is applied on the bottom surface of the build plate equivalent to $400 \text{ }^\circ\text{C}$. It remains constant during the whole printing time. The preheating of the build plate helps to decrease the residual stresses presented at the bottom of the part and to improve the mechanical properties of the material [18]. On the other hand, a room temperature of $40 \text{ }^\circ\text{C}$ is set to the remaining free surfaces of the part and build plate. It comes from a typical Argon atmosphere in the printer chamber [19].

In the mechanical model the principal BC is the fixing constrain of the bottom surface of the build plate. The three degrees of freedom belonging to the displacement are limited to zero. It avoids distortion alien to the printing process. In addition, the thermal transient temperature field resulting from the heat transfer analysis is applied to the entire model.

6.5. Interactions.

In this section the contact interaction between the build plate and the part is modelled. In the thermal model a “tie” constrain is implemented which unifies the temperatures of the two surfaces in contact. The surface in contact can be visualized at the figure 23. The fixturing losses from the build plate to the machine are ignored. It is a fair modelling choice when the part is relatively small and the build plate does not heat up [7].

The same surface is used to apply the interaction for the structural analysis. Again a “tie” condition is applied, meaning that the nodes belonging to the two components unify their translational motion.

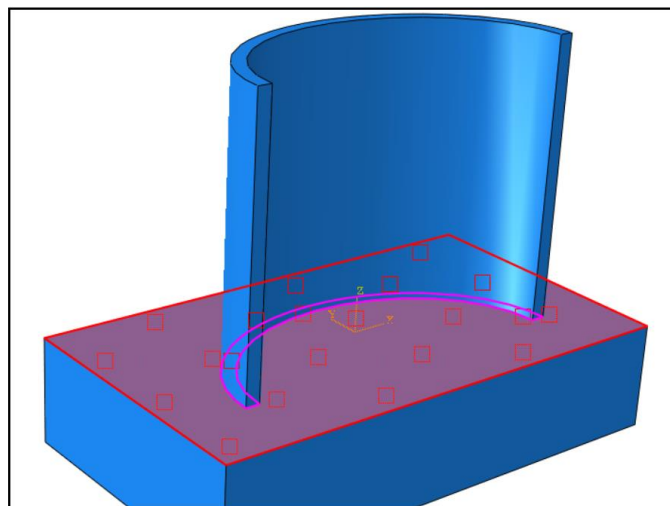


Figure 23: Contact surface (pink) between the build plate and the part.

6.6. Printing parameters.

There are different parameters that enable a customization of the printing process. For example, the energy absorption coefficient, the laser energy distribution parameters, the type of element activation or the behaviour of the inactive elements.

An absorption coefficient η equal to 0.46 is selected. This value had the best agreement with experimental results in a previous study of the same material Ti-6Al-4V under the effect of a laser radiation [20]. An accurate value of this parameter is important because it limits proportionally the amount of energy that the part gets from the laser.

The parameters belonging to the Goldak's spatial energy distribution are summarized in the table 3. They correspond to the melting pool dimensions in millimetre calibrated in Keller's experimental-simulation work using similar printing conditions [10].

The elements are partially activated to fit the cases when the thickness of the physical powder layer does not match the finite element height. According to the heat energy balance experiment in a unitary element cube, the partial activation keeps accurate temperature results [20].

Finally, the follow deformations option determines whether or not the inactivated elements are allowed to move and follow the predicted deformation of the part. By default, elements that are inactive do not contribute to the overall response of the model and their degrees of freedom are not part of the solution. In stress-displacement analyses this approach works only if displacements are relatively small. If that is not the case, the inactive elements may become excessively distorted before they get activated, which may cause convergence difficulties or produce poor results [21]. Thus, the option is activated. A model validated by the National Institute of Standards and Technology (NIST) activated the deformations [22].

Parameter	Value
a	0.03
b	0.085
c_f	0.03
c_r	0.03
f_f	1
f_r	1

Table 3: Laser energy distribution parameters. Equation (2.2).

6.7. Cooling.

Convection and radiation are the two heat-transfer mechanisms of cooling to the environment. Both are subjected to a sink temperature corresponding to the room temperature of 40 °C.

A typical film coefficient h for inert gas atmosphere of 18 W/m^2K is set to all the free surfaces of the model except the bottom surface of the build plate [19]. The key-parameter in the radiation is the emissivity ϵ of the surface exposed to the atmosphere. The value selected is 0.201 defined in a previous study for the same material and similar process [23].

The cooling is continuously applied during the whole part printing time of 106 seconds and an extra cooling time of 120 seconds.

6.8. Mesh.

The element used in both thermal and mechanical models is a 3D 8-nodes linear brick element shown at the figure 24. The designation for the heat transfer element is DC3D8 and for the structural element C3D8.

The spatial distribution of the elements is uniform or “mapped” along the printed part. The build plate presents a progressive refinement when getting closer to the part location. The proposed mesh distributions are depicted in figure 25 for the part and build plate.

The size of the elements influences the results of the printing simulation. A convergence study is done in each model to the part mesh in order to obtain accurate results in a reasonable computational time. The studies are described in Appendix A.2.1. resulting in an element size of 0.8 physical layers per element for the HF model and 3 physical layers per element for the MF model. Consequently, the mesh of the part is formed by 187866 and 11237 nodes for the HF and MF models, respectively.

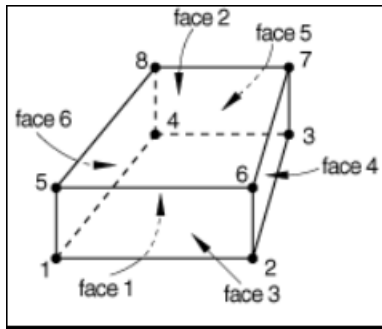


Figure 24: 8 node linear brick element.

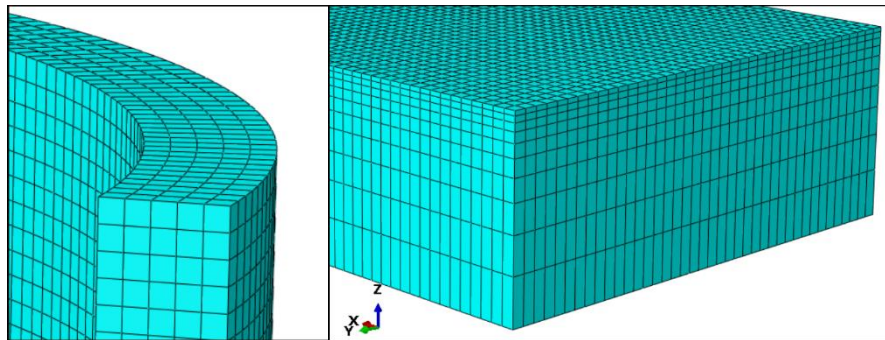


Figure 25: Mesh distribution for the part (left) and the build plate (right).

6.9. Time-stepping

The printing of a single layer is divided in two time periods with very different requirements. The period belonging to the layer deposition and subsequently the laser melting period. The layer deposition takes 1 s and can be modelled with a coarse time step as there is not any change in the temperature trend during this period. A single time increment is implemented.

On the other hand, the laser movement requires a finer time increment to capture the high gradient of temperature along the part cross section. A time stepping convergence study is necessary to select an increment refined enough but avoiding an unfeasible computational cost. The convergence studies of the thermal and mechanical HF solutions are described in Appendix A.2.2. The thermal history evaluation of the part revealed an efficient time increment of 0.75 ms for the HF model and 0.35 s for the MF model.

The thermal temperature field of the HF model introduces a huge amount of data in the mechanical model. In order to save computational resources, the mechanical results are evaluated in a reduced model representing the first ten printed layers.

The mesh is the same as in the thermal model in order to avoid extrapolation errors at transferring the temperature between dissimilar meshes. The evaluation of the displacement and stress fields revealed an efficient time increment of 1 ms for the HF model and 0.146 s for the MF model. Both completed convergence studies are described in Appendix A.2.2.

6.10. Results.

With the proper space and time discretization selected, the sequential thermo-mechanical model is solved. The asymmetric matrix storage and solution scheme is activated to avoid convergence problems caused by the asymmetric system of equations introduced by the temperature-dependent conductivity of the material [9].

6.10.1. Thermal results.

6.10.1.1. High Fidelity model.

The new and refined time step increment increased excessively the magnitude of the temperature using the original power of 250 W . Thus, a calibration of the power is carried out to save energy of the system but ensuring that the material melts (over 1873 K). The result provided a power of 160 W for all the layers except for the first one of 100 W .

The melting pool is analysed for an infill track of the laser path. The large gradient of temperature caused by the fast movement of the laser is shown in figure 26. The real molten pool shape is depicted at the figure 27. There is a full melting of the part's cross section. In addition, the melting pool penetrates the layer underneath causing a partial re-melting.

The temperature history is analysed to have a quantitative and detailed view of how the printing process thermally affects to a point of the part. Figure 28 shows the thermal history of node 971 located at the contour of the fourth layer of the part. The graph is limited to the printing of the first 10 layers. The first heating-cooling cycle is described below:

- [0, 2.117] s: Printing of the previous layers. The temperature is equal to the room temperature.
- [2.117, 3.118] s: Layer deposition. Fast raise from room temperature to previous layer temperature.
- [3.118, 3.134] s: Laser approximation. Smooth temperature raise.
- [3.134, 3.135] s: Laser melting. Extremely fast temperature gradient causing melting of the material.
- [3.135, 3.155] s: Cooling. Exponential decrement while the laser melts the remaining contour plus the initial infill.
- [3.155, 3.157] s: Laser close pass. Infill track causes a high heat.
- [3.157, 3.176] s: Cooling. Infill track last section melting. Low cooling rate.
- [3.176, 4.176] s: Cooling. Next layer depositing period. High cooling rate.

The following cycles show a flattening of the temperature peaks. No re-melting noticed. The infill track has a bigger influence on the heating than the contour track as the part builds up. The temperature seems to get stabilized around 700 K (close to the preheating temperature of the build plate).

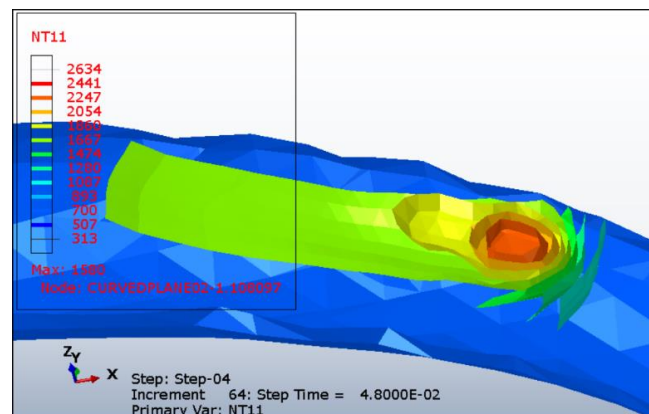


Figure 26: Iso-surface representation of the melting pool gradient of temperature for the HF model.

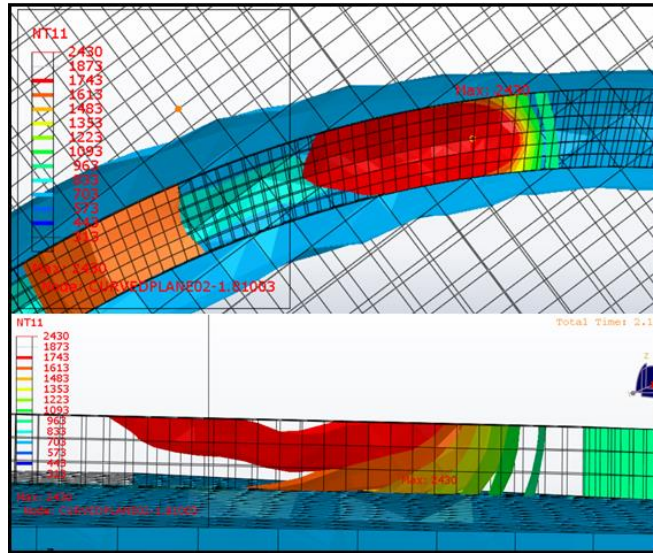


Figure 27: Cross section (Top) and depth (bottom) views of the melting pool (red) for HF model.

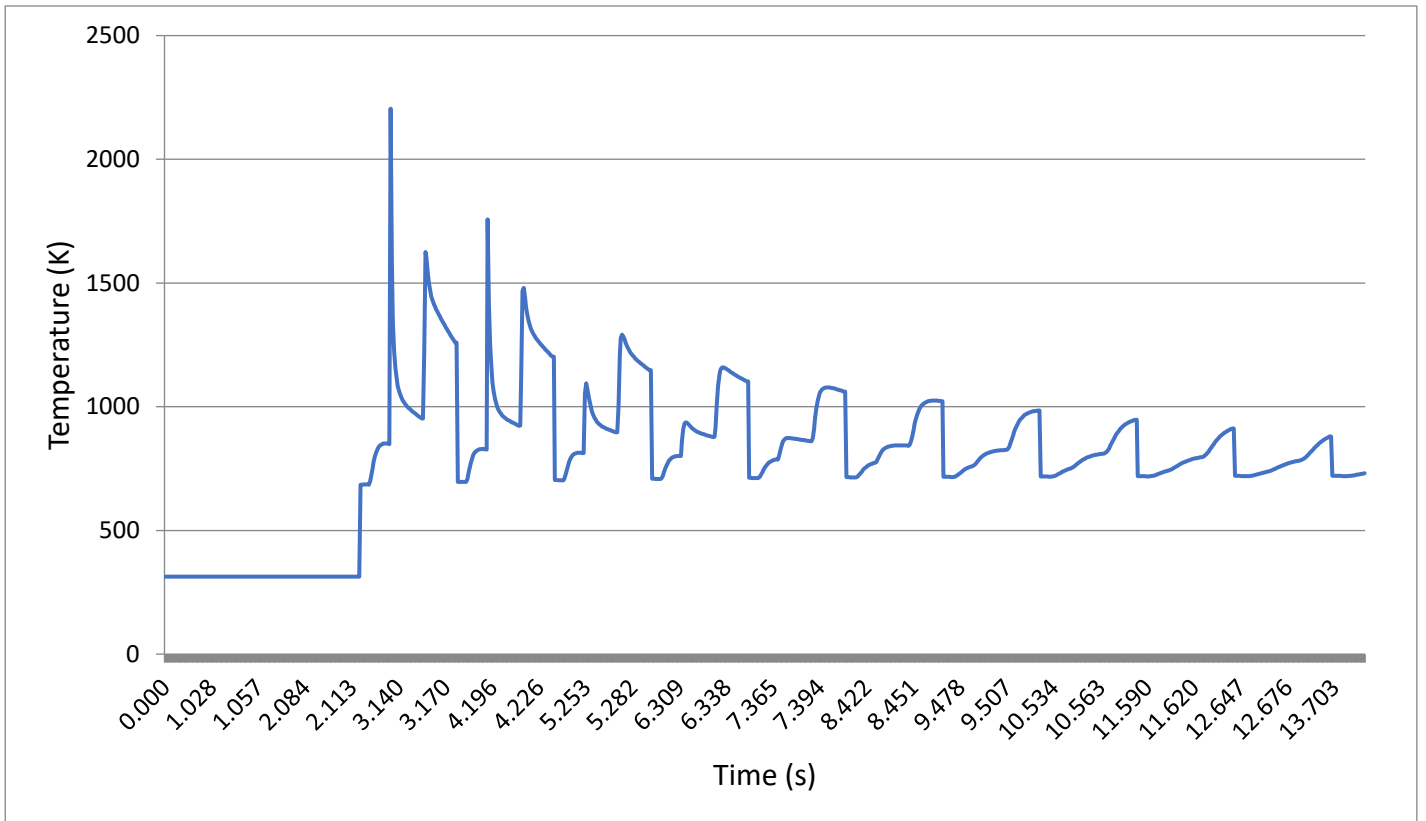


Figure 28: Thermal history of the node 971 for the HF model.

6.10.1.2. Medium Fidelity model.

The MF model only captures the thermal effect of the main stages of the building process. Figure 29 shows the thermal history of the node 4759 located on the centred location illustrated in figure 30. The output frequency is once per printed layer. The whole printing process is simplified to four stages:

- [0, 44.5] s: Printing of the previous layers. The temperature is equal to the room temperature.
- [44.5, 47.6] s: Laser heating. Layer activation and three layers scanning to the maximum temperature.
- [47.6, 105.8] s: Cooling. Smooth temperature decrease as the laser heats the remaining layers overhead.
- [105.8, 225.8] s: Cooling. High cooling rate once the printing ends. Exponential decay to the room temperature.

The peak of maximum temperature takes three depositions because the element height of the MF model is three physical layers. The slow temperature decrease during the printing time is influenced by the constant preheating temperature of 673 K applied on the build plate.

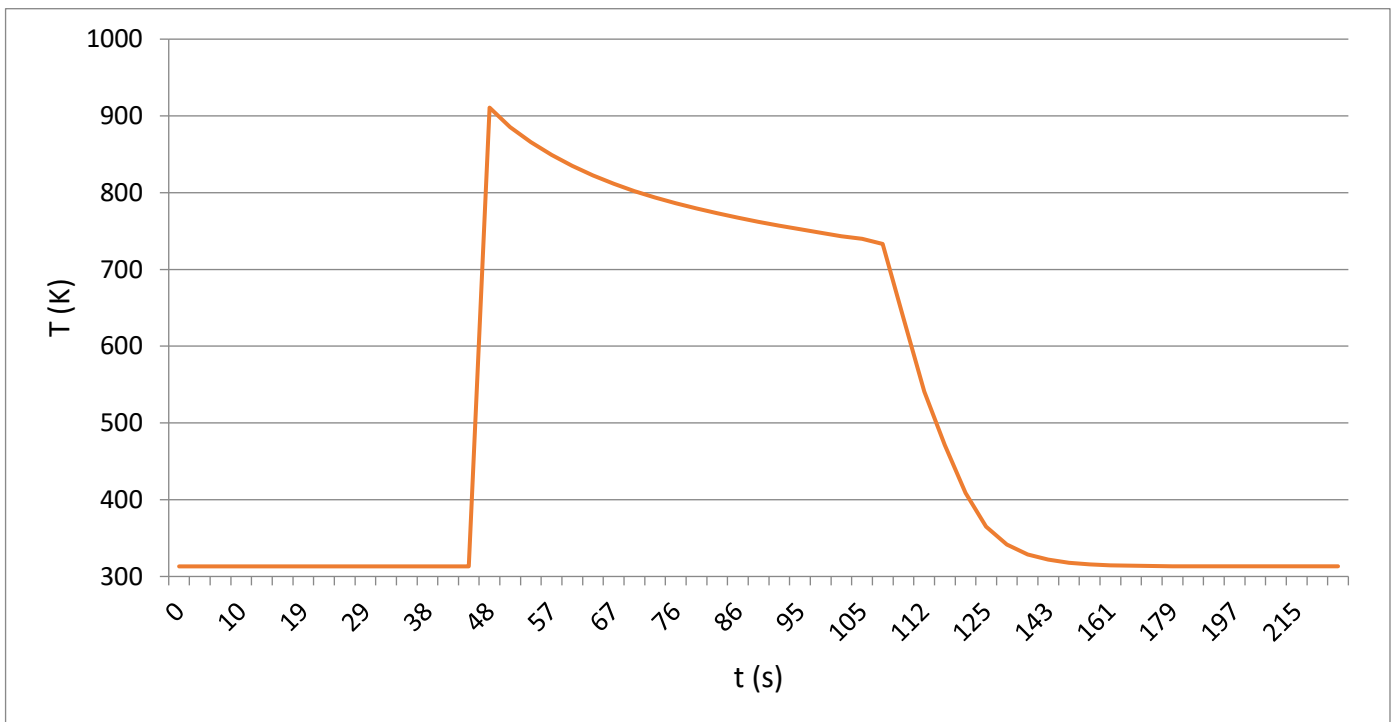


Figure 29: Thermal history of the node 4759 for the MF scaled model.

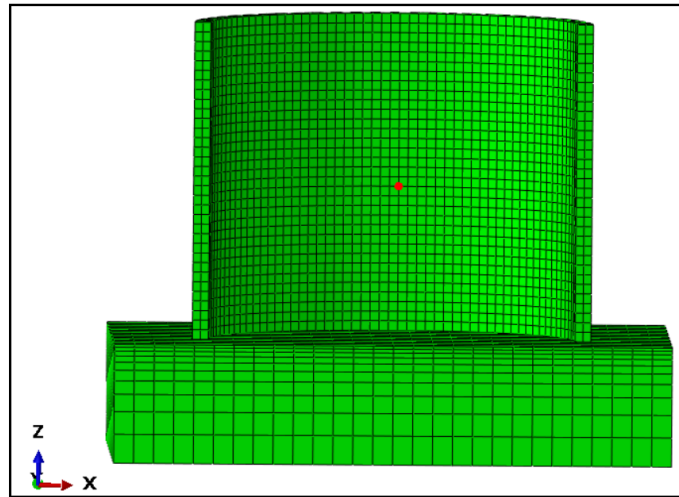


Figure 30: Node evaluated (red point) for the MF scaled thermal history.

6.10.2. Mechanical results.

6.10.2.1. High Fidelity model.

The deformed shape of the part is evaluated after the printing period and the components of the distortion are shown in figure 31. The part gradually expands in *X-direction* from the centre to the edges. The top left corner distorts an additional 60 % compared to the right one. The reason could be linked to the thermal history of both sides. There is a 200 K temperature difference between both locations on every printed layer whose effect gets accumulated over the building process. The thermal fields are depicted in figure 32 for the left and right side of the part. This effect comes from the differences in the tool-path trajectories between both sides. On the left side there is a sharp ending that makes the laser spend more time at the same location whereas on the right side there is a smoother ending enabling a wider distribution of the power along the edge. The part also expands in the *Y-direction* as can be visualized in figure 31. The location of the maximum distortion is shifted from the centre of the part to the left side due to the aforementioned singularity. Finally the distortions in *Z-direction* have a small influence on the overall distortions. The magnitude again increases on the top left corner of the part.

Figure 33 shows that the maximum Von Mises stress of 772 MPa is located on the same side than the maximum distortions. The stress magnitude barely overpasses the yielding stress limit of 770 MPa defined in the elastic-perfectly plastic material model. The stress field is more

significant on the side with larger deformations. In addition, the interlayer residual stresses are visibly widespread along the cross section.

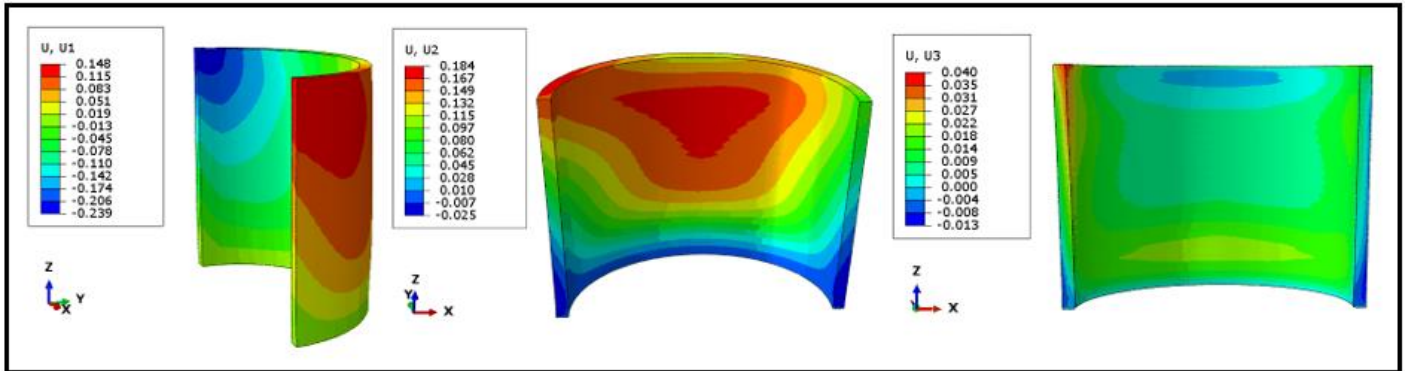


Figure 31: Distortions in X-direction U1 (left), Y-direction U2 (centre) and Z-direction U3 (right) for the HF model. Units in mm.

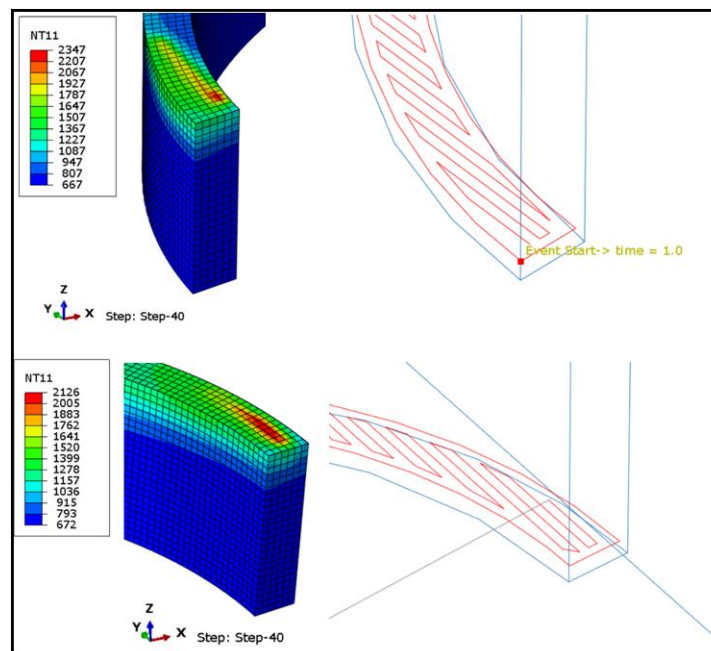


Figure 32: Temperature field comparison between left side (top) and right side (bottom) of the HF model. Toolpath depicted in red on the right.

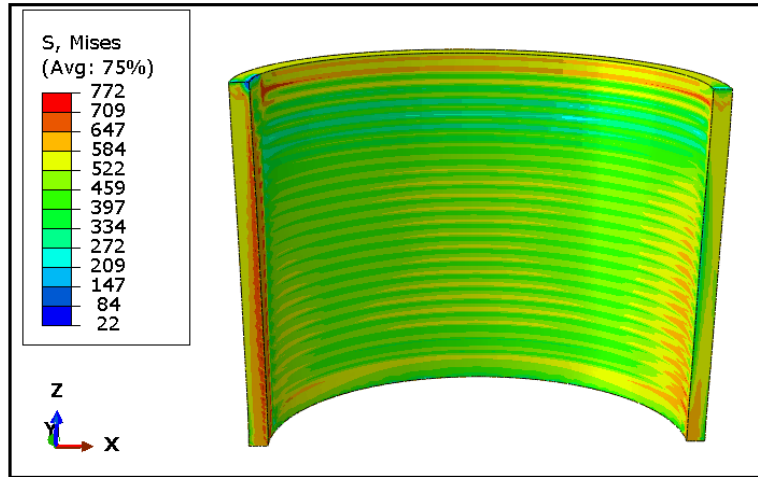


Figure 33: Von Mises stress σ_{VM} (MPa) for the HF model.

6.10.2.2. Medium Fidelity model.

The distortion and the stress states of the part are also evaluated right after concluding the printing. The output variables are the projections of the displacements over the principal directions U_x , U_y , U_z (mm) and the Von Mises stress σ_{VM} (MPa). The distribution of the distortions is depicted in figure 34. There is a symmetric distribution related to the YZ -plane in the three components. The part expands in the three principal directions with larger effect on X - and Y - than on Z -direction. The maximum displacement in X -direction of 0.097 mm is located 20 layers under the top surface and the displacement in Z -direction gradually increases from the bottom to the top of the part.

The stress state of the part is illustrated in figure 35. The largest stresses are located on the external face along the side and top edges of the part. The maximum stresses clearly overpass the yielding limit of 770 MPa. This effect is caused by the value extrapolation from the Gauss points to the nodes of the elements. The coarse mesh of this model also leads to a stress singularity inside the part which can be visualized in figure 35.

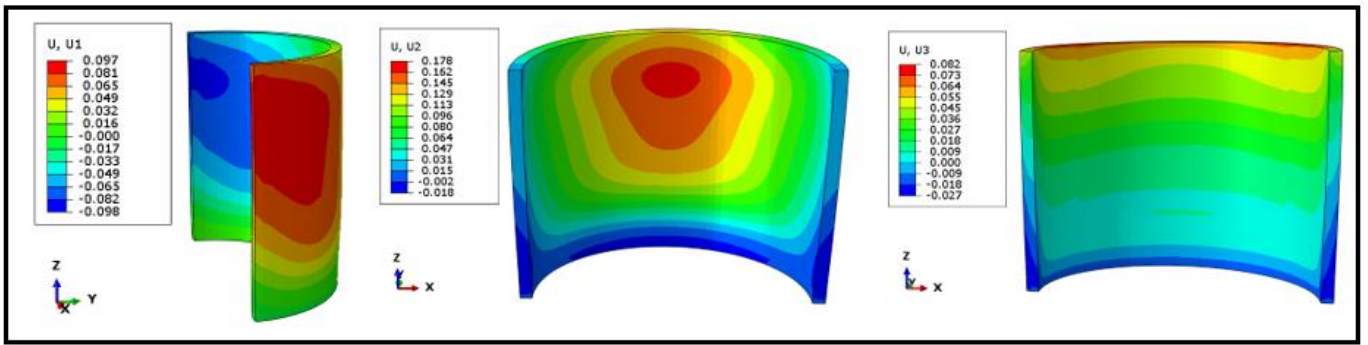


Figure 34: Distortions in X-direction U_1 (left), Y-direction U_2 (centre) and Z-direction U_3 (right) for the MF scaled model. Units in mm.

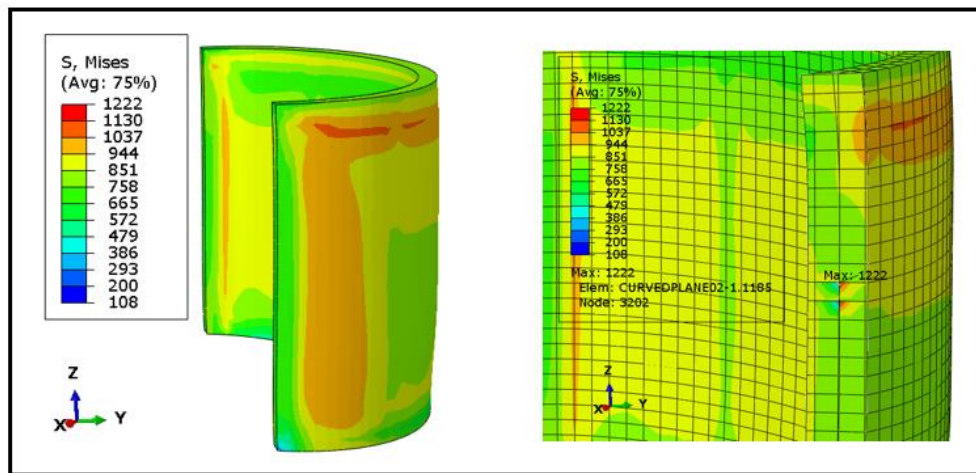


Figure 35: Von Mises stress σ_{VM} distribution (left) and stress singularity (right) for the MF model.

6.10.3. Models comparison.

Both HF and MF models experience an expansion behaviour with similar distributions but with differences in the magnitude of the distortions. Figure 36 shows the locations evaluated for the comparison between both models. The corner point for U_x and the centred point for U_y . The MF model presented a U_x decrease of 52 % related to the HF model. On the other hand, the top centre of the MF model presents a U_y difference of 5 % related to the HF value. The reason probably is the laser scanning strategy (see Section 6.2.). The longer tracks on the edges of the part result in an increment of the distortions. This effect is captured in the HF model but not in the MF due to its lumping discretization in space and time. The difference in the distortions in Z-direction is originated in the discretization of the laser energy distribution. The volumetric

shape introduced in the HF model without an experimental validation led to the uneven distribution illustrated in figure 31. On the other hand, the laser discretization as a point, characteristic from the MF model, led to a uniform distortion along the cross-section illustrated in figure 34.

The local effect presented in the left edge of the HF model contributes to the results' differentiation. In order to avoid the singularity of the corners, the deformed cross-sections at a height of 4 mm (half of the part) are compared in figure 37. The contours of the part match with a maximum distortion difference of 0.05 mm on the left side of the part.

The stress distributions of both models showed concentrations along the side and top edges of the part. In addition, the MF model presented the extrapolation and the singularity errors that resulted in an overestimation of the residual stresses.

A comparison with experimental results must be carried out in order to find out what model adjusts better to the real state of the printed part. This is the objective of the chapter 7. of this work where the MF model is implemented in an industrial size part and the results are compared with the actual distortions.

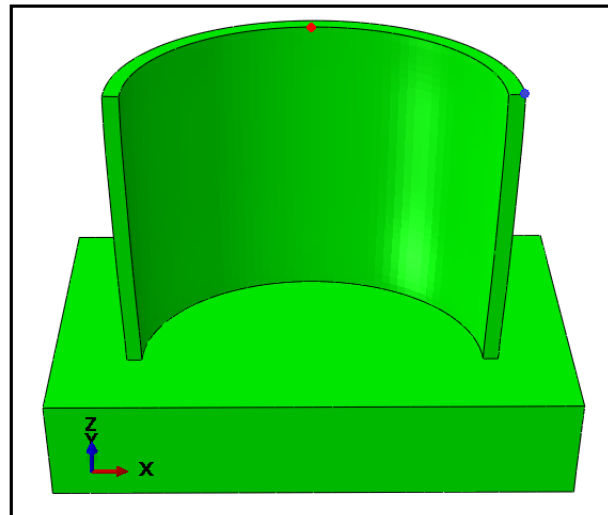


Figure 36: Locations evaluated for the models' comparison of U_x (blue) and U_y (red).

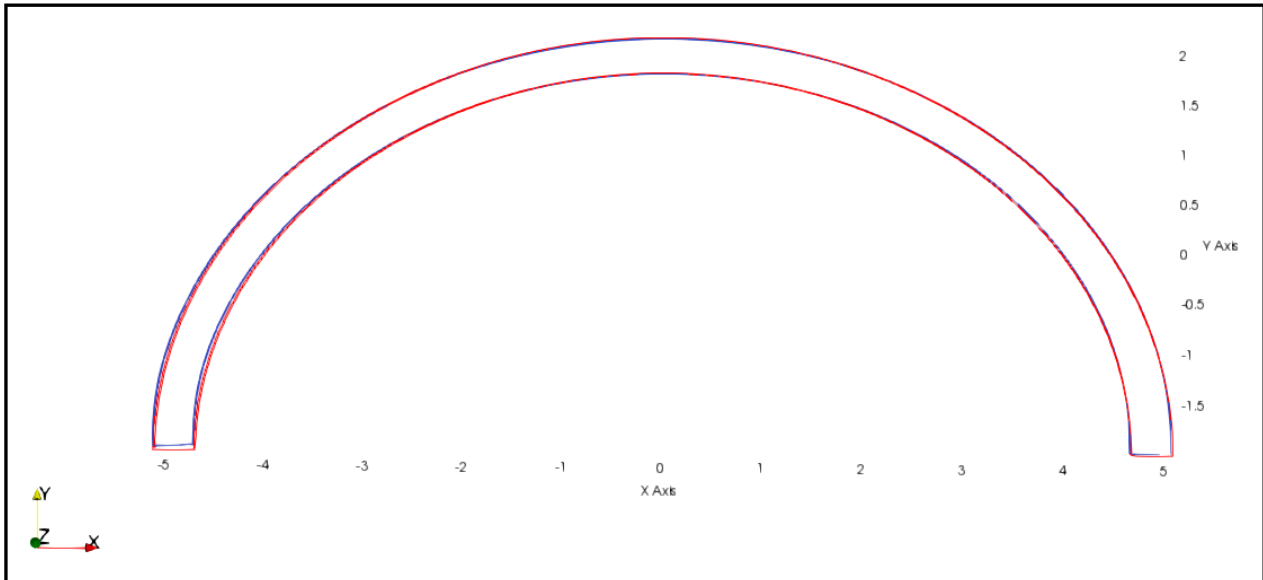


Figure 37: Cross-sections at $z = 4$ mm of the MF model (red) and HF model (blue) after print. Measurements in mm.

6.10.4. Computational cost.

The HF model involves high computational costs. The thermal model took *60 hours* of running time whereas the mechanical model needed *108 hours* to be completed, making a total simulation time of *7 days*. In addition, the output data required a total space of *41 GB*.

On the other hand, the MF model needed only *32 minutes* to complete both the thermal and the mechanical simulation and the memory requested *45 MB*.

The running time is measured from the instant the job is submitted to the end of the process solution. The simulations run in parallel using a total number of 24 CPUs from the computer CLUSTER provided by DTU (Technical University of Denmark) which contains different hardware components [24].

7. Real model.

In this section the different simulation methods are evaluated with the help of experimental results.

The geometry has the size of a typical part manufactured using the SLM technology. The dimensions of the geometry are shown in figure 19. The thermo-mechanical and the pure mechanical Inherent Strains (IS) methods are implemented. The MF model approach is used in the thermo-mechanical simulation. The long printing time required makes the HF model unfeasible for this printing simulation.

The new modelling includes all the stages of the actual manufacturing process: part printing, heat treatment and removal from the build plate. This allows to check the accuracy of the simulations in different points of the process.

The material properties and the cooling conditions are similar to the Scaled model.

7.1. Part-fixing.

The part is connected to the build plate using supports. The supports play an important role in the SLM process. They have three utilities [1]:

1. The support offers a platform for the next layer to be built upon. For that purpose, supports structures are printed first and then the part's section is built over them.
2. Support anchors the part to the build plate increasing stiffness and holding thinner features in place.
3. The support acts like an excellent heat sink, especially when they have a lattice structure. They draw heat away from the printed part allowing to cool at a more controlled rate.

In addition, the supports allow to remove easier the part from the build plate. However, cutting tools are usually required. Generally, the more supports included in the model, the more accurate the printing will be, but the higher cost and post-processing time will be required.

Figure 38 shows the geometry of a single support. It is a 4 mm high and bulk cylinder with a smooth diameter reduction on the edge connected to the part in order to facilitate the

post-processing work. The distribution of the supports along the bottom cross section of the part is depicted in figure 38. They are evenly spaced.

The third element of the assembly is the build plate which constrains the movement of the part and also acts as a heat conduction sink. The dimensions of the flat build plate are specified in figure 39. The size is reduced to the part dimensions in order to save computational resources. The material of the build plate is the same one used in the part and supports.

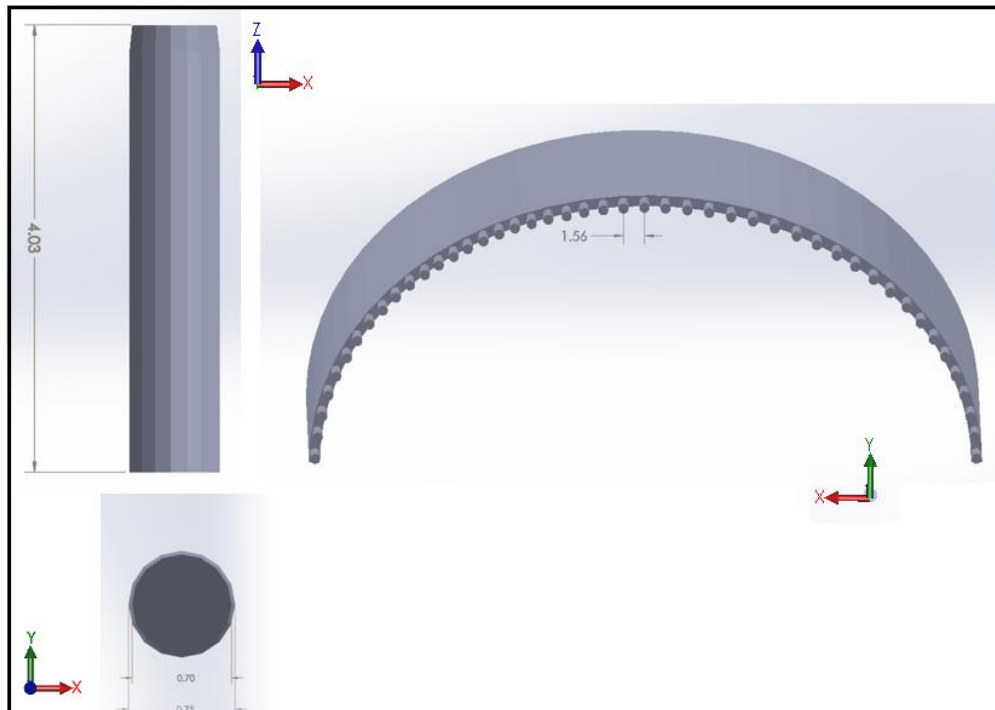


Figure 38: Support's geometry (left) and distribution along the part (right). Dimensions in mm.

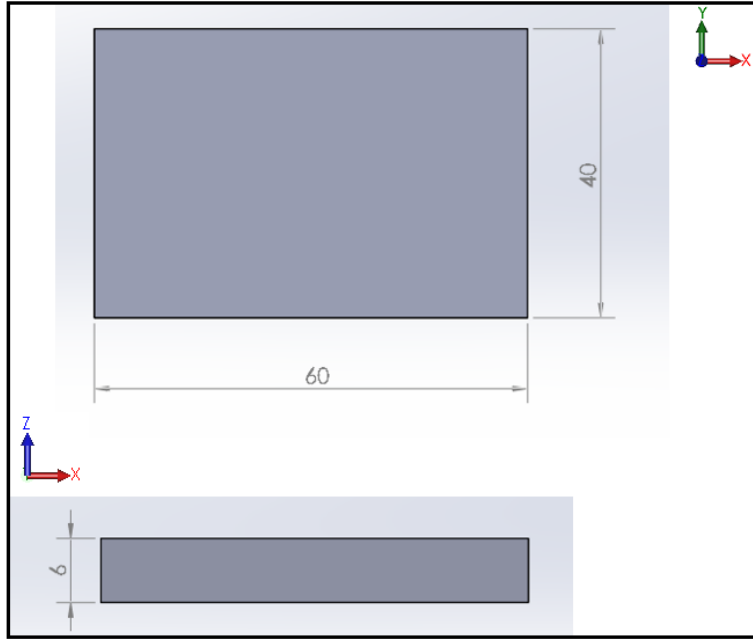


Figure 39: Build plate top and front view. Dimensions in mm.

7.2. Inherent strains application.

The principal components of the inherent strains vector to apply to each layer are provided by DTI:

$$\begin{cases} \varepsilon_{11}^* \\ \varepsilon_{22}^* \\ \varepsilon_{33}^* \end{cases} = \begin{cases} -0.00609878 \\ -0.00208316 \\ -0.2995 \end{cases} \quad (7.1)$$

whose values were calibrated experimentally comparing the distortions before and after the removal of the part from the build plate (Section 2.2). The “in-plane” strain state $(\varepsilon_{11}^*, \varepsilon_{22}^*)$ is modelled as isotropic to simplify the implementation. Thus, the applied in-plane strains are:

$$\varepsilon_{11}^* = \varepsilon_{22}^* = -0.00409097 \quad (7.2)$$

which corresponds to the average value of both components.

A sudden application of eigenstrains can lead to convergence difficulties due to an excessive distortion of the elements. Therefore, Abaqus/Standard gives the possibility to ramp up the eigenstrains linearly according to the formula:

$$\varepsilon^{inh} = \begin{cases} \frac{t-t_{act}}{\tau_{inh}} \varepsilon_0^{inh}, & t_{act} \leq t \leq t_{act} + \tau_{inh} \\ \varepsilon_0^{inh}, & t > t_{act} + \tau_{inh} \end{cases}, \quad (7.3)$$

where ε^{inh} is the inherent strain applied, ε_0^{inh} is the value of the inherent strain at the end of the increment at which the element gets activated, t_{act} is the activation time and τ_{inh} is the user-specified time constant [21]. The time constant must be smaller than the time required to activate one layer-element. Otherwise, the inherent strains are not fully applied before the layer above gets activated. That would make the shared nodes of the new layer have a wrong initial configuration which can lead to inaccurate results. Figure 40 shows the first component of the eigenstrains ε_{11}^* applied to the structure before and after the addition of a new layer using a time constant equal to 82 s. The delay caused by the ramped application may lead to a lack of inherent strains applied over the last element layer.

The isotropic inherent strains guarantee the same application regardless the scanning pattern or the interlayer rotation. A single scanning strategy is applied to the whole model.

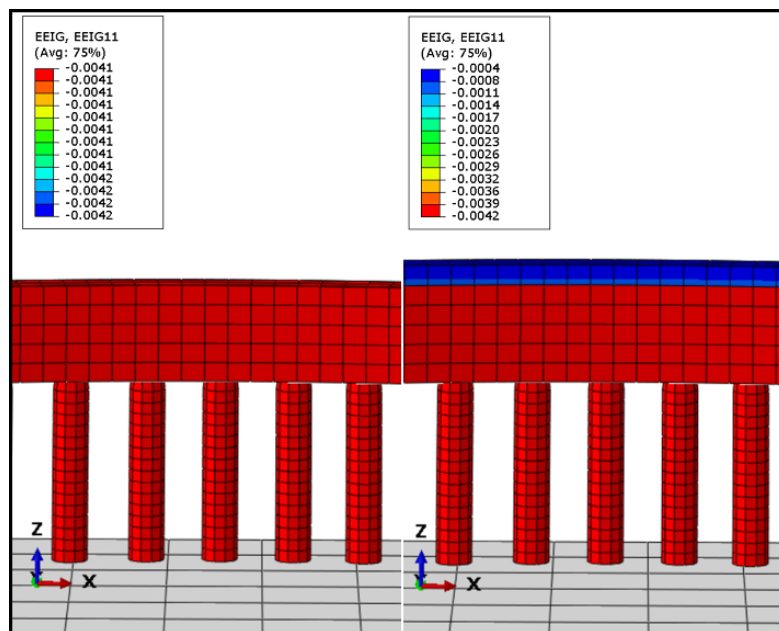


Figure 40: ε_{11}^* state before the addition of a new element layer (left) and after the addition of a new element layer (right).

7.3. Boundary conditions.

The boundary conditions play an important role in the correct modelling of the process.

A fixing constrain of the bottom surface of the build plate is applied in both LF and MF mechanical simulations. It simulates the attachment of the build plate to the printer structure. The three degrees of freedom belonging to the displacement are limited to zero avoiding distortion alien to the printing process.

In the thermal simulation of the MF model a preheating temperature is applied on the top surface of the build plate equivalent to $200\text{ }^{\circ}\text{C}$. This condition is removed once the printing time starts. In addition, a room temperature of $40\text{ }^{\circ}\text{C}$ is set to the remaining free surfaces of the part and build plate. It comes from the Argon atmosphere presented during the whole printing time.

7.4. Interactions.

In this section the contact interactions between the part and the supports as well between the supports and the build plate are modelled. A “tie” constrain is implemented, meaning that the nodes belonging to the two components unify their translational motion. A Surface to Surface contact is defined which enforces the contact between the slave node and the facets of the master surface. Figure 41 depicts the support surfaces in contact with the part and with the build plate. The slave surface is highlighted in a pink colour whereas the master surface in red. The slave surface is assigned to the supports because it is the smallest surface of both interactions and has a more refined mesh allowing to join more points.

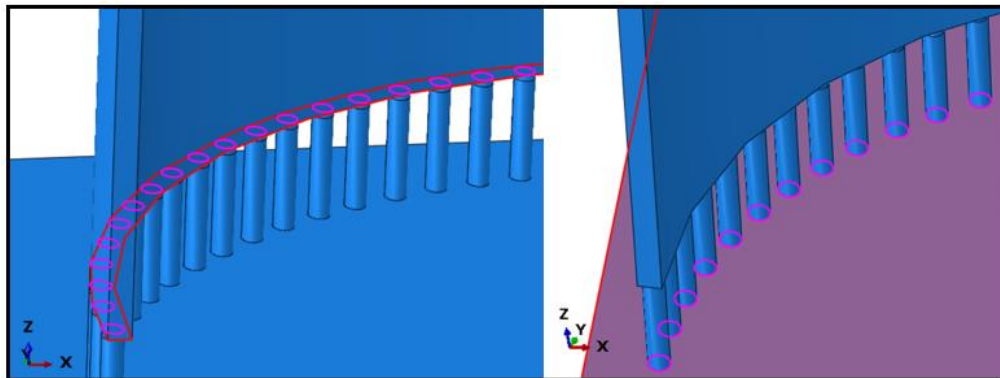


Figure 41: Part contact surface (left) and build plate contact surface (right) in pink.

7.5. Printing parameters.

There are different parameters that enable a customization of the printing process. For example, the type of element activation or the inactive element's behaviour (see Section 6.6.). The laser scanning details are also important to determine the time period of the simulation. This data was provided by DTI and is summarized in table 4. These parameters were introduced in the ReplicatorG toolpath generator and resulted in a printing time of *8693 s (2 hours 25 minutes)* which must coincide with the application of the last inherent strains. The scanning laser path is rotated 90° every layer to avoid the accumulative error caused by any path defect as happened in the HF model (See section 6.10.2.1). The toolpath of the first two layers is illustrated in figure 42.

The elements are partially activated to fit the cases when the slice height does not match the finite element height. The new material is added with the prescribed eigenstrains. When the new material is added in an increment, both the old and new material contribute to the stress response [25]. In general, the two slices are in different states. Therefore, the homogenized values of state variables are used to compute stresses from the relation:

$$\varepsilon^{el} = \Delta\varepsilon + \frac{V_t^f}{V^f} \varepsilon_t^{el} - \frac{\Delta V^f}{V^f} \Delta\varepsilon^* \quad (7.4)$$

where ε^{el} is the homogenized elastic strain; V^f is the volume fraction of the material in the element; V_t^f is the volume fraction of material in the element in the previous increment; ΔV^f is the volume fraction of the material added to the element; $\Delta\varepsilon$ is the total strain increment; $\Delta\varepsilon^*$ is the eigenstrain in the material added; and ε_t^{el} is the elastic strain at the end of the previous increment.

Finally, the "Follow deformations" option determines whether or not the inactivated elements are allowed to move and follow the predicted deformation of the part. In this situation, the inactive elements should follow the deformation to prevent excessive element distortion [21]. In this model, the large eigenstrains applied in z-direction forces the activation of this option.

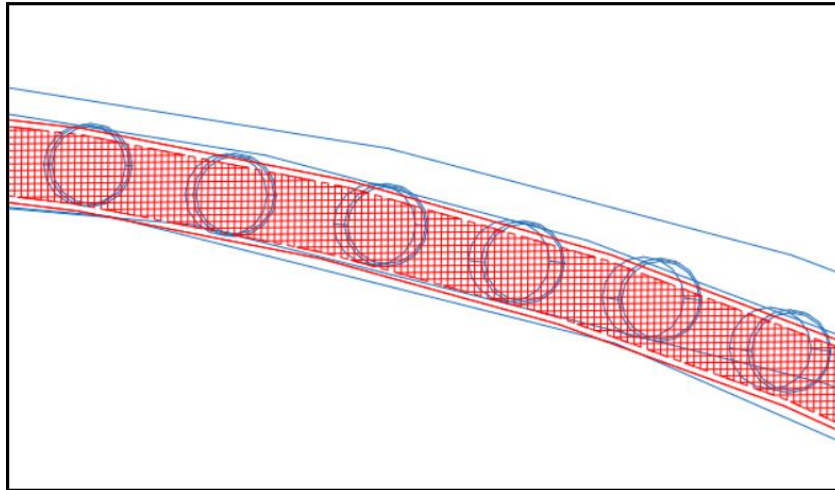


Figure 42: Scanning strategy of the Real model.

Printing parameter	Value
Layer height (μm)	60
Laser diameter (μm)	60
Laser speed (mm/s)	1100
Hatch distance (μm)	120

Table 4: Laser scanning parameters of the Real model.

7.6. Mesh.

The type of element used in the Real model is the same 3D 8-nodes linear brick element than in the Scaled model shown in figure 24.

The spatial distribution of the elements is uniform along the printed part, supports and build plate. This distribution allows an even application of the eigenstrains along the cross section. The proposed meshes are depicted in figure 43. The build plate presents a progressive refinement when getting closer to the support's location.

A mesh convergence study is done to obtain an efficient mesh size which is described in Appendix A.2.1. The study resulted in a mesh size of *7 physical layers per element* for the LF model and *2.33 physical layers per element* for the MF model to efficiently discretize the part

geometry. Consequently, the number of nodes of the part are 58210 and 1000482 for the LF and MF models, respectively.

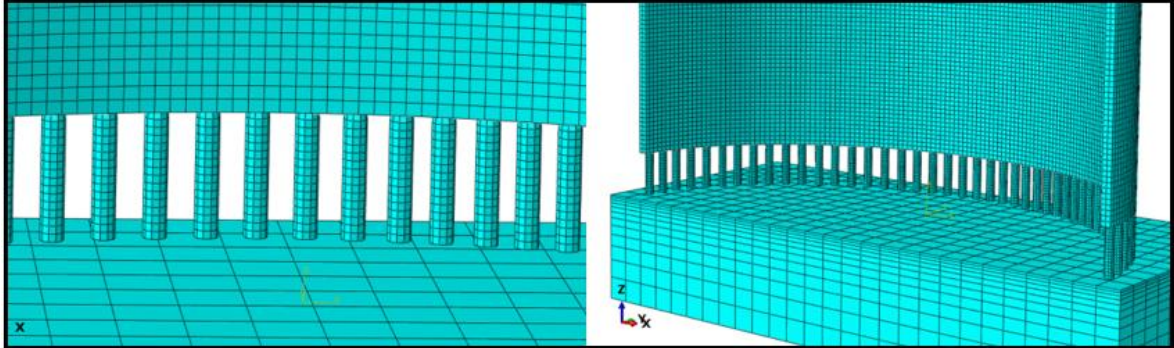


Figure 43: Mesh distribution for the supports and part (left) and the build plate (right).

7.7. Time-stepping

The static nature of the IS analysis does not require a time-stepping convergence study to find the efficient time increment. The same results are obtained regardless the time increment as long as the full application of the eigenstrains is guaranteed (See section 7.2). It is also preferable a time increment as big as possible in order to save computational time. A manual calibration is done to find an efficient time increment of 18 s for the printing process period of this model.

On the other hand, the transient MF model requires a time increment convergence study for both thermal and mechanical simulations to efficiently obtain accurate results. Appendix A.2.2 describes the aforementioned studies which result in a time discretization of 6 increments per element layer corresponding to 4.62 s.

7.8. Results.

7.8.1. After printing.

Once the proper space and time discretization are selected, the mechanical models are solved. The extrapolation scheme used to speed up the solution is turned off to prevent an excessive iteration typical from models with a plastic material definition [9].

In order to understand better the physical state of the part after the printing process, the magnitude of the distortion is split in its three components: U_x , U_y and U_z according to the global coordinate system. The supports and the build plate are suppressed in the visualization.

Figure 44 illustrates the distortions of the LF model. The *X-direction* component U_1 presents a symmetric distribution related to the *YZ-plane*. On the edges the magnitude rises from 0 mm at the bottom attached to the supports to the maximum value on the top corner's area. The top width of the part contracts 1.066 mm unevenly with a 13% difference between both sides. The distortions in the *Y-direction* have a total symmetric distribution related to the *YZ-plane*. The largest distortion takes place in the centre of the part, once the support's influence area is over. The part deforms to its inside with a maximum peak of 0.677 mm . Finally, the distortions in the *Z-direction* show a linear increment of the magnitude from the bottom to the top of the part. The part shrinks 1.166 mm from its original height.

The distortions of the MF model are depicted in figure 45. The *X-direction* component U_1 presents a symmetric distribution related to the *YZ-plane*. The largest distortions of 0.292 mm are located at the bottom of the part at a distance of 8 mm from the lateral edges. The expansion gradually decreases as the height increases with the edges starting to shrink from half of the part. The distortions in the *Y-direction* have an asymmetry in the *YZ-plane* with the largest distortions shifted to the left half. The part expands a maximum peak of 0.487 mm . The distortion is decreased as getting closer to the lateral edges. Finally, the distortions in the *Z-direction* show a small influence over the majority of the part but on the bottom corners where there is a local effect which is illustrated in figure 46.

The cross sections of both models are compared at the part's height of 20 mm in figure 47. A difference was observed in the *Y-direction* up to 0.628 mm at the centre of the section whereas 0.44 mm in the *X-direction* accumulated from both external edges. This derives from the opposite shrinking and expansion behaviour acknowledged in the LF and MF models, respectively.

The Von Mises stress distribution of the LF model is depicted in figure 48. The interlayer residual stresses are visibly widespread along the cross section of the outer face. The maximum stresses, which take place on the joining area with the supports, clearly overpass the yielding limit of 770 Mpa . This effect is caused by the value extrapolation from the Gauss points to the nodes of the elements. The stress concentrations must be realised with the removal of the supports.

Figure 49 illustrates the Von Mises stress field for the MF model. The maximum stress is limited to the one presented in the LF model in order to compare both fields. A uniform stress distribution is presented along the part. A slight stress concentration follows the edges of the outer face. The effect of the stress concentrations on the support's area is smaller than in the LF model. A point of the inner face experiences a 37 % drop in stress magnitude. On the other hand, the highest stresses are found on the supports up to 1867 MPa meaning a 140 % increment compared to the LF model.

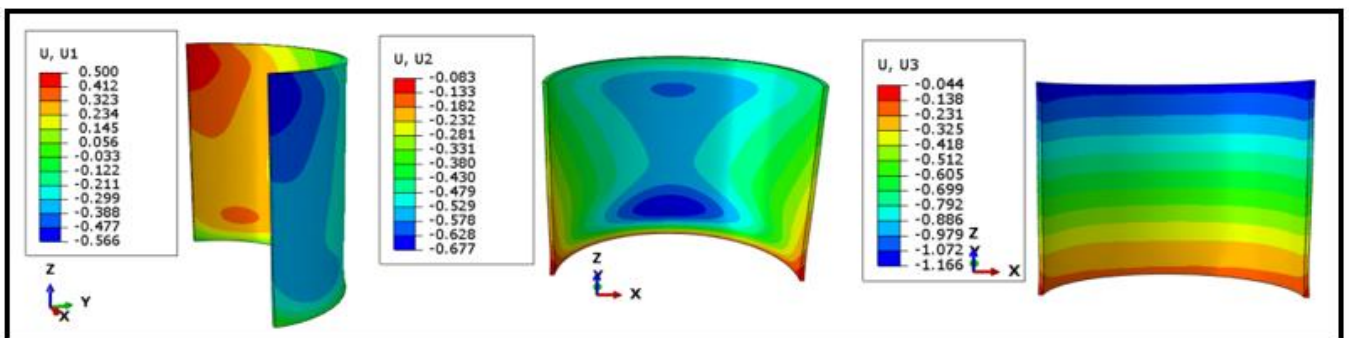


Figure 44: Distortions in X-direction U_1 (left), in Y-direction U_2 (centre) and in Z-direction U_3 (right) for the LF model. Units in mm.

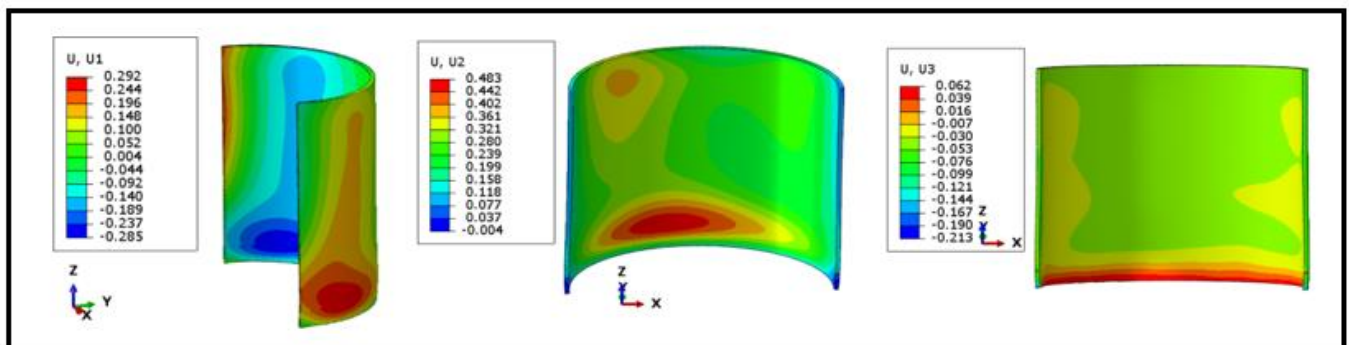


Figure 45: Distortions in X-direction U_1 (left), in Y-direction U_2 (centre) and in Z-direction U_3 (right) for the MF real model. Units in mm.

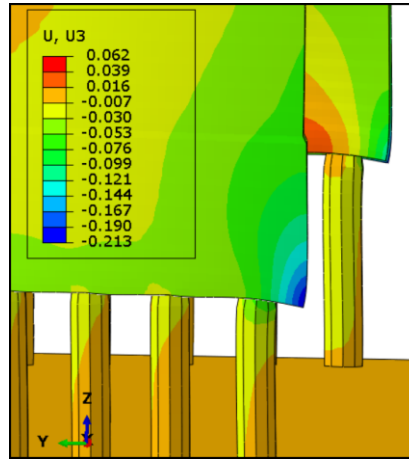


Figure 46: Detail of the distortions in Z-direction U3 for the MF model.

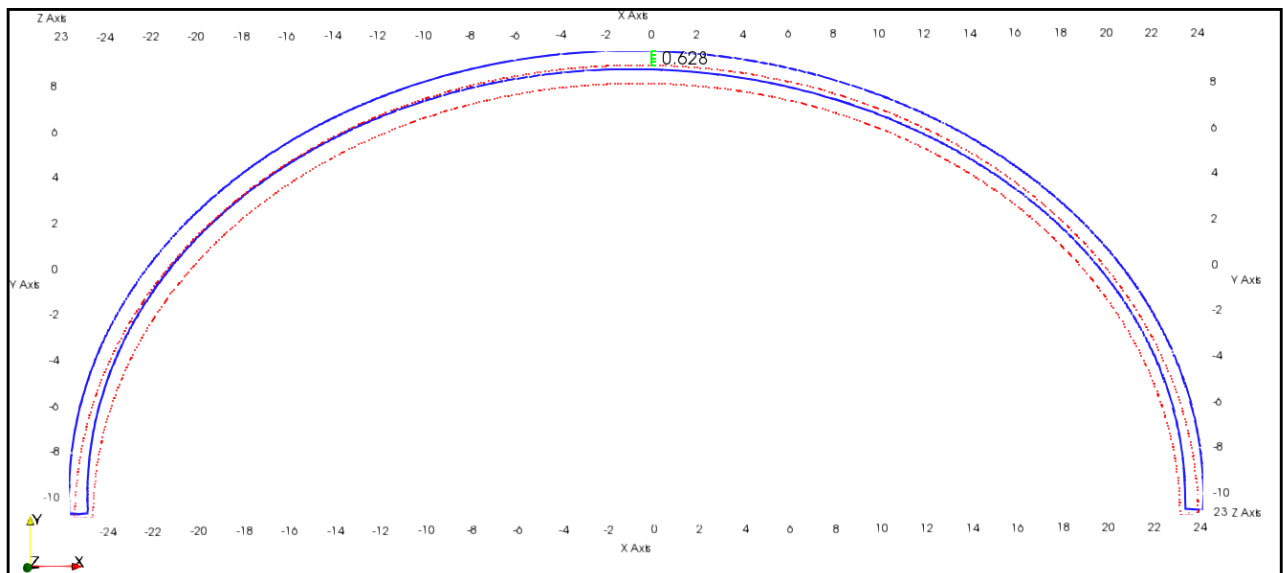


Figure 47: Cross-sections at $z=20$ mm of the LF model (red) and MF model (blue) after print. Measurements in mm.

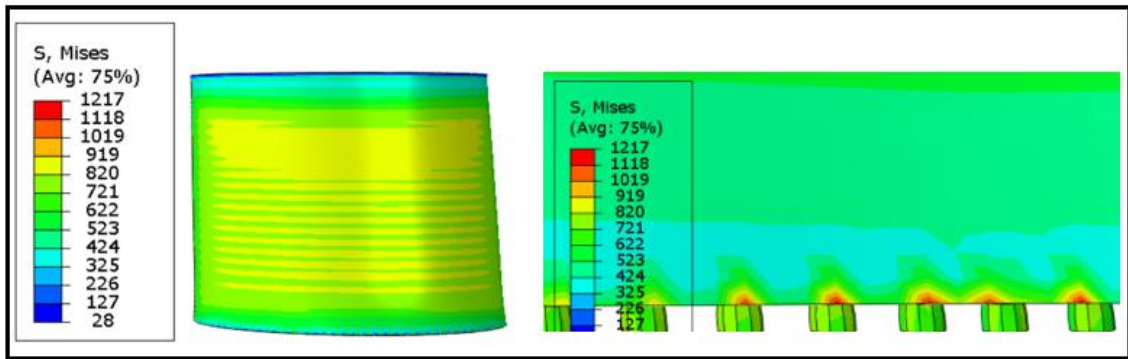


Figure 48: Stress distribution in MPa in the outer face (left) and a detail in the support's area (right) for the LF model.

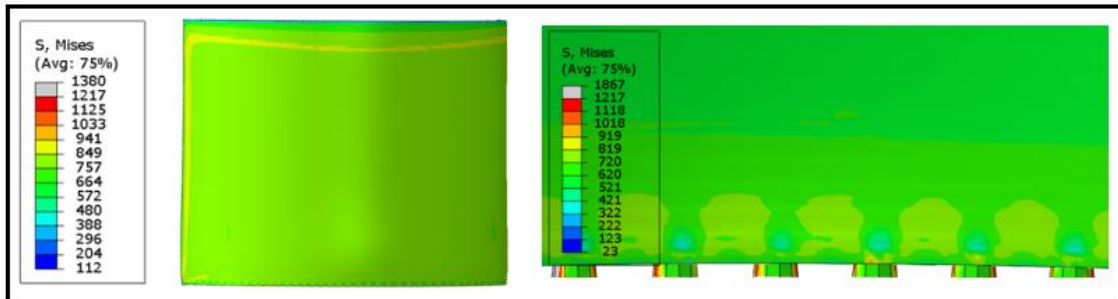


Figure 49: Stress distribution in MPa in the outer face (left) and a detail in the support's area (right) for the MF real model.

7.8.2. Supports removal.

Because of the bond between the printed part and the build plate, parts must be cut off after printing. This is done via sawing, milling or wire cutting. Once the part is released, the residual stresses redistribute, and the part deforms to its ultimate shape.

The cut is made along the support's element section highlighted in figure 50. It is modelled by removing the specified elements in a general analysis step. Just prior to the removal step, Abaqus/Standard stores the forces that the region to be removed is exerting on the remaining part of the model at the nodes on the boundary [26]. These forces are ramped down to zero during the removal step. Therefore, the effect of the removed region is completely absent only at the end of the step.

The part may fall off if a region of the model is left with an unconstrained rigid mode which can lead to convergence problems. In order to avoid it, six degrees of freedom are

constrained in different locations of the part highlighted in figure 51. The displacement in *X-direction* is constrained in a node on the middle of the bottom face. The part is constrained in *Y-direction* in a node of the top surface. Finally, two nodes of the supports attached to the part are constrained in *Z-direction*. The constrains do not add any internal stress to the elements.

Figure 52 illustrates the stress field in the supports' area before and after the cutting step of the LF model. It results in a reduction of 113 % in the stress concentrations close to the supports. This stress relief results in an additional deformation translated in an expansion in the *X-direction* and a shrinking in the *Y-direction* as can be observed in figure 53. There is not deformation in *Z-direction*. The bottom outer corners of both parts are made coincident for the visual comparison.

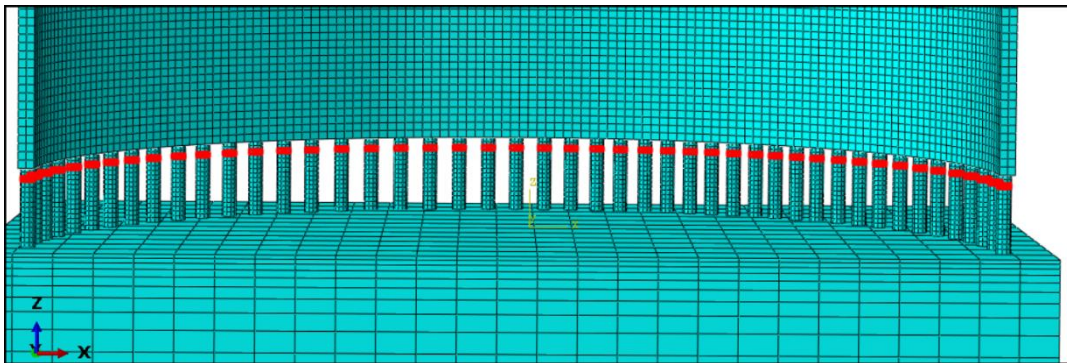


Figure 50: Section of the supports cut from the LF model.

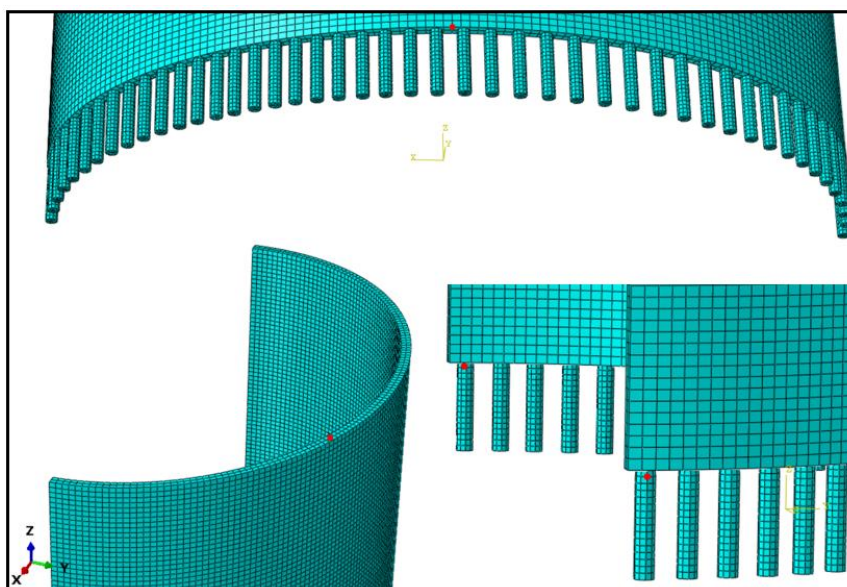


Figure 51: Locations constrained in *X-direction* (top), *Y-direction* (bottom left) and *Z-direction* (bottom right) for the cutting procedure.

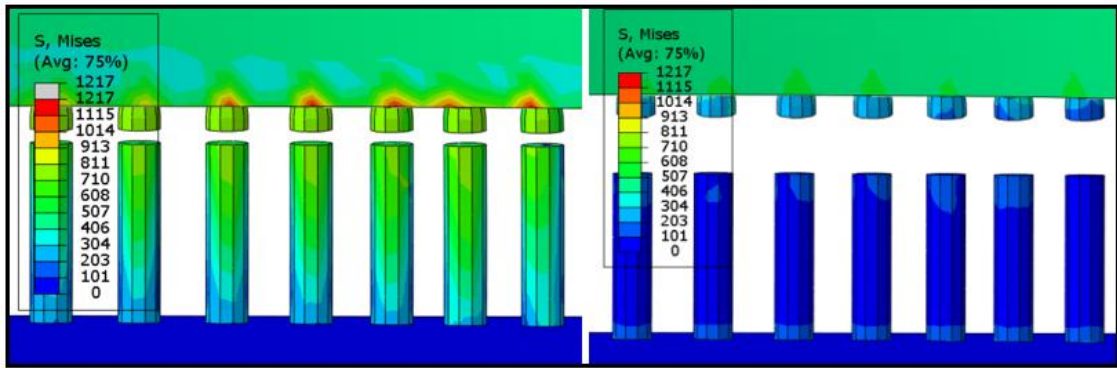


Figure 52: Stress distribution before cut (left) and after cut (right).

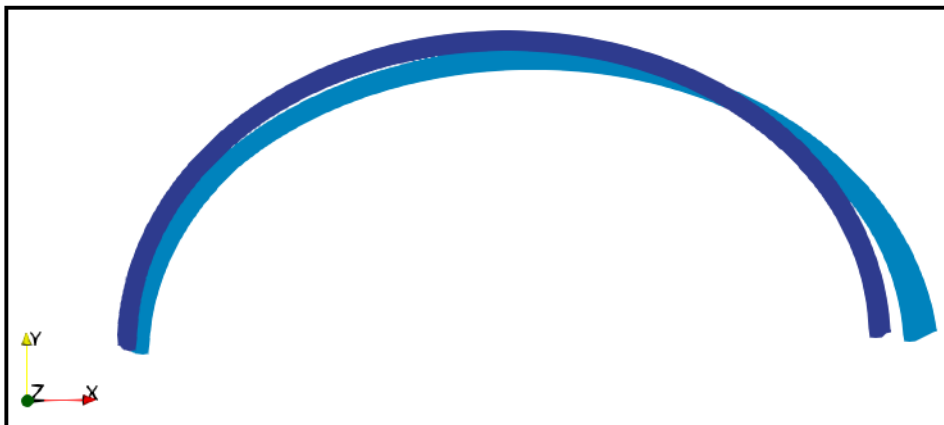


Figure 53: Comparison of cross-sections of the part before cutting (dark blue) and after cutting (light blue).

7.8.3. Heat treatment.

Heat treatment of the printed parts is a common practice in the metallurgical industry before removing the part from the platform. The objective is to decrease the residual stresses inherent to the printing process which helps to reduce the final distortions of the part.

Heat treatment techniques include annealing, tempering, carburizing or quenching among others. DTI applied an annealing treatment where the material is heated for several hours at a temperature of:

$$T \approx 0.5 T_m[K] \quad (7.5)$$

where T_m is the melting temperature, and then slowly cooled down to room temperature. Since the annealing temperature of $0.5 T_m$ lies in the region of recrystallization temperature, a complete relaxation of residual macro-stresses can be expected [27].

The thermal cycle applied to the platform in the experimental work is shown in figure 54. It is composed by three hours heating to $823 K$, three hours at a constant anneal temperature and three hours cooling in furnace to $373 K$.

The long-term exposure to high level of stress below the yield strength causes Creep deformations. Thus, it is important to implement a Creep Law which calculates the rate of deformation. The Steady-state creep model is implemented:

$$\dot{\epsilon} = A \sigma_A^n e^{(-Q/RT)} \quad (7.6)$$

where A is a constant related to the material microstructure, σ_A the applied equivalent stress, n the stress exponent for the dominant mechanism, Q the creep activation energy, R the universal gas constant and T the applied temperature. These constants are summarized in table 5. The value of A was extracted from an experimental work with similar annealing conditions applied to shot peened Ti-6Al-4V [27]. The exponent n comes from the dominance of the dislocation mechanism during creep in this alloy [28]. The value of Q represents the high-temperature creep activation energy for Titanium alloys [29]. The strain rate is updated at every time increment following an explicit scheme and it is used to compute the accumulative creep deformation.

A coupled thermo-mechanical simulation enables to get the temperature-stress history of the part plotted in figure 55. The evaluated point belongs to the concentration stress area close to the supports which can be visualized in figure 56. A smooth relaxation of the stress is noticed at the beginning. Then, when the material gets a temperature close to the 40 % of the melting temperature, the creep mechanism gets activated turning the elastic residual strains into plastic strains. This results in a final residual stress of 5 % of the original value at the end of the annealing process. Figure 57 shows the inverse relationship between the residual stress and the macro-plastic creep strain.

The large stress release is translated into smaller deformations after removal of the part from build plate. Figure 58 shows the comparison of bottom cross-sections of the LF model with and without annealing treatment. The distortions of the bottom face of the part is reduced a 70 % thanks to the heat treatment.

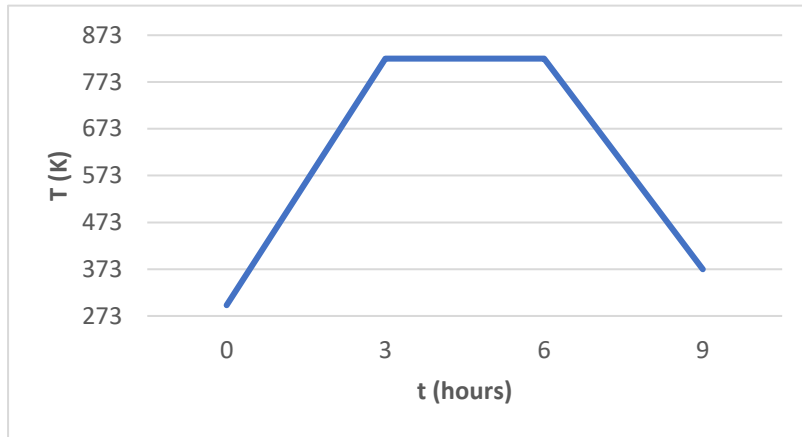


Figure 54: Annealing heat cycle.

Parameter	Value
A	5.88E-07
n	3
Q ($J \cdot mol^{-1}$)	100000
R ($J \cdot K^{-1} \cdot mol^{-1}$)	8.31446

Table 5: Creep law parameters.

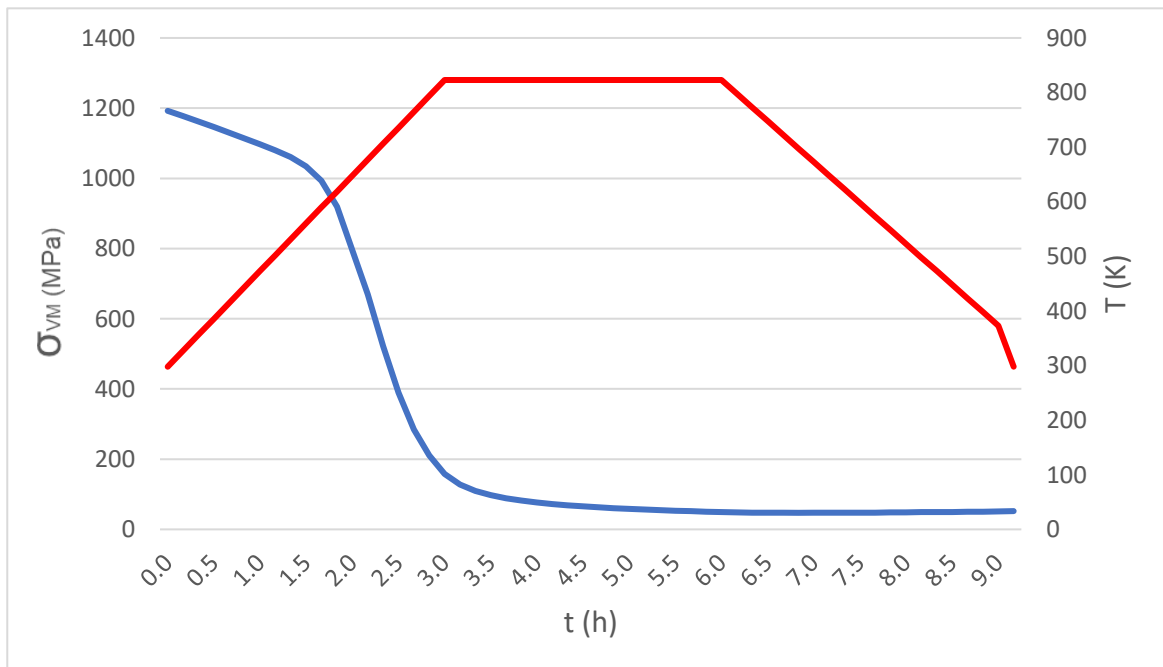


Figure 55: Stress-temperature annealing cycle on LF model. Stress (blue), temperature (red).

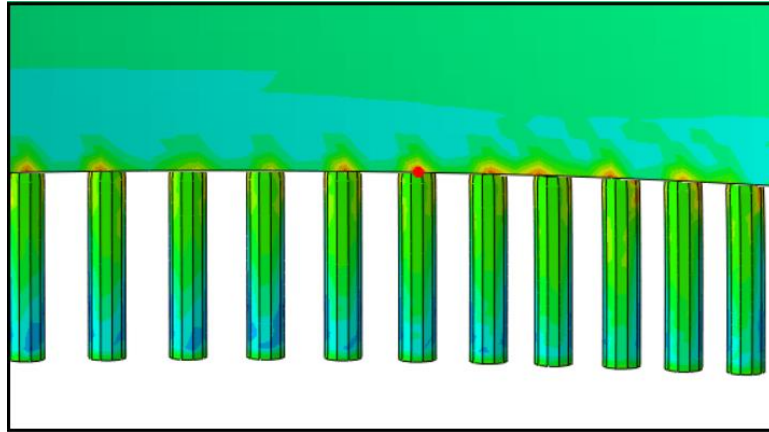


Figure 56: Point evaluated during the Annealing treatment (highlighted in red).

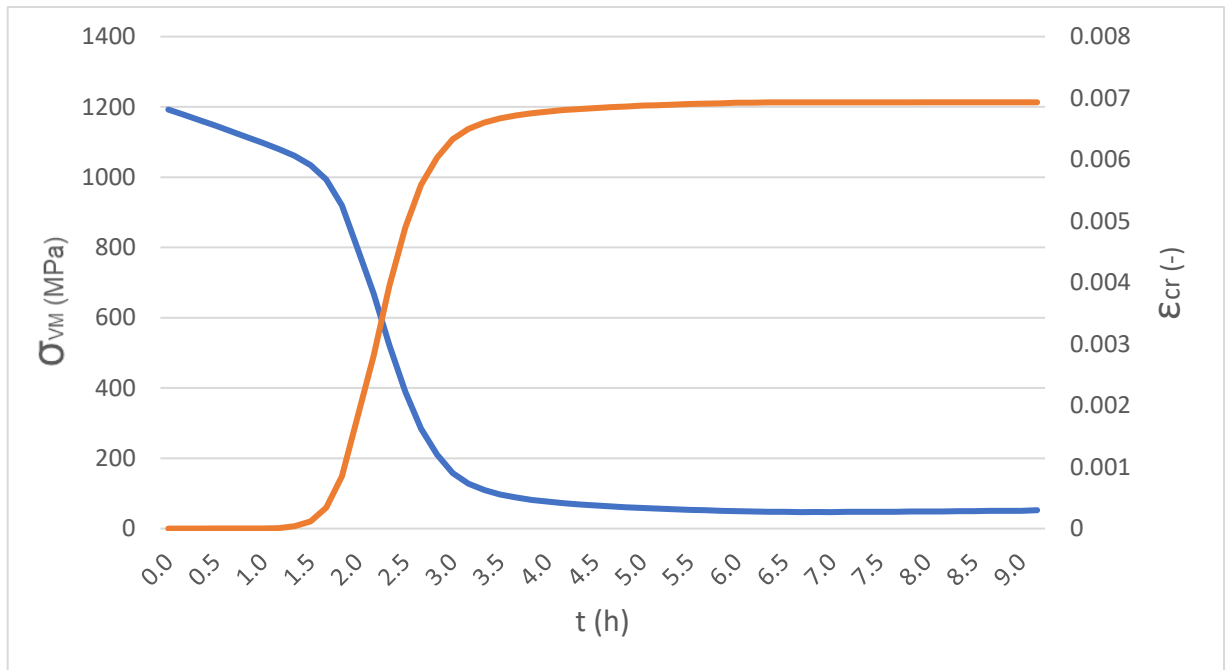


Figure 57: Stress – creep strain relationship during the annealing treatment. Stress (blue), strain (orange).

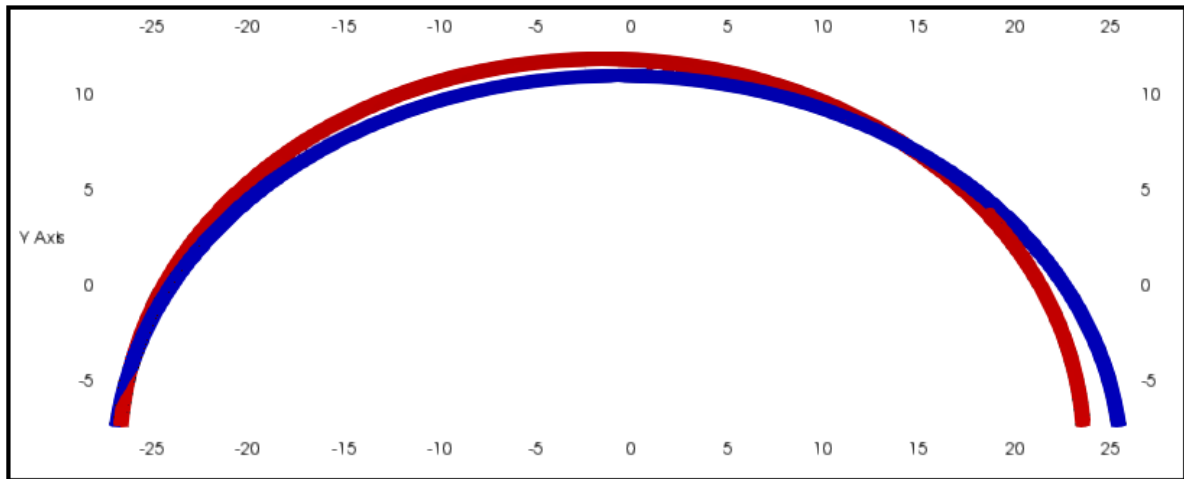


Figure 58: Bottom cross-sections of the LF model with annealing treatment (red) and without annealing treatment (blue).

7.9. Experimental data.

7.9.1. Available data.

The Oqton[®] Company provided the results of two nearly identical platforms with test parts printed at DTI. One of the platforms was heat treated before removal of the parts. At each platform were printed three identical instances of the part. All three parts were standing upright (front view position from figure 19). The orientation in the XY-plane was varied, but this variation is disregarded in the LF model. It is expected that the three prints from the same platform experience nearly identical deformations. The three parts are labelled part1, part2 and part3.

7.9.2. Measurement methodology.

The displacements were measured by optical scanning of the parts. The scanning was performed on the final parts, after removing them from the build plate.

The Oqton's Inspection cell of the figure 59 was used to scan the geometries of the printed parts. It provides a complete automatic 3D analysis of the part with an accuracy of 30 μm [30]. The part is placed on a small turntable and a sequence of scans is performed with 5-10 degrees rotation in between until the part is covered from all angles. These scans are stitched together. The high degree of symmetry of the part allows to the stitching algorithm to have

limited reference points. For this reason, a clamp was added on an edge of the part which must be removed before evaluation of the part. Figure 60 shows the point clouds before and after the manual removal of the clamp points using the data analysis application ParaView®. The parts appear solid because of the high density of measured points.

The dimensions of the top and bottom faces are measured in order to evaluate the simulated models. The way to extract the width, depth and height of the part (illustrated in figure 61) is described in Appendix A.3.



Figure 59: Inspection machine developed by Oqton® to scan the experimental parts [30].

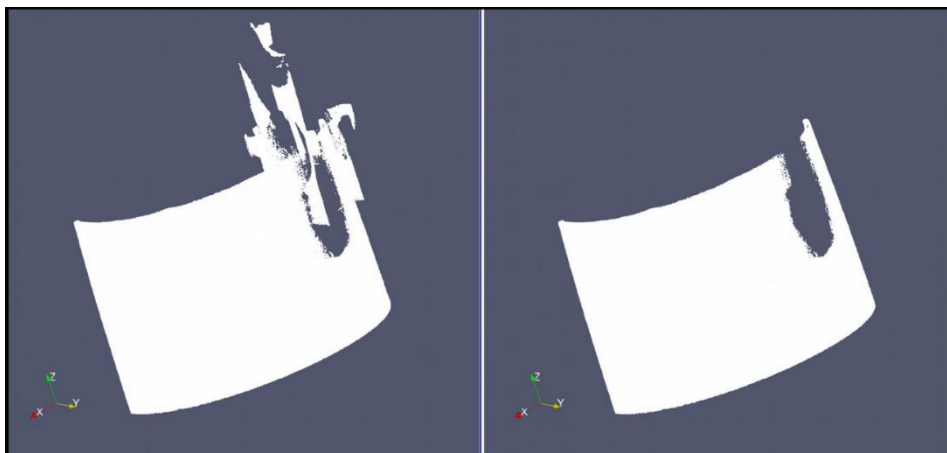


Figure 60: Scanned part before removal of the clamp (left) and after removal of the clamp (right).

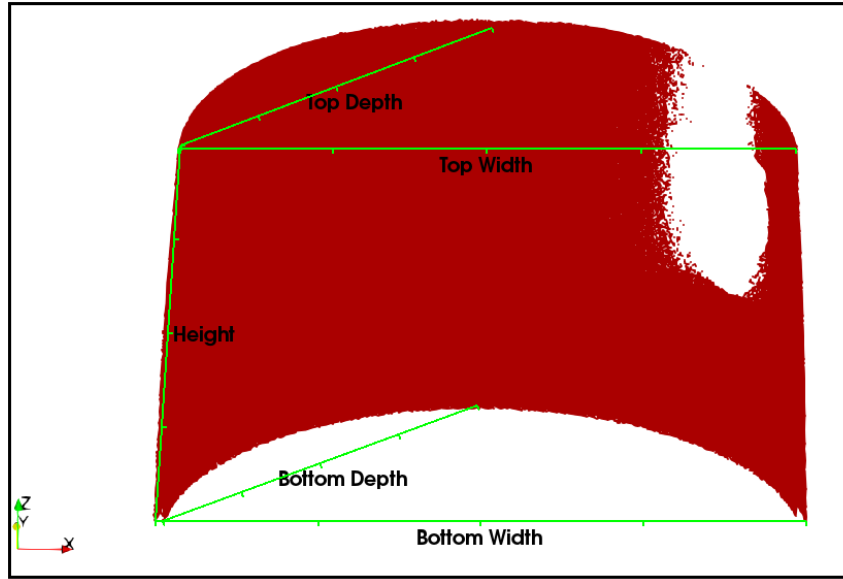


Figure 61: Measurements in the experimental parts.

7.9.3. Results.

The dimensions of the three parts belonging to the Heat Treated (HT) and Non-Heat Treated platforms are shown in table 6. The printed parts after the removal from the build plate expanded in width and shrunk in depth and height. The annealing treatment led to fewer distortions and had a larger effect on the bottom surface of the parts. Figure 62 shows the contour shape of the Non-HT part1 compared with the original part geometry.

Dimension (mm)	Original Part	Non-HT Part	Δl (mm)	HT Part	Δl (mm)
Width B.	50.0	53.60 ± 0.16	3.60 ± 0.16	50.93 ± 0.23	0.93 ± 0.23
Width T.	50.0	51.02 ± 0.14	1.02 ± 0.14	50.88 ± 0.24	0.88 ± 0.24
Depth B.	19.2	18.03 ± 0.14	-1.17 ± 0.14	18.59 ± 0.26	-0.61 ± 0.26
Depth T.	19.2	18.45 ± 0.18	-0.75 ± 0.18	18.74 ± 0.17	-0.46 ± 0.17
Height	40.0	37.39 ± 0.07	-2.61 ± 0.07	37.52 ± 0.07	-2.48 ± 0.04

Table 6: Measurements of the experimental parts after cut for the HT and Non-HT parts.

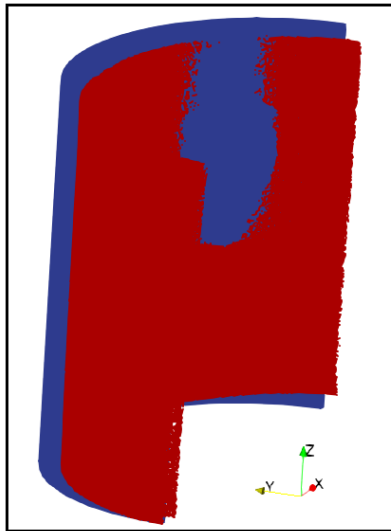


Figure 62: Contour shape comparison between the original part (blue) and experimental Part1 (red) for the Non-HT case.

7.10. Results comparison.

The deformed shape of the simulated models is compared with the actual printed parts in order to evaluate the accuracy of the models. All the deformed shapes are measured after the part removal from the build plate.

7.10.1. Non-heat treated part.

Table 7 compares the length change of the dimensions between the LF, MF models and the experimental part for the Non-HT case. The compared dimensions can be visualized in figure 61. In AM a $\pm 30\%$ of the measured value is a fairly acceptable range to deem the results of a simulation as accurate [7].

Δl (mm)	Non-HT Part	LF model	% difference	MF model	% difference
Width B.	3.60 ± 0.16	3.13	13	-3.03	184
Width T.	1.02 ± 0.14	0.50	51	-1.54	251
Depth B.	-1.17 ± 0.14	-1.14	3	0.91	178
Depth T.	-0.75 ± 0.18	-0.62	17	0.53	171
Height	-2.61 ± 0.07	-1.23	53	0.02	101

Table 7: Experimental - simulated models comparison for the Non-HT case.

7.10.1.1. Low Fidelity model.

Table 7 shows that the experimental widths are larger than the ones in the LF model with a larger difference in the top surface. It is probably caused by the lack of inherent strains applied over the last element layer shown in figure 63. This effect results from the need for ramping up the application of inherent strains to avoid convergence issues (see Section 7.2.). The aforementioned issue also makes the bottom depth to fit better the experimental data than the top depth. Finally, the printed part experiences a larger shrinking in *Z-direction* than the LF model caused by the isotropic plasticity assumption. The metal in a powder state typically presents an orthotropic behaviour with a stress ratio $R_{33} < 1$ that leads to higher deformation in *Z-direction*.

The differences listed in table 7 can be observed in figure 64. The LF deformed shape is overlapped over the experimental part. The bottom left corners of the parts are made coincident. There is an expansion effect in *Y-direction* on the areas close to the bottom of the LF part which does not experiences the experimental part. This may be caused by the FEM overestimation of the residual stress when extrapolating from the Gauss points to the nodes.

Besides the top and bottom of the parts, a middle cross-section at a height $z = 12 \text{ mm}$ is extracted and the outer face contours are compared in figure 65. All the measurements are in *mm*. It is observed a correlation in depth ($x = 0$) and a progressive difference leading to a maximum of 0.95 mm at the right edge ($x = 25 \text{ mm}$).

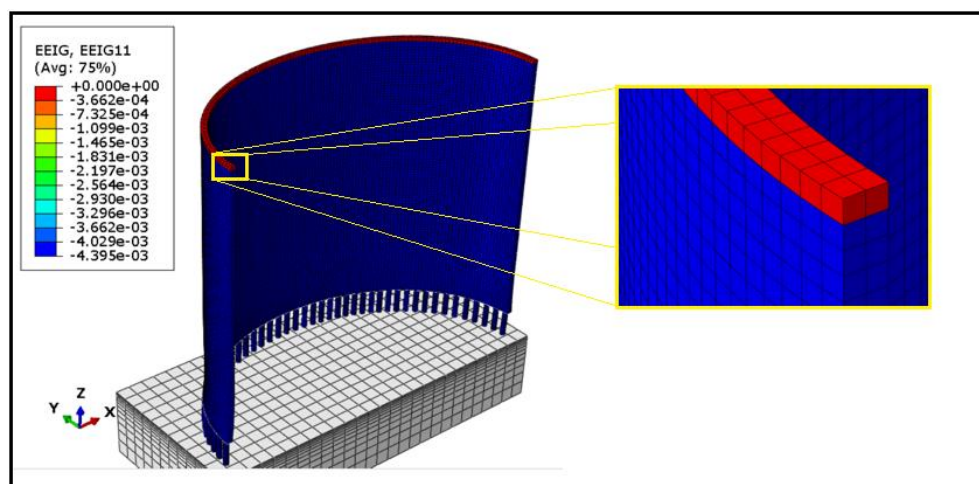


Figure 63: Error in the application of the Inherent strains on the last element layer.

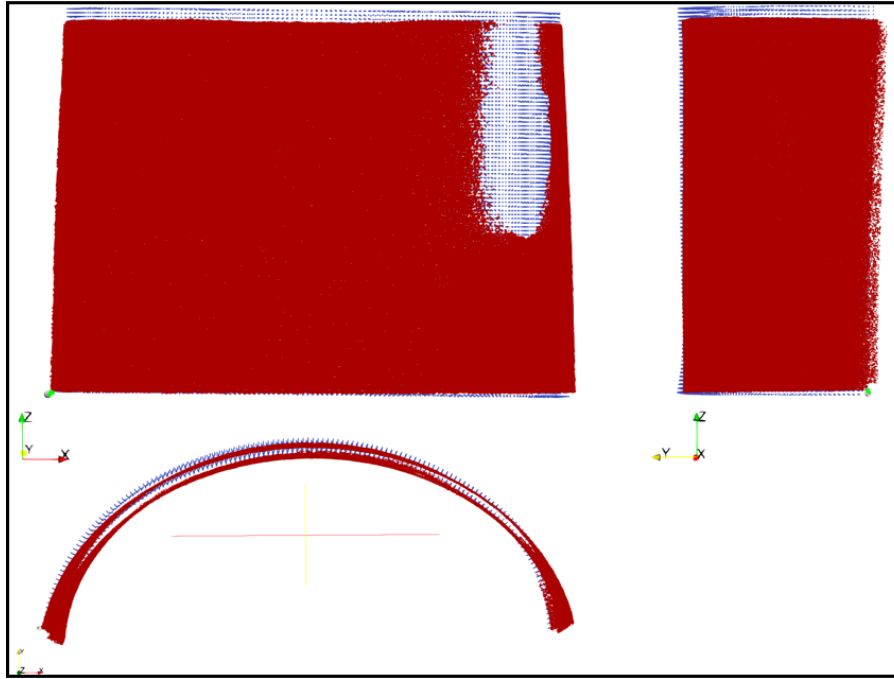


Figure 64: Deformed shape of the Part1 (red) and the LF part (blue) for the Non-HT case.

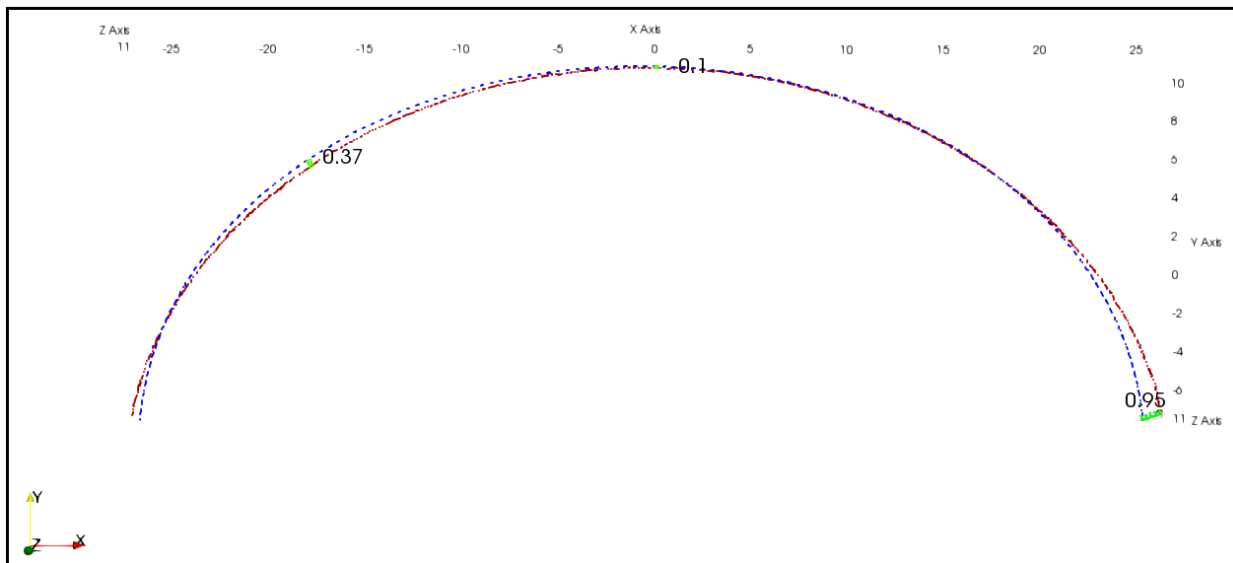


Figure 65: Cross-section's external contour at $z=12$ mm of the experimental part (red) and LF model (blue) for the Non-HT case. Measurements in mm.

7.10.1.2. Medium Fidelity model.

The measurements of the MF part after cutting the supports are shown in table 7. The large differences related to the experimental print are caused by an opposite behaviour when realising the residual stresses. The MF part shrinks in width and expands in depth whereas the experimental part experiences the opposite. The MF behaviour originates from the stress concentrations on the outer bottom edge of the part illustrated in figure 66. These stresses are redistributed after cutting and originate the “closing” effect that can be visualized in figure 67. The stress concentrations have their origin on the deformation of the printed supports shown in figure 68. The top surface of the supports deforms in the direction of the outer face of the part. The reason is probably a displacement in the initial position assigned to the supports.

In addition, the thermal simulation involves the following uncertainties that influence in the distortions of the part:

- Laser scanning path: the layer-to-layer rotation angle and infill scanning strategy may differ from the actual printing.
- Solid-state phase transformation: Different temperatures determines which solid phase exist. When the solid state changes phase, the shift to a different crystallographic orientation can produce phase transformation strains [7]. Modelling this would have modified the distribution of residual stresses shown in figure 66.
- Printing parameters: the absorption from the laser, film coefficient of the convection and emissivity of the material are extracted from previous studies and may differ from the actual printing conditions.

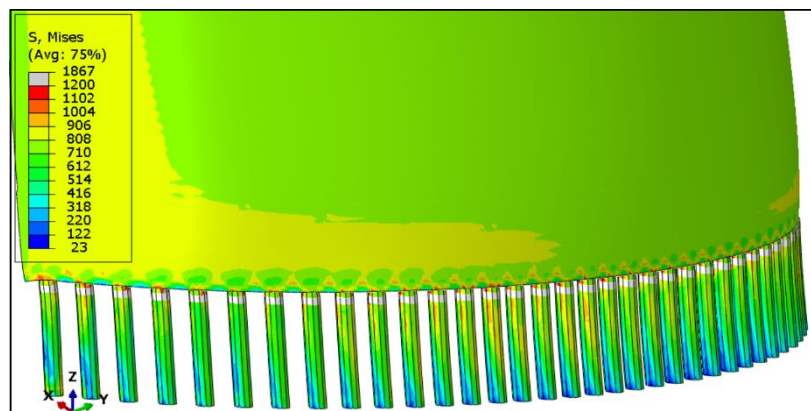


Figure 66: Residual stress presented in MF model after printing. Von Mises stress in MPa.

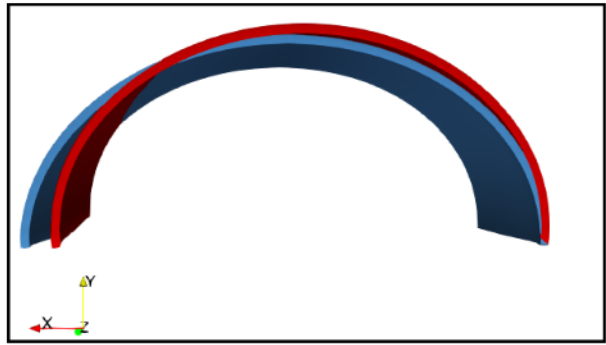


Figure 67: Closing effect. Deformed shape after printing (blue) and after stresses release (red) for the MF model.

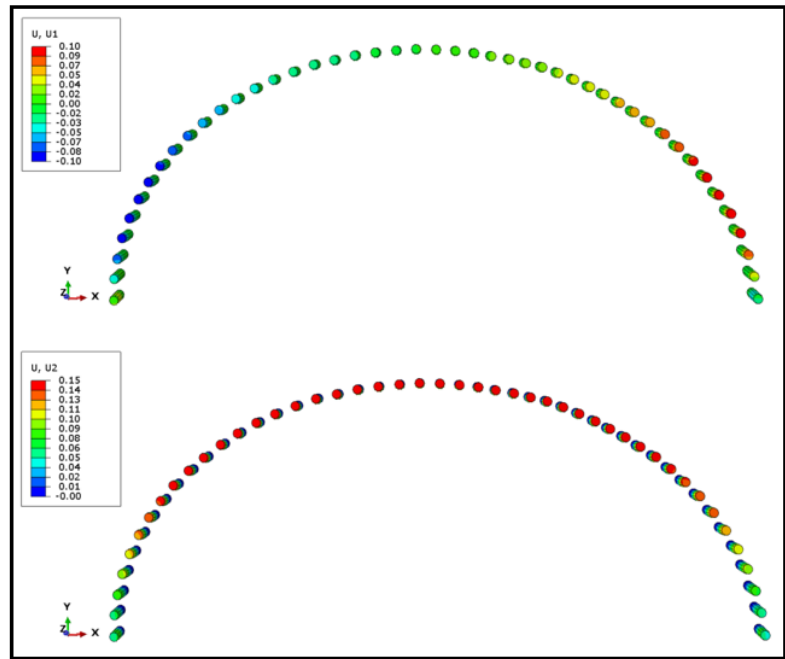


Figure 68: Support's top surface deformation after printing for the MF model. Displacements in mm.

7.10.2.Heat treated part.

Table 8 compares the length change between the LF model and the experimental part for the HT case. The experimental and simulated bottom widths experience a shrinking of 2.46 and 2.13 mm, respectively, after the annealing treatment. The top width accumulated the error inherent to the printing process and was influenced by the following modelling uncertainties that also affected to the depth of the part:

- The Steady State creep law relates only to the Secondary creep regime but neither to the primary nor the tertiary. In practice, the primary regime can be extended over a significant fraction of the creep lifetime and its contribution to the overall creep strain can be substantial [28].
- The material constant A belonging to the Steady State creep Law was extracted from a peened-shot Ti-6Al-4V component. A correction can be expected for an additive manufactured component.
- The FEM heat treated simulation does not consider the micro-stresses which ultimately lead to a higher distortion in the printed part.

Together with the aforementioned uncertainties, the measurements taken in sensible locations (corners of the part) contribute to the differences in the results.

Δl (mm)	HT Part	LF model	% difference
Width B.	0.93 ± 0.23	1.00	8
Width T.	0.88 ± 0.24	0.28	68
Depth B.	-0.61 ± 0.26	-0.34	45
Depth T.	-0.46 ± 0.17	-0.52	12
Height	-2.48 ± 0.04	-1.03	58

Table 8: Experimental - LF model comparison for the HT case.

7.11. Computational cost.

The MF model involves high computational costs in industrial part sizes. The thermal model took *16 hours* of running time whereas the mechanical model needed *114 hours* to be completed, making a total simulation time of *5 days and 10 hours*. In addition, the output data required a total of *21 GB*.

On the other hand, the LF model needed only *1 hour* to be completed and the memory requested *6 GB*. The removal of the supports took *4 minutes* whereas the annealing process required *20 minutes*.

The running time is measured from the instant the job is submitted to the end of the process solution. The simulations run in parallel using a total number of 24 CPUs from the CLUSTER provided by DTU (Technical University of Denmark) which contains different hardware components [24].

8. Conclusions.

After modelling, implementing, and analysing the results of the simulation methods, applied to the SLM manufacturing process, one can conclude that:

Related to the simulation methods:

- A detailed-level thermo-mechanical simulation captures the defects presented in the laser scanning path.
- A process-level thermo-mechanical simulation qualitatively and efficiently predicts the distortions after printing of a detailed-level simulation.
- An Inherent strains simulation predicts accurately the distortions of the part except for the top of it. The implemented procedure does not allow to apply inherent strains over the last layer.
- A process-level thermo-mechanical simulation does not predict the actual distortions of the printed part.
- The number of uncertainties is reduced in the Inherent strains simulation compared to the thermo-mechanical simulation.

Related to the computational cost:

- A detailed-level thermo-mechanical simulation is unfeasible to model part sizes typically printed in the AM metal industry.
- A process-level thermomechanical simulation requires a high computational time to model part sizes typically printed in the AM metal industry.
- An Inherent strains simulation is computationally efficient applied to part sizes typically printed in the AM metal industry.
- The use of a computer cluster is highly recommended to manage the computational requirements of thermo-mechanical simulations in AM.

Related to the software:

- Abaqus/Standard offers the frame to implement the whole metal printing process: building, heat treatment and cutting.
- The use of Abaqus/Standard for the simulation of AM requires a deep understanding of the process, internal code and user subroutines of the software.

- The functionality of Abaqus/Standard provides a high degree of control and customization.
- Abaqus/Standard has limitations in the implementation of the simulation methods.

Related to the experimental data:

- The experimental print is required. An incomplete experimental data including material properties, printing conditions and actual laser scanning strategy does not allow to obtain accurate results.
- An accurate calibration of the experimental eigenstrains is fundamental for the implementation of the Inherent strains simulation method.

Related to the FEM modelling:

- A mapped mesh is required to accurately simulate the layer deposition and the inherent strains application.
- A process-level finite element mesh introduces error in the prediction of the residual stresses due to the stress extrapolation from the Gauss points to the nodes.
- A small change in the initial distribution of the supports has a relevant influence on the final distortions of the part. Supports close to the edge of the part cause stress concentrations that modify the residual stresses field.
- The isotropization of the in-plane components of the inherent strains successfully approximates the influence of the actual scanning strategy.
- The larger the magnitude of the applied inherent strains, the higher the computational time required.

9. Assessment of the work done.

9.1. Objectives achieved.

The objective of creating a low fidelity model which approximates the final state of the printed part at a substantially lower computational expense is accomplished. The low fidelity model developed by the Inherent strains method predicted the distortions of the experimental part requiring a small portion of the time needed in the thermomechanical simulation.

9.2. Limitations and Future work.

The modelling of the printing process resulted in a challenging task because of the incomplete experimental data. The lack of the actual scanning strategy, several printing parameters and material properties made increase the number of assumptions based on previous works.

The experimental print of the parts would be carried out in a future work. Joining the process simulation and the experimental work would allow to reduce the number of uncertainties and would give a more reliable view of the accuracy of the models. An alternative FEM software would be also used to overcome the incapability of Abaqus/Standard to apply the inherent strains over the last element layer of the part. In addition, the following deeper studies would be carried out to improve the outcome of the models:

- Implementation of an orthotropic plasticity model with a stress ratio in the building direction below one. This assumption could improve the simulated behaviour of the distortions in the building direction.
- Implementation of a Miller – Norton creep law that captures the effect of both the Primary and Secondary Regimes. This would approximate better the stress release of the part during the heat treatment and, thus, the final distortions of the simulated model.
- Calibration of the initial position of the supports in the MF model. It would clarify whether the source of error comes from the supports or from the uncertainties related to the thermal model.

References

- [1] Redwood B, Schöffner F, Garret B. The 3D printing book. 3D HUBS. 2017.
- [2] Additive Manufacturing Research Group Loughborough University, Powder bed fusion, Loughborough University, viewed 16 April 2020, <<https://www.lboro.ac.uk/research/amrg/about/the7categoriesofadditivemanufacturing/powderbedfusion/>>
- [3] Panorender, Advantages of metal 3D printing for medical parts, Panorender, viewed 16 April 2020, < <https://panorender.com/advantages-of-metal-3d-printing-for-medical-implants/>>
- [4] Shiomi M, Osakada K, Nakamura K, Yamashita T, Abe F. Residual stress within metallic model made by selective laser melting process. CIRP Ann-Manuf Technol 2004;53(1):195–8.
- [5] Dassault Systèmes. Abaqus documentation. Analysis techniques. Additive Manufacturing Process Simulation. Special purpose techniques for additive manufacturing. 2019.
- [6] Costa L, Vilar R, Reti T, Deus AM. Rapid tooling by laser powder deposition: process simulation using finite element analysis. Acta Mater 2005;53(14):3987–99.
- [7] Gouge M, Michaleris P. Thermo-mechanical Modeling of Additive Manufacturing . Butterworth-Heinemann; 2018
- [8] Dassault Systèmes. Abaqus documentation. Analysis techniques. Additive Manufacturing Process Simulation. Toolpath – mesh intersection module. 2019.
- [9] Dassault Systèmes. Abaqus documentation. Analysis techniques. Additive Manufacturing Process Simulation. Thermomechanical simulation of additive manufacturing process. 2019.
- [10] Keller N. Verzugsminderung bei selektiven Laserschmelzverfahren durch Multi-Skalen-Simulation; 2017.
- [11] Dassault Systèmes. Abaqus documentation. Analysis techniques. Additive Manufacturing Process Simulation. Toolpath-mesh intersection module. 2019.
- [12] Stoer J, Bulirsch R. Introduction to numerical analysis, vol. 12. Springer Science & Business Media; 2013.
- [13] Dassault Systèmes. Abaqus documentation. Analysis procedures. Heat transfer and thermal-stress analysis. Uncoupled heat transfer analysis. 2019.
- [14] Dunbar AJ, Denlinger ER, Gouge MF, Michaleris P. Experimental validation of finite element modeling for laser powder bed fusion deformation. Additive Manuf 2016;12:108–20.
- [15] Dassault Systèmes. Abaqus documentation. Theory. Mechanical Constitutive Theories. About mechanical constitutive models. 2019.
- [16] Ninshu Ma, Keiji Nakacho, Takahiko Ohta, Naoki Ogawa, Akira Maekawa, Hui Huang, and Hidekazu Murakawa. Inherent strain method for residual stress measurement and welding distortion prediction. In ASME 2016 35th International Conference on Ocean and Arctic Engineering, pages V009T13A001–V009T13A001. American Society of Mechanical Engineers, 2016.

- [17] Setien I, Chiumenti M, van der Veen S, San Sebastian M, Garciandia F, Echeverria A. Empirical methodology to determine inherent strains in additive manufacturing. 2018.
- [18] Mertens R, Vrancken B, Holmstock N. Influence of powder bed preheating on microstructure and mechanical properties of H13 tool steel SLM parts. 2016.
- [19] Feih S, Sun C, Zhang B, Lo Q, Chin C, Wei J. Influence of Surrounding Powder Bed and Build Platform on Thermal Cooling Characteristics in 3D Printed Parts via Selective Laser Melting. 2017.
- [20] Dassault Systèmes. Abaqus documentation. Analysis Procedures and Techniques. Additive Manufacturing Process Simulation. Heat energy balance. 2019.
- [21] Dassault Systèmes. Abaqus documentation. Analysis Techniques. Special Purposes Techniques. Progressive element activation. 2019.
- [22] Dassault Systèmes. Abaqus documentation. Example Problems. Additive Manufacturing Process Simulation. Sequential thermomechanical analysis of a laser powder bed fusion build. 2019.
- [23] Doubenskaia M, Pavlov M, Grigoriev S, Smurov I. Definition of brightness temperature and restoration of true temperature in laser cladding using infrared camera. 2012.
- [24] DCC Computing Center DTU, Central DTU HPC Cluster (LSF 10), Danmarks Tekniske Universitet, viewed 10 June 2020, <https://www.hpc.dtu.dk/?page_id=2520>
- [25] Dassault Systèmes. Abaqus documentation. Analysis Techniques. Eigenstrain-based simulation of additive manufacturing processes. 2019.
- [26] Dassault Systèmes. Abaqus documentation. Analysis Techniques. Special Purposes Techniques. Element and contact pair removal and activation. 2019.
- [27] Vöhringer O. Relaxation of residual stresses by annealing or mechanical treatment. 1987.
- [28] Kral P, Dvorak J, Blum W, Kudryavtsev E. Creep study of mechanism involved in low-temperature superplasticity of UFG Ti-6Al-4V processed by SPD. 2016.
- [29] Department of Materials Science and Metallurgy at the University of Cambridge, Constitutive Laws for Creep. University of Cambridge, viewed 27 June 2020, <<https://www.doitpoms.ac.uk/tlplib/creep/constitutive.php>>
- [30] Oqton 2019, Oqton announces the first fully automated 3D inspection machine, Oqton, viewed 30 June 2020, <<https://www.oqton.com/oqton-announces-the-first-fully-automated-3d-inspection-machine/>>
- [31] Danish Technological Institute, Organisation, DTI, viewed 22 May 2020, <<https://www.dti.dk/about>>

A. Appendix.

A.1. Collaborating organizations.

The Oqton company is a multinational organization that implements an artificial intelligence driven factory operating system to solve today's additive manufacturing challenges. Their product, FactoryOS™, is an end-to-end production platform that tightly connects manufacturing software and hardware. As a result, the productivity is boosted by complete production visibility and automated engineering workflows [30]. In the Copenhagen division an in-house simulation software is developed to optimize the SLM manufacturing process focusing on the dental market.

The Danish Technological Institute (DTI) is a leading research and technology Institute with more than 1000 specialists. It is a multi-disciplinary Institute divided in 7 divisions: Production & Innovation, Materials, Environmental Technology, Energy & Climate, Agro technology, Building & Construction and Meat research [31].

A.2. Convergence studies.

A.2.1. Mesh convergence.

HF MODEL

The study evaluates the nodal temperature. The mesh size is related to the physical layer thickness. For the HF model a range of sizes from 2 to 0.33 physical layers per element is analysed. The location selected is one of the bottom corners of the part depicted in figure A1. The output time is selected so that the laser beam has just passed over the mentioned location. The time step increment is fixed in 3 ms for all the cases.

The temperature convergence is depicted in figure A2. The selected mesh size is 0.8 elements per layer once the result gets stabilized and presents only a 0.1 % difference with the finest mesh result.

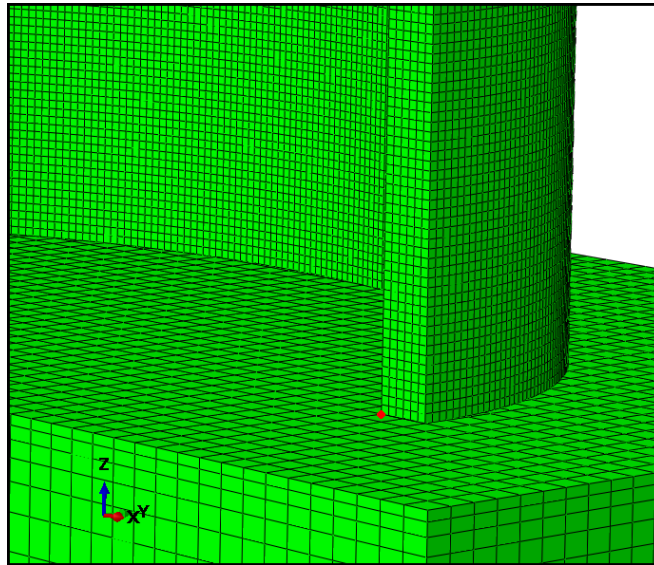


Figure A1: Node evaluated (red point) for the high fidelity mesh convergence study.

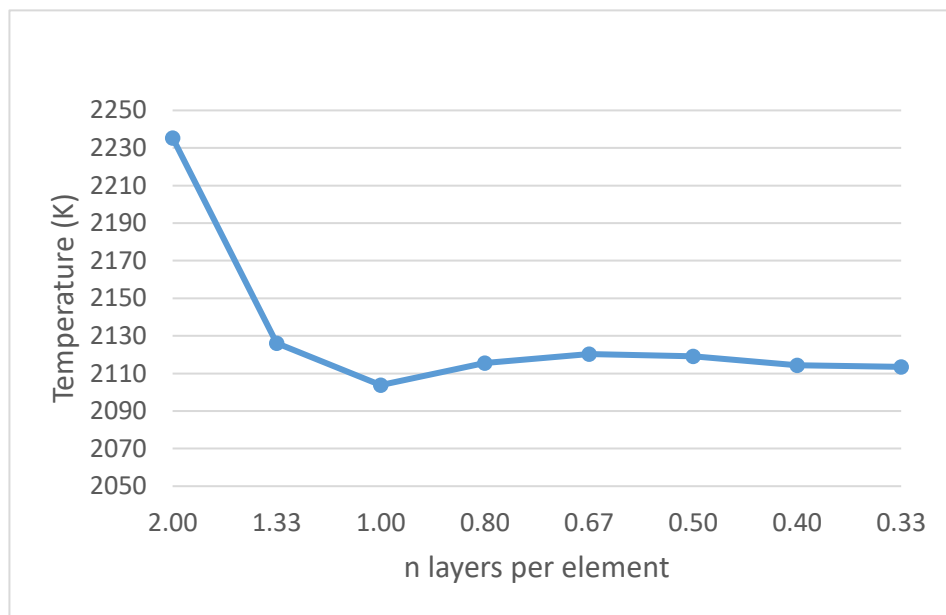


Figure A2: Mesh convergence study for the HF model.

MF SCALED MODEL

The convergence in the MF model evaluates the full temperature history during the printing process. The inner bottom corner of the part is evaluated for a range of mesh sizes between 2 and 5 *physical layers*. Figure A3 shows the location of the node. The time step increment is fixed to 2 *increments per physical layer*.

Figure A4 shows the thermal evolution of the different mesh sizes. It can be noticed the high cooling rate after the printing time of 107 s. All the cases resulted in two different temperature evolutions. The big difference between 3 and 3.5 sizes is caused by the addition of one element along the thickness of the part. The selected size is 3 *elements* (depicted in yellow) as it is the coarsest size which accurately follows the temperature profile of the most refine mesh size (green).

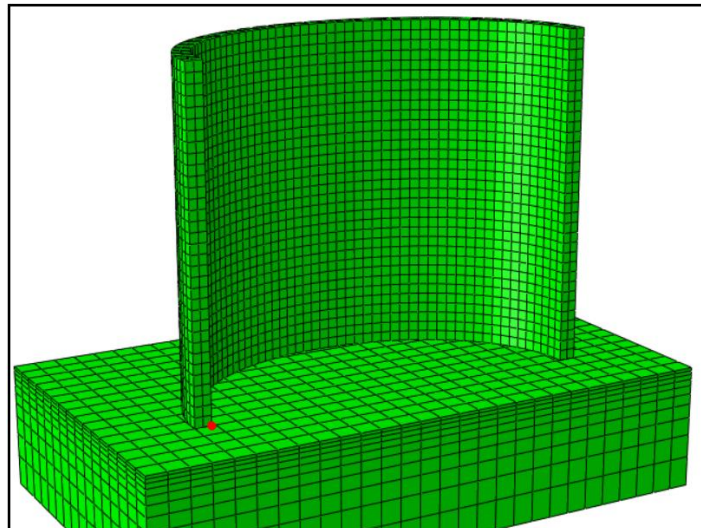


Figure A3: Node evaluated (red point) for the scaled MF mesh convergence study.

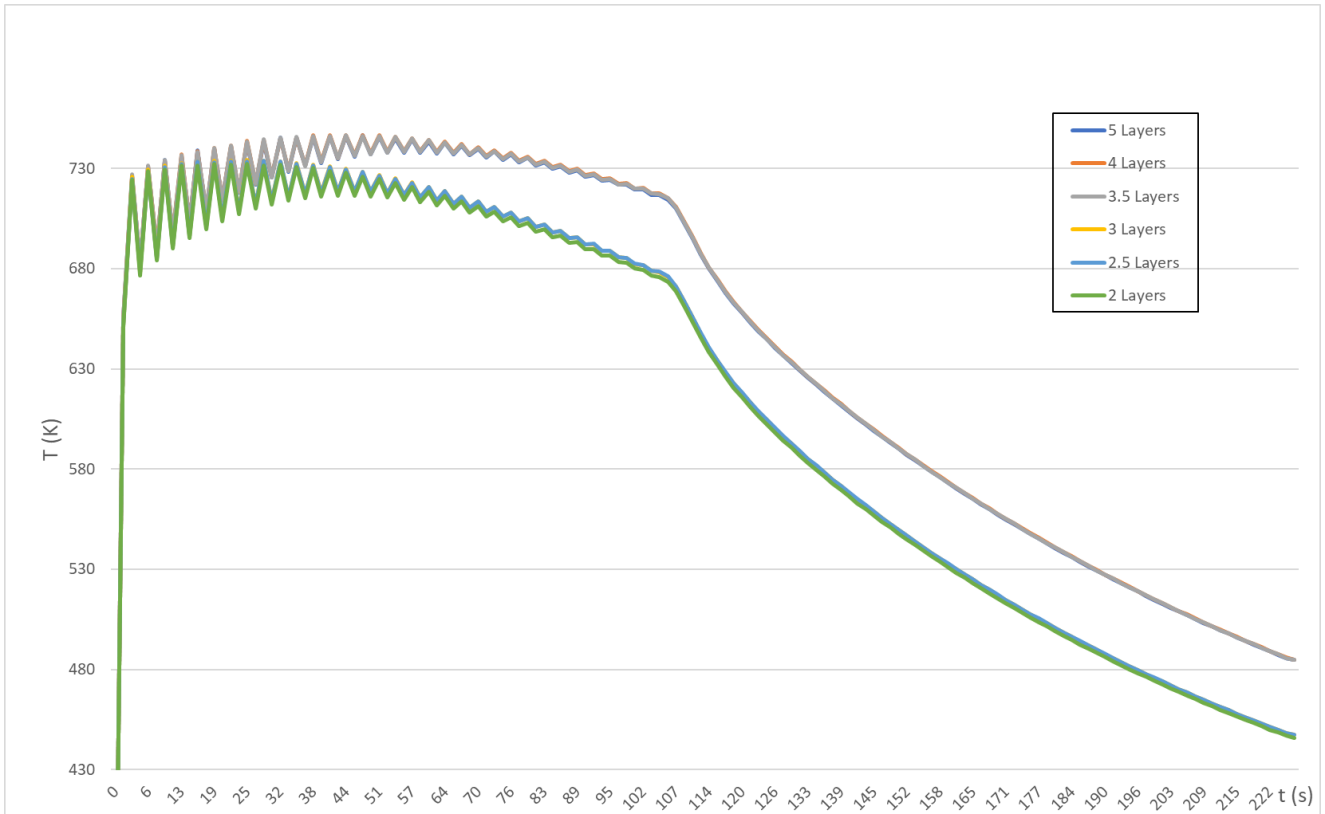


Figure A4: Mesh thermal history convergence of a single node for the MF scaled model.

LF MODEL

The mesh convergence in the LF model evaluates the distortion in the X -direction U_x . The mesh size is related to the physical layer thickness. A range of sizes from 1 to 20 layers per element is analysed. The location selected is the top right outside corner of the part (red point in figure A5). The results are extracted at the end of the printing period. The time step increment is fixed in 30 s for all the cases.

The displacement result for all the cases is shown in the graph of the figure A6. It is observed the solution's convergence from an element size of 7 physical layers. The nodal displacement for the aforementioned mesh size presents only a 0.12 % difference with the displacement of the most refine case. Then, an element volume of 0.42 mm^3 is applied to the whole part resulting in a number of nodes of 58210.

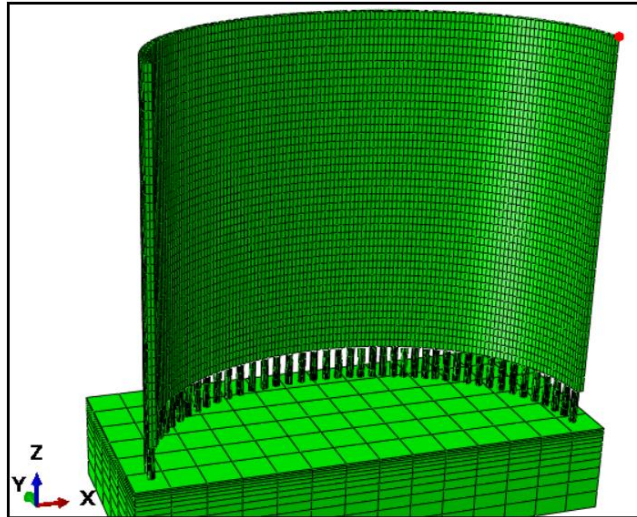


Figure A5: Node evaluated (red point) for the LF mesh convergence study.

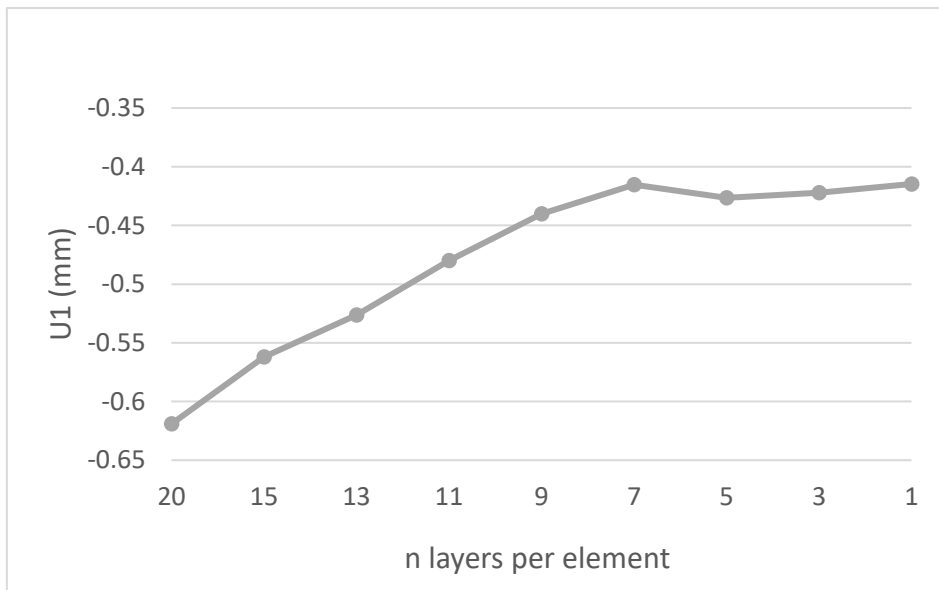


Figure A6: Mesh convergence study for the LF model.

MF REAL MODEL

The mesh convergence of the real model evaluates the temperature history of the bottom corner node depicted in figure A7. The mesh size is related to the number of elements along the part thickness. The effect on the temperature evolution for a range from 1 to 7 elements is shown in figure A8. The time increment is fixed for all the cases.

The mesh size of 6 *elements* is selected. The temperature varies less than a 3 % compared to the most refine size at a time of 2282 s when the maximum difference takes place. The selected size of 6 *elements per part thickness* corresponds to 2.33 *physical layers per element height*. A total number of 1000482 nodes form the mesh of the part.

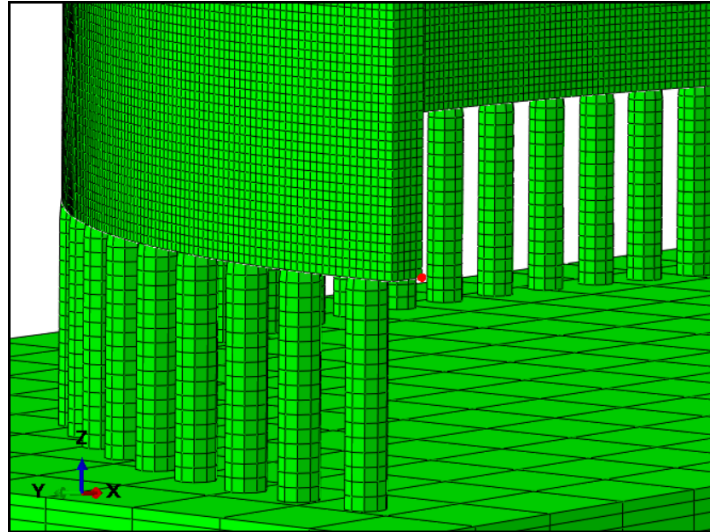


Figure A7: Node evaluated (red point) for the real MF mesh convergence study.

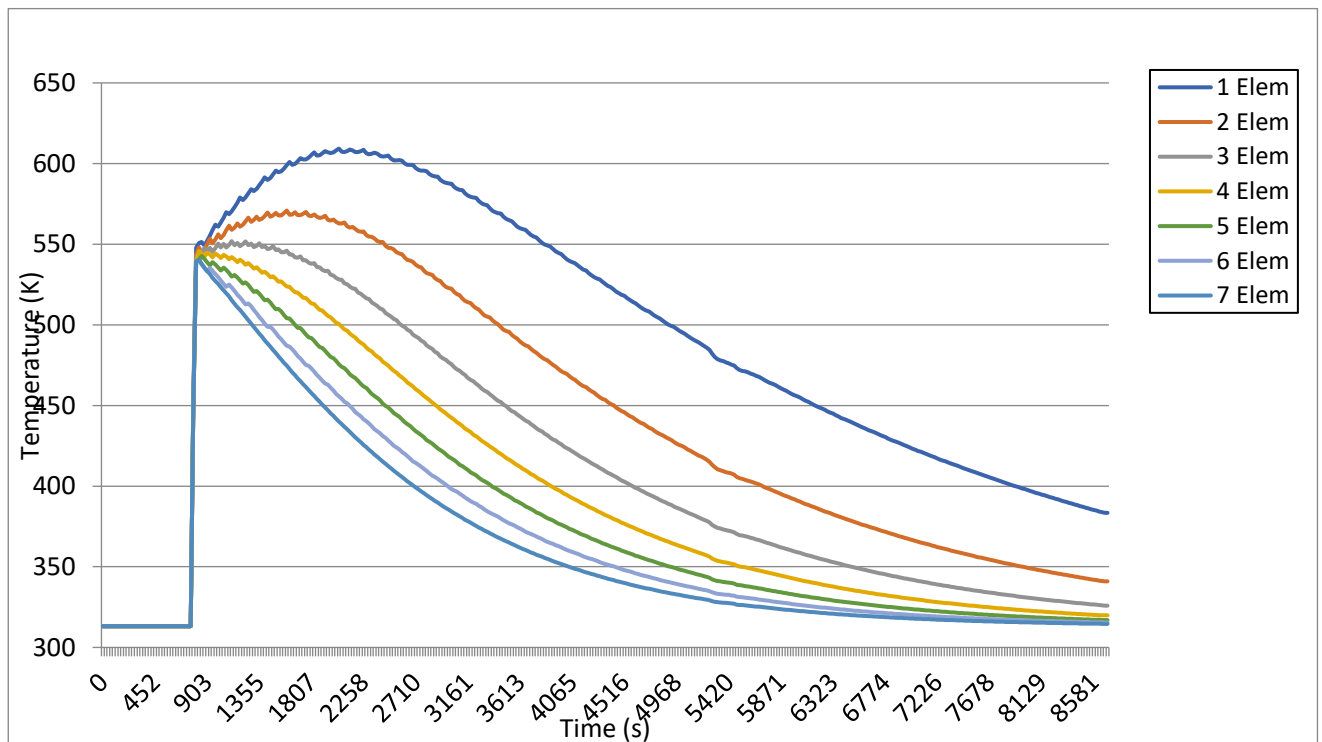


Figure A8: Mesh thermal history convergence of a single node for the MF real model.

A.2.2. Time increment convergence.

HF MODEL

The time stepping convergence in the HF model is done for a range of time increments from 3 ms to 0.5 ms . The melting pool length and the temperature belonging to one node inside the melting pool are evaluated. The melting pool shape (area over 1873 K) can be visualized at the figure A9. The node is located in the fifth layer belonging to the infill track. The temperature is extracted at a printing time of 5.279 s .

The convergence graph for the melting pool length and the nodal temperature are shown at the figures A10 and A11, respectively. The molten pool length convergences for a time increment of 1 ms . However, the nodal temperature requires a shorter increment of 0.75 ms .

A temperature time-history evaluation is done in order to confirm the time increment selection of 0.75 ms . A node from the contour of the fourth layer is evaluated for the range of time increments. The results are depicted in figure A12. The largest difference between the profiles takes place at the moment that the laser is on the top of the point evaluated. For some cases the time increment perfectly matches the node location ($\Delta t = 1\text{ ms}$) and for others the evaluation takes place a bit displaced from the nodal exact location (rest of the cases). Thus, it is reasonable to focus on the remaining temperature profile to evaluate the convergence. The proposed time increment of 0.75 ms (light blue) closely approximates the finest increment of 0.5 ms (green) during the infill track period as well as for the cooling periods between layers. Consequently, the thermal solution is solved with a time step increment of 0.75 ms .

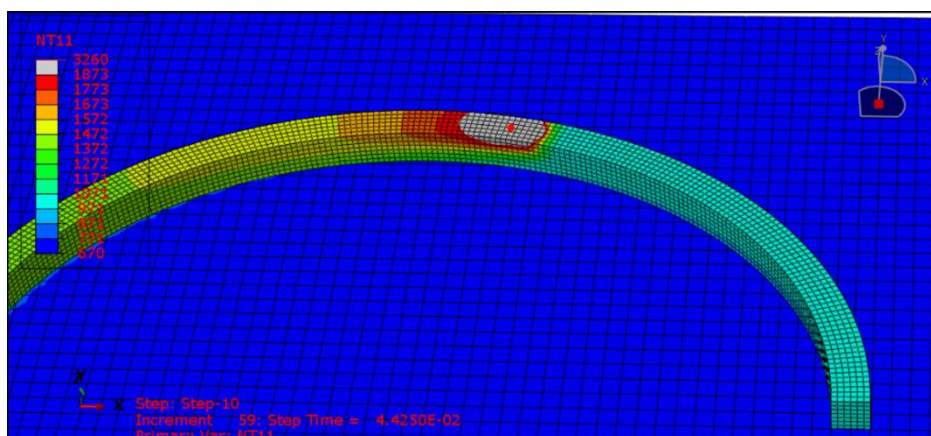


Figure A9: Molten pool evaluated for the High-fidelity convergence study.

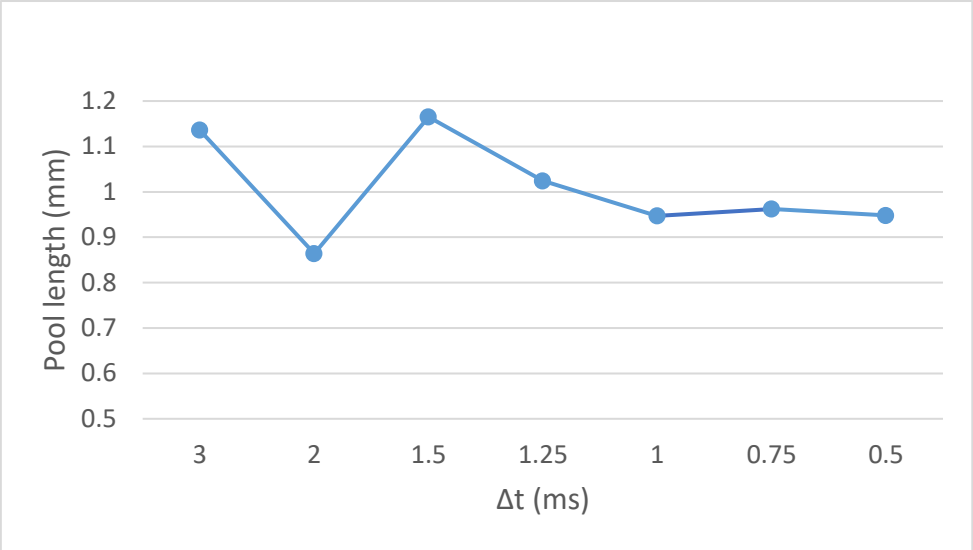


Figure A10: Pool length stepping convergence for the High-fidelity model.

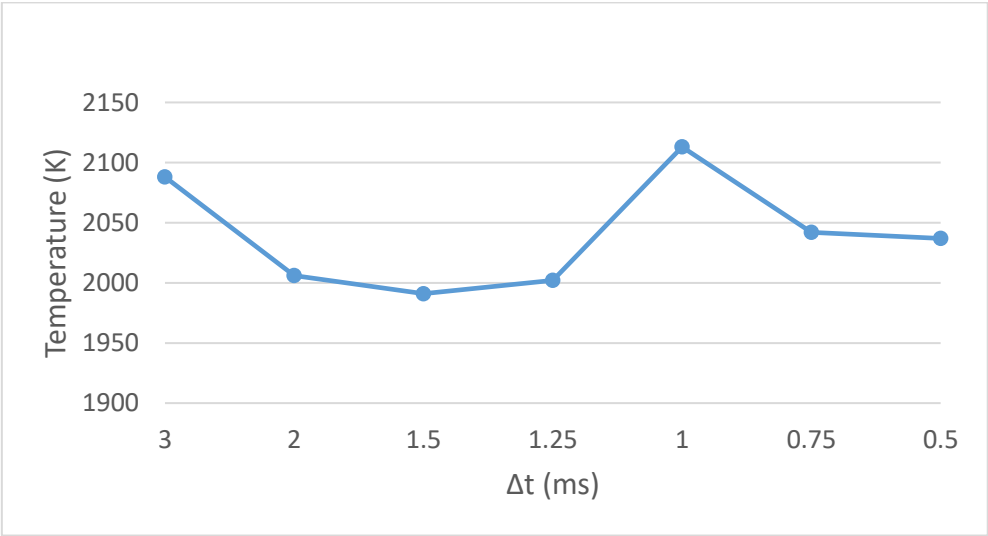


Figure A11: Nodal temperature stepping convergence for the High-fidelity model.

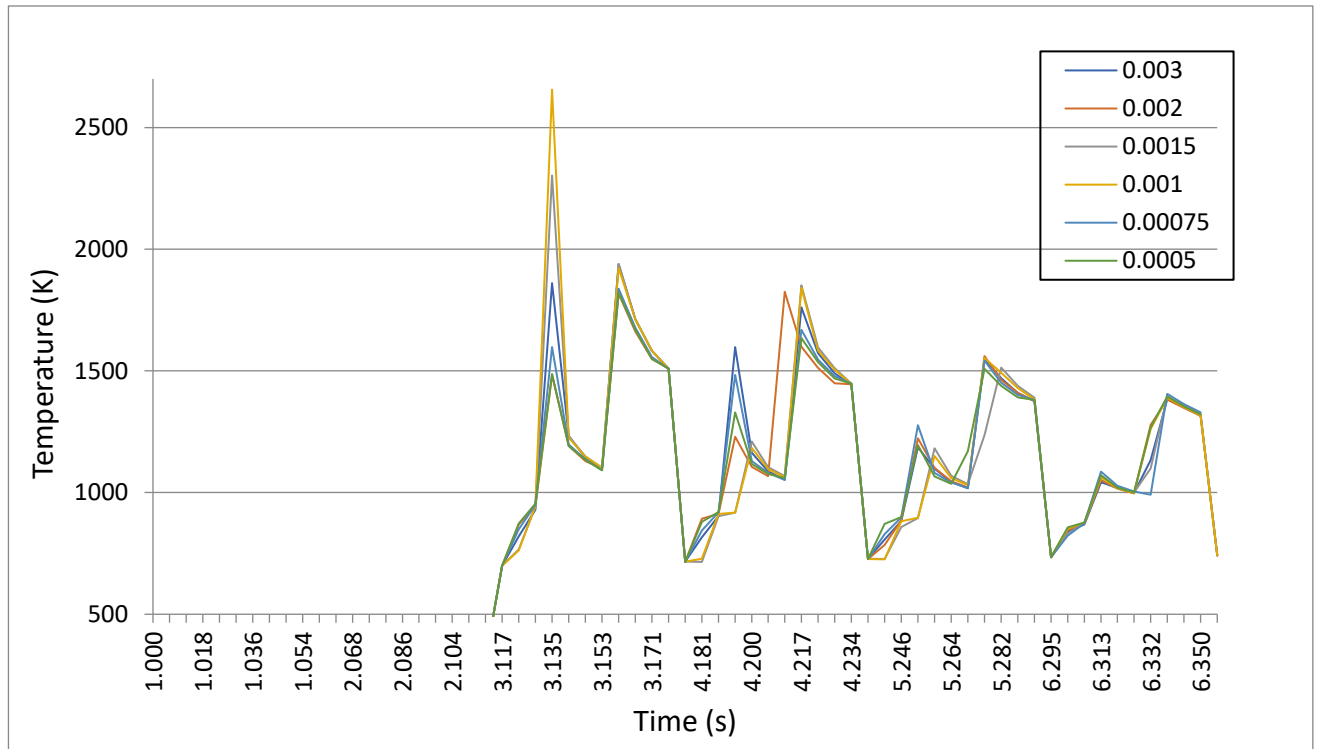


Figure A12: Δt thermal history convergence of a single node for the High-fidelity model.

The mechanical time increment of the HF model is selected by evaluating the printing of the first ten layers of the part. A time increment range from 15 to 0.625 ms is studied. The location of the node where the Von Mises stress is evaluated can be observed in figure A13. Figure A14 shows the convergence as the time increment decreases. The stress field converges from a time increment of 2.5 ms. On the other hand, the distortions are evaluated at the node location depicted in figure A15. The time dependence of the displacement is illustrated at the figure A16. The convergence is observed after decreasing the time increment to 1 ms. Thus, the selected time increment is 1 ms for solving the whole mechanical model. Even though, there is not a big difference in magnitude compared to the 2.5 ms increment, the error would get accumulated and become considerable when building up the remaining 90 layers.

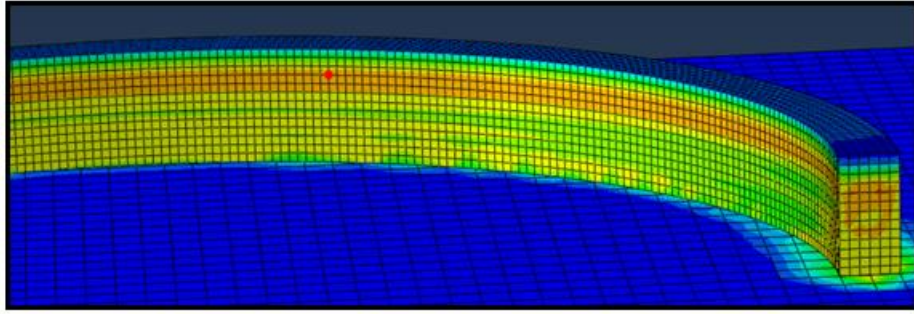


Figure A13: Nodal location (red point) of the HF time increment convergence study. Stress evaluation.

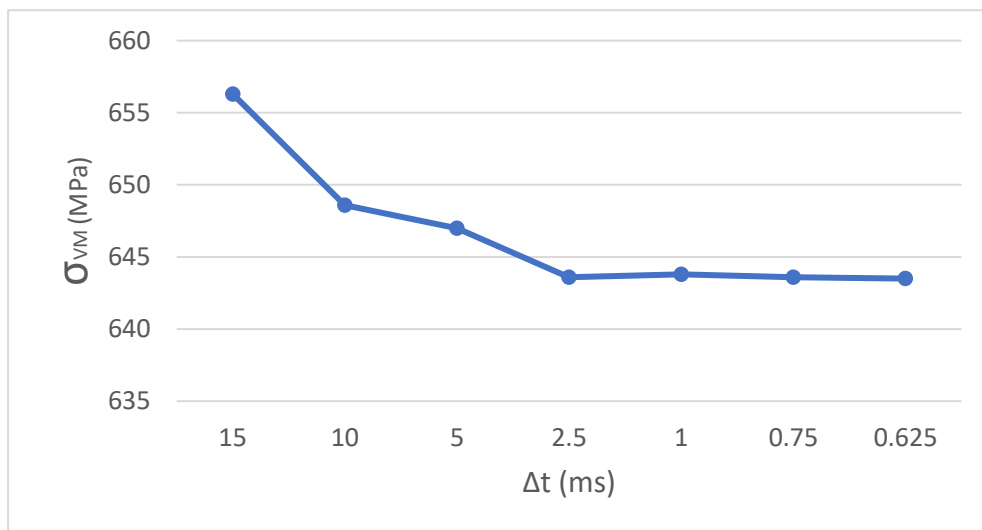


Figure A14: Stress-time convergence for the HF model

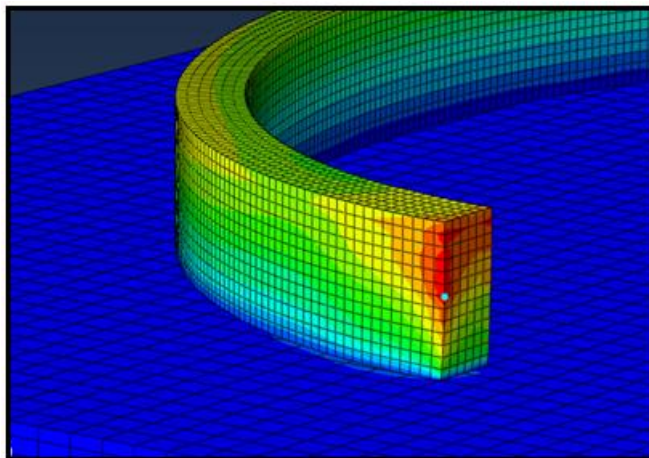


Figure A15: Nodal location (blue point) of the HF time increment convergence study. Distortions evaluation.

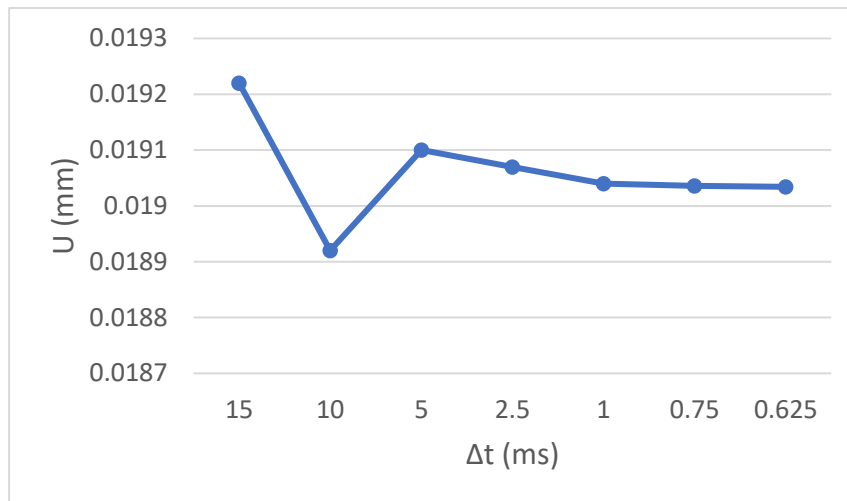


Figure A16: Distortions-time convergence for the HF model

MF SCALED MODEL

The time is evaluated in a range between *1* and *15 increments per element layer*. The mesh size is fixed in *3 physical layers per element* in all the cases. The temperature history of the node 4759 of the part is evaluated. The nodal location is depicted in figure A17. The centred position avoids any influence from the build plate.

Figure A18 illustrates the temperature evolution during the whole process of all the cases. The largest difference is found at the time that the laser passes over the node. During the cooling period the temperature profiles unify. As the objective of this type of simulation is to approximate the far-field temperature evolution, the temperature ten layers on top of the node ($t = 60$ s) gets evaluated and depicted in figure A19. The convergence is achieved and *9 increments per layer* is selected as the final choice (*1 %* difference with the finest case of *15 increments*). *9 increments per layer* corresponds to a time magnitude of *0.35 s*.

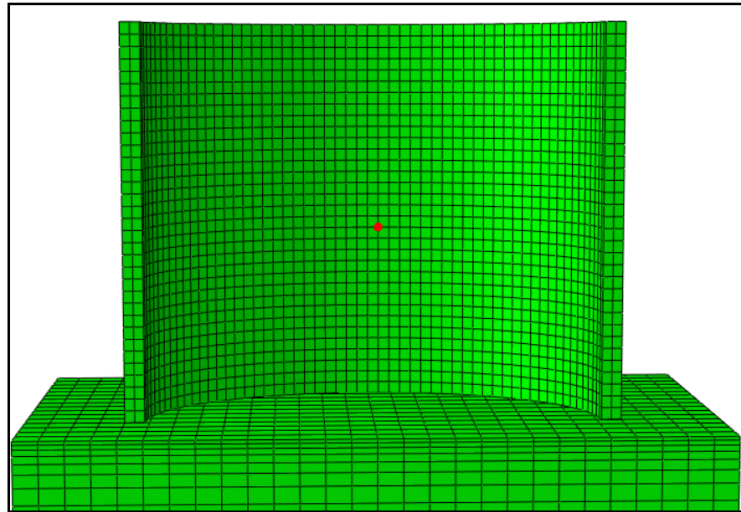


Figure A17: Node evaluated (red point) for the scaled MF thermal time stepping convergence study.

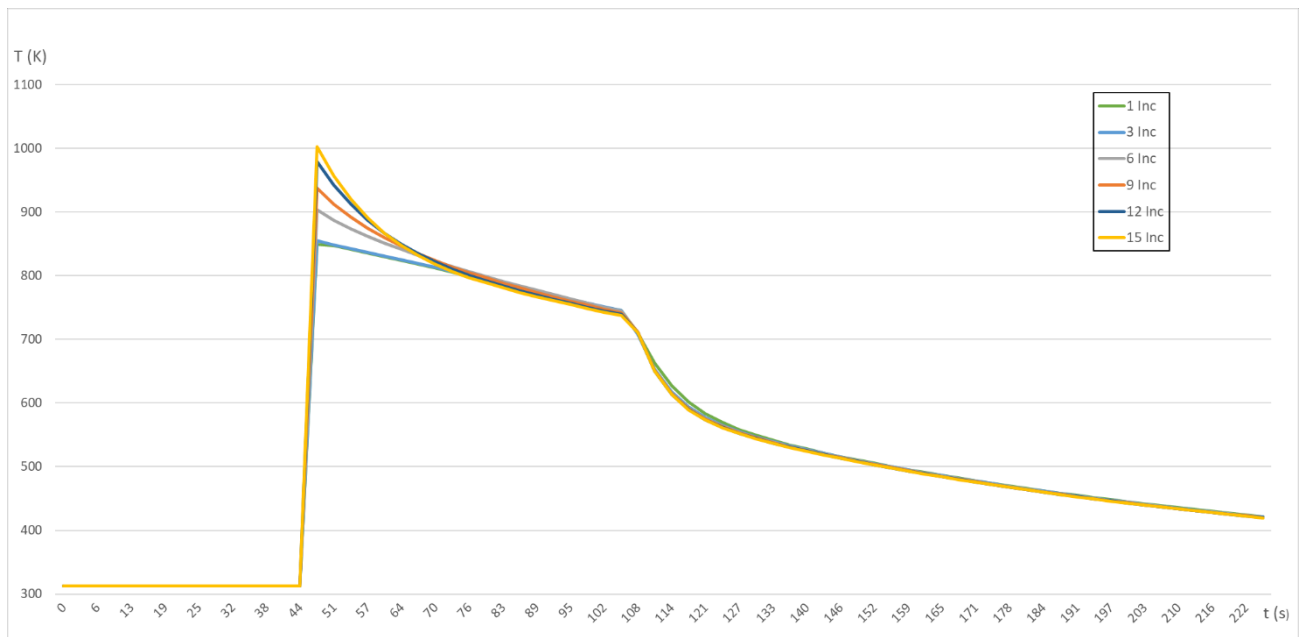


Figure A18: Thermal history convergence of a single node for the scaled MF model.

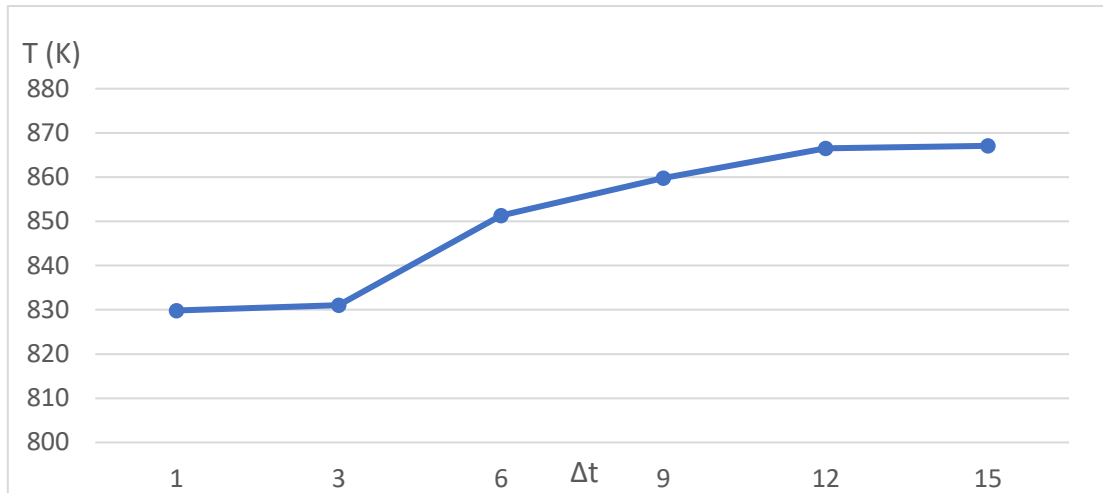


Figure A19: Temperature-time convergence for the scaled MF model at a $T=60$ s.

The proper time-dependent temperature field previously calculated by the thermal convergence study is introduced to the mechanical model to calculate the distortions as well as the stresses. The results are extracted after two minutes of cooling for a range between *1* and *15 increments per element layer*.

First the displacement in the Y-direction U_Y (mm) is evaluated at the node 5387 whose location is shown in figure A20. Figure A21 shows the solution convergence from *12 increments*. On the other hand, the Von Mises stress σ_{VM} (MPa) is extracted at the location depicted in figure A22. The trend in figure A23 confirms that *12 increments per element layer* achieves the solution convergence (less than 1 % difference with the stress for *18 increments*). The relative size of *12 increments per element layer* in this model means a time increment of *0.146 s*.

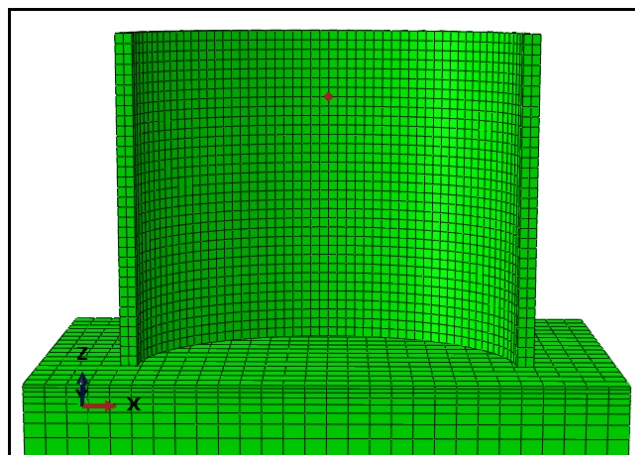


Figure A20: Node evaluated (red point) for the U_Y - time convergence study of the scaled MF model.

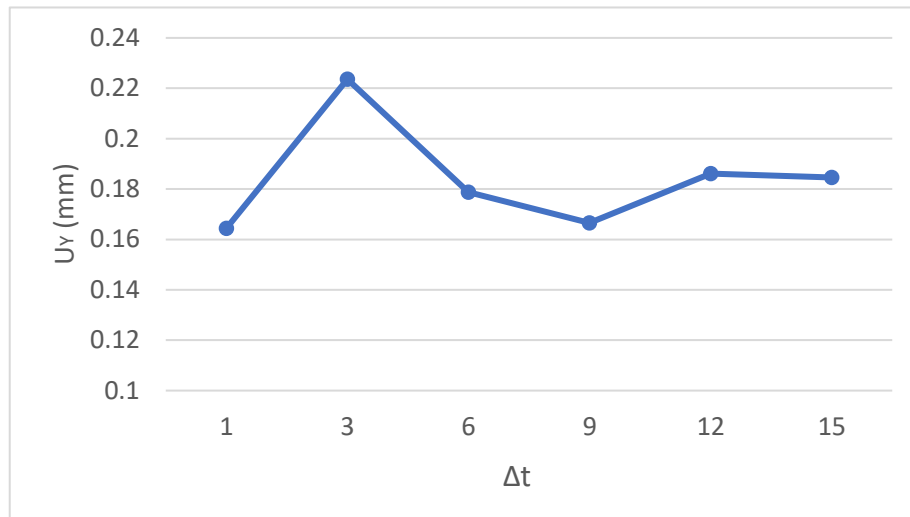


Figure A21: U_y - time stepping convergence for the scaled MF model.

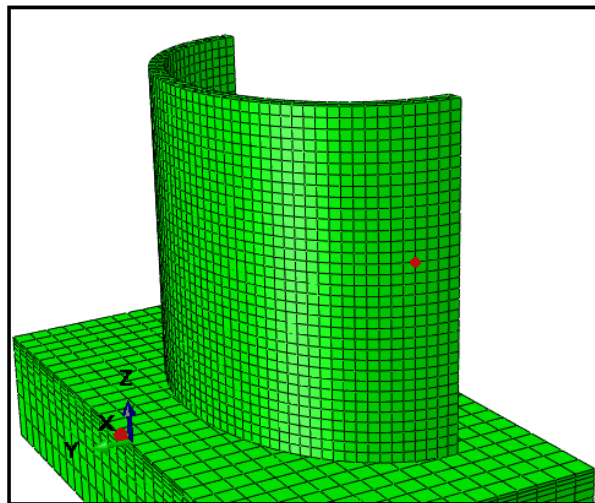


Figure A22: Node evaluated (red point) for the σ_{VM} - time convergence study of the scaled MF model.

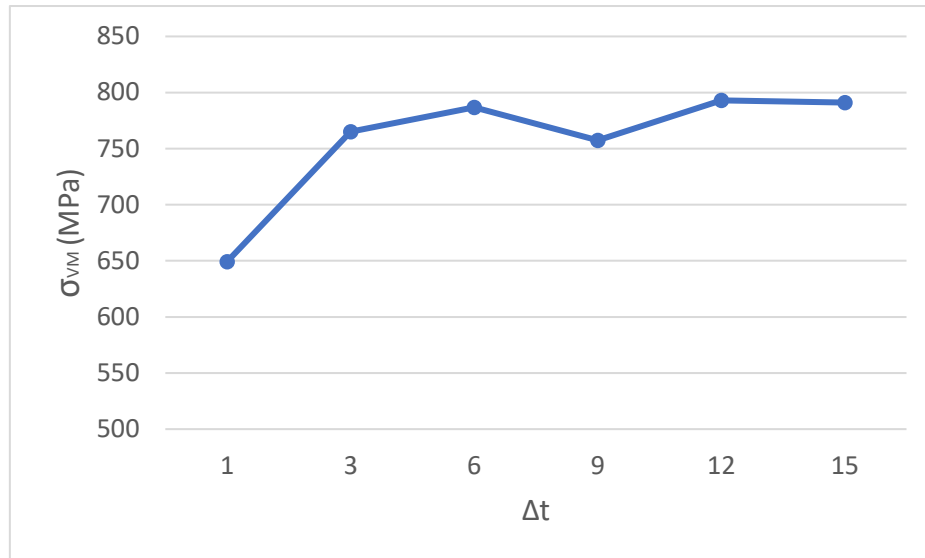


Figure A23: σ_{VM} - time convergence for the scaled MF model.

MF REAL MODEL

The resulting mesh size of *2.33 layers per element* is fixed in the time convergence study. A range from *1 to 15 time increments per element layer* is evaluated on the node *909603* highlighted in figure A24. The output variable is the temperature history during the printing process plus five minutes of cooling. The output frequency is limited to every other physical layer to reduce the data size. Figure A25 shows the temperature profiles for the different time increments. The decreasing trend of the temperatures comes from extracting the results right after the *11 s* layer deposition period when the part cools down.

The MF model captures accurately the far temperature field. Then, the temperature at a time corresponding to the printing of the tenth layer after the evaluated node is depicted in figure A26. The temperature for a time increment size of *6 increments per element layer* presents a 2 % difference with the most refine size and, thus, it is selected as the thermal time discretization.

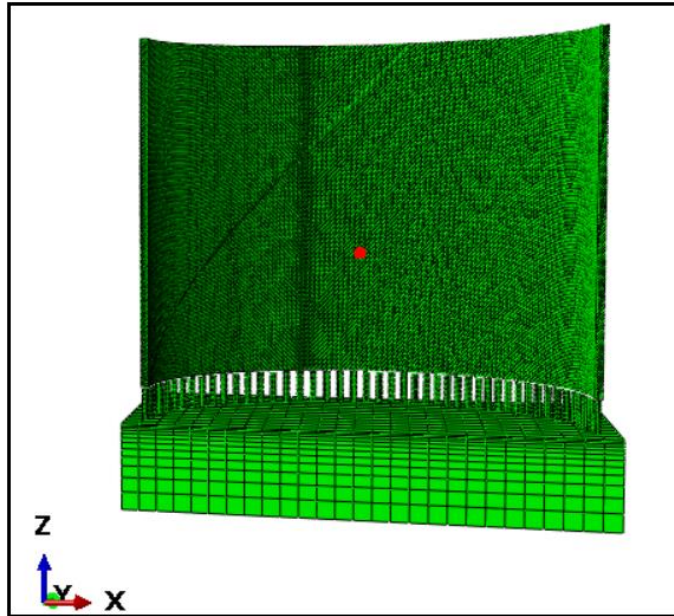


Figure A24: Node evaluated (red point) for the thermal-time convergence study of the real MF.

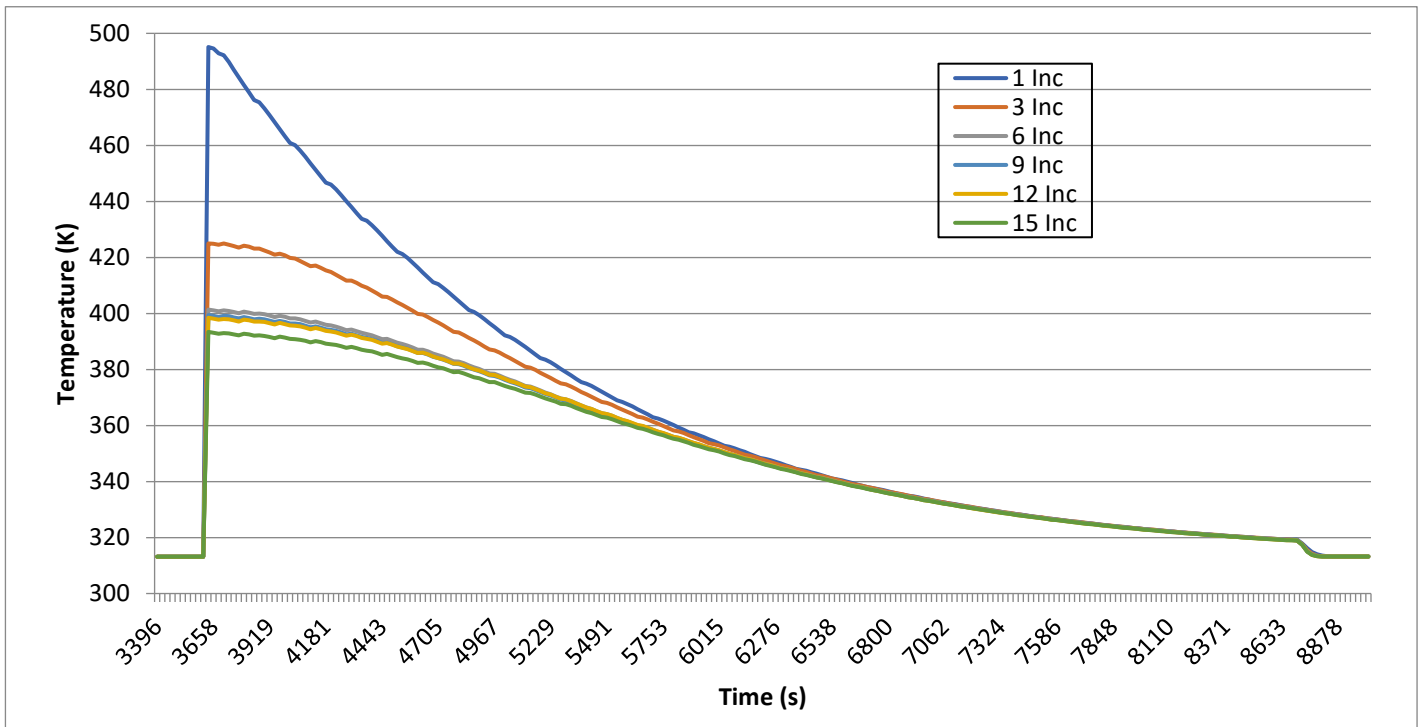


Figure A25: Δt thermal history convergence of a single node for the real MF model.

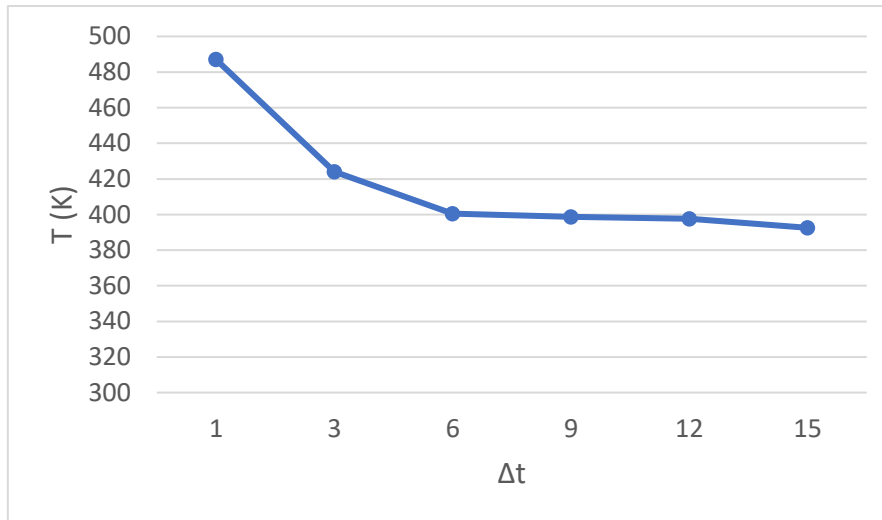


Figure A26: Nodal temperature stepping convergence for the real MF model at a $T=3759$ s.

A reduced model of one quarter of the original height is used for the mechanical time convergence study due to the high computational resources required. The range of increment sizes covers *from 1 to 15 increments per element layer*. The output variables are the displacements in *X-direction U_1 (mm)* and the Von Mises stress σ_{VM} (MPa). Figure A27 depicts the location of the evaluated node 7964 and the results are presented in figure A28. The time discretization of *6 increments per layer* is selected. Despite of a decrease with the time increment refinement, the displacement for *6 increments per layer* represents less than 1 % difference compared to *15 increments*. The Von Mises stress result depicted in figure A29 confirms the selected time increment as the most efficient choice.

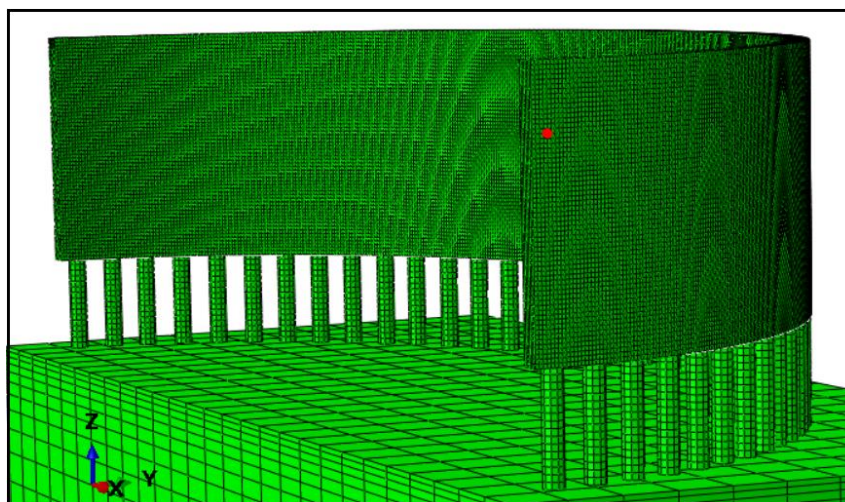


Figure A27: Node evaluated (red point) for the real MF- U_1 time stepping convergence study.

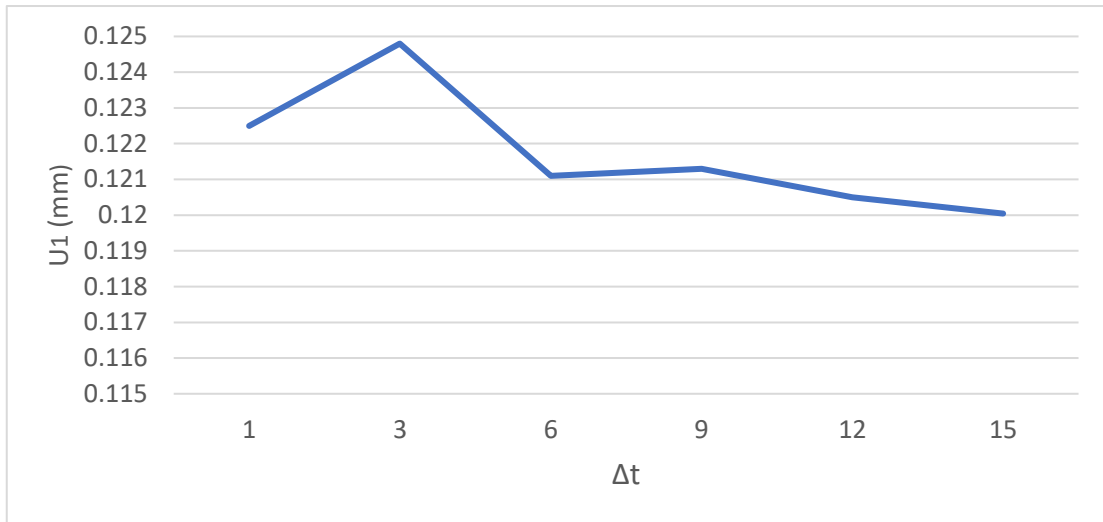


Figure A28: U_1 - time stepping convergence for the real MF model.

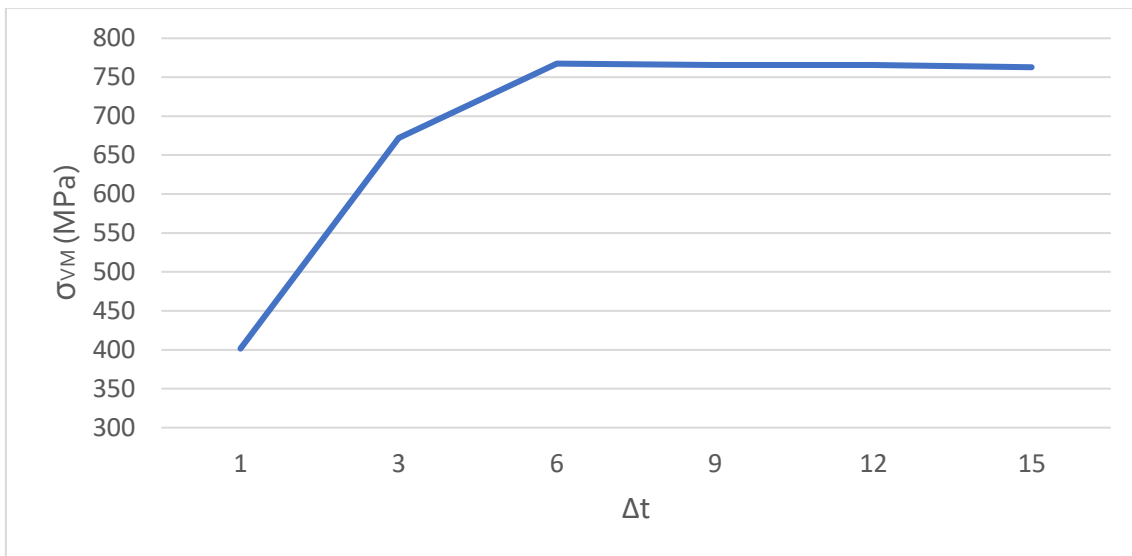


Figure A29: σ_{VM} - time stepping convergence for the real MF model.

A.3. Experimental measurements.

The dimensions of the top and bottom faces of the scanned parts are measured in Paraview® using the ruler tool in the following way:

- Width: distance from the outer corner of the left side to the outer corner of the right side. They are named “Top width” and “Bottom Width” in figure A30.
- Depth: two measurements are taken of the depth named “Bottom Depth” and Top depth” in figure A30. *Bottom Depth* represents the distance from the inner corner of the left side to the middle point located on the inner contour of the bottom face. *Top Depth* represents the distance from the outer corner of the left side to the middle point located on the inner contour of the top face. The actual dimensions are the projections in *YZ-plane* of the aforementioned measurements depicted in figure A31. A calibration example of the central point in the Part3 is shown in figure A32 where “X Range” is used to locate the centre and “Y Range” represents the Depth magnitude.
- Height: a single measurement is analysed from the bottom to the top of the left outer corner. Figure A30 illustrates the “Height” distance.

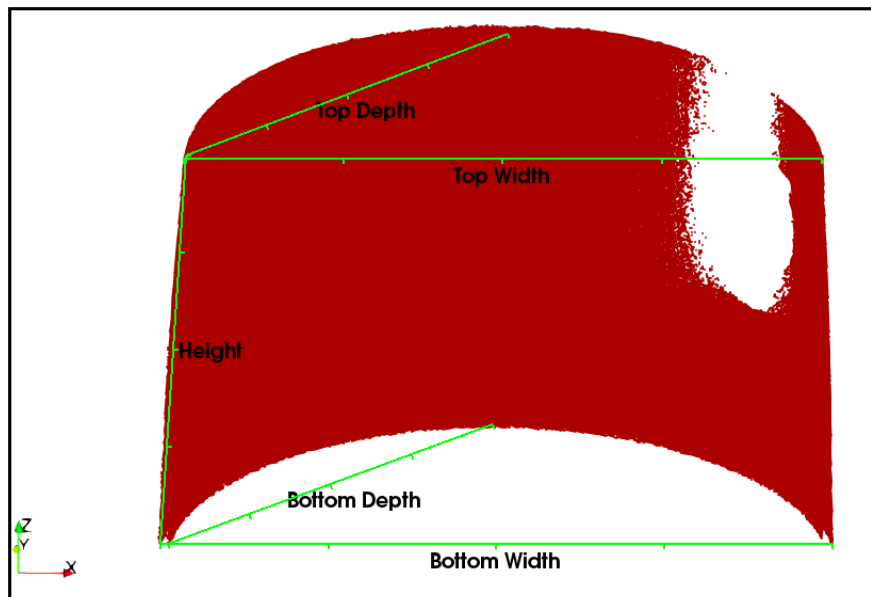


Figure A30: Measurements in the experimental parts.

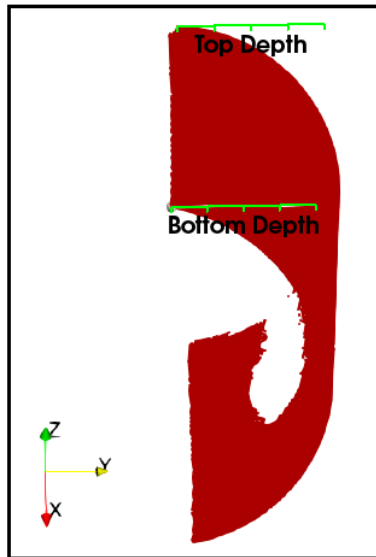


Figure A31: Depth measurements of the parts.

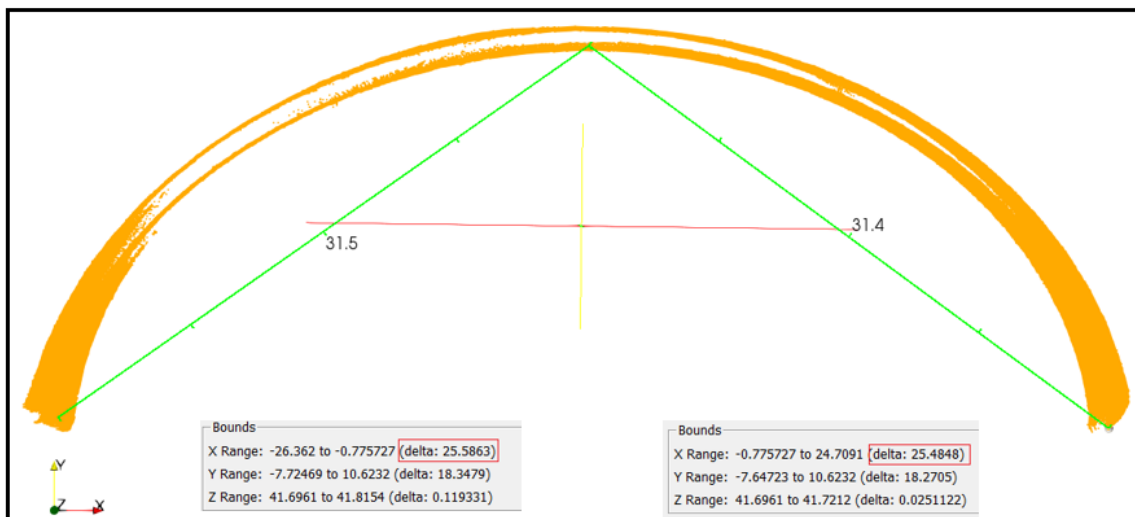


Figure A32: Depth measurement's calibration.

